UNIVERSITY OF CALIFORNIA

Santa Barbara

Reliability of InAs quantum dot lasers grown on silicon: Physics, Limits and Solutions

A dissertation submitted in partial satisfaction of the

requirements for the degree Doctor of Philosophy

in Materials

by

Jennifer Grace Selvidge

Committee in charge:

Professor John Bowers, Co-Chair

Professor Kunal Mukherjee, Co-Chair

Professor Daniel Gianola, Member

Professor Arthur Gossard, Member

Dr. Robert Herrick, Member

June 2021

The dissertation of Jennifer Grace Selvidge is approved.

Daniel Gianola

Arthur Gossard

Robert Herrick

John Bowers, Committee Co-Chair

Kunal Mukherjee, Committee Co-Chair

June 2021

Reliability of InAs quantum dot lasers grown on silicon: Physics, Limits and Solutions

Copyright © 2021

by

Jennifer Grace Selvidge

ACKNOWLEDGEMENTS

In the past, scientific research took the form of a marathon, which is to say, a single individual would run a long distance, without assistance from others. Likewise, many older papers have one or two authors. However, the research in my PhD journey, and in modern engineering departments more generally, closely resembles a relay race. As the failure analysis and reliability expert, I would never have been successful without the rest of the runners on the team. However, as our team was substantially bigger than the four people included on an athletic team, fully acknowledging each of them will unfortunately not be possible. Nevertheless, my aim in this section is to give my key contributors their due.

Firstly, I must acknowledge my committee and internship supervisor, the coaches for my relay team. Prof. John Bowers and Prof. Kunal Mukherjee as my advisors have both been instrumental in my development as a scientist. Dr. Bowers provided me with the freedom to pursue my interests, even when they were not his own. I became the resident microscopy expert in the group early on, which helped me to gain confidence in my work, to check my own assumptions and work frequently, and to not be afraid to develop my own experimental methods. Dr. Mukherjee, for his part, had a keen sense of when I was making forward progress and when I was wandering randomly in the vastness of TEM and STEM possibilities. When it was the latter, he helped me map out a path. For the last few years of my degree, we acted as collaborators more than advisor and advisee, which has, in my opinion, led to some particularly interesting work. I had two other UCSB faculty members, Prof. Arthur Gossard and Prof. Daniel Gianola, serve on my committee. Dr. Gossard has served on my committee since the beginning and has also faithfully attended the weekly

Bowers quantum dot sub-group meetings providing his growth expertise as resource for myself and the other students and post-docs. In addition to his service on my committee, Dr. Gianola has served as the UCSB Microscopy and Microanalysis Facility (MMF) Director. His work to ensure the Facility ran smoothly during my time ensured I had access to the equipment and other resources I needed, whenever I need them. My external examiner, Dr. Robert Herrick, from Intel has also been particularly instrumental. From early on, Dr. Herrick identified that I had potential as a microscopist and worked to nurture it. As a part of this, he helped me to get an internship with the premier semiconductor electron microscopy industrial consulting firm, EAG Laboratories-Eurofins Materials Science. My boss at EAG, Dr. Michael E. Salmon also provided me with immeasurable help during the 4.5 months I was in Raleigh, while also encouraging me to push the limits of EAG's brand new Attolight Rosa CL system. As noted in the text, I conducted the measurements in Chapter 4 of this thesis under his supervision, during that internship.

Before acknowledging students and post-docs, I would be remiss in not mentioning the MMF staff engineers, who perhaps most closely resemble the medical team for my relay. Dr. Aidan Taylor and Dr. Claire Chisholm have been especially instrumental in this work. In addition to working tirelessly to ensure the incredibly finnicky electron microscopes were working as intended, they have gone above and beyond to aid my progress, assisting with things as varied as Defense preparation and STEM sample loading (when I had drunk too much coffee prior to my session). Other critical UCSB staff members include Ms. Bettina Norton, Ms. Tina Huang, and Ms. Ceanna Bowman who always ensured that I got paid and that my gateway shopping carts filled with omniprobe grids went through.

My fellow student and post-doc runners clearly played critical roles as well. Among the many who passed me 'batons', either literally in gel packs or figuratively in countless meetings and brainstorming sessions, Dr. Justin Norman and Mr. Eamonn Hughes deserve special recognition for their consistent roles. Dr. Norman grew the samples analyzed in all three of my first/co-first author papers, while I performed the microscopy in his later work. Likewise, Mr. Hughes and I went round and round, discussing results, trading samples, and re-writing each other's sections in our co-first authored papers. Indeed, we worked so closely, our writing styles began to converge—I even got him to come around a little on the em-dash! Dr. Daehwan Jung, Mr. Chen Shang, and Mr. Mario Dumont also provided support on the MBE growth side, while Dr. Yating Wan, Mr. Jon Peters, Mr. MJ Kennedy, Dr. Robert Zhang, Mr. Warren Jin, and Ms. Kaiyin Feng provided support on the fabrication side. Other student/post-doc members of both Bowers and Mukherjee groups also frequently provided me with helpful discussions.

My family and friends, including my parents and my lovely wife Delaney, also deserve acknowledgements for keeping me sane, laughing, and crying with me. Although their contributions were not scientific, they were no less important in my graduating.

VITA OF JENNIFER GRACE SELVIDGE
May 2014

EDUCATION

Bachelor of Science in Materials Science and Engineering, Massachusetts Institute of Technology, June 2015
Doctor of Philosophy in Materials, University of California, Santa Barbara, June 2021 (expected)

PROFESSIONAL EMPLOYMENT

2015-2021: Graduate Student Researcher, Materials Department, University of California, Santa Barbara
Summer 2018: Summer Internship, EAG Laboratories-Eurofins Materials Science

SELECTED PUBLICATIONS

Jennifer Selvidge, et al. "Reduced dislocation growth leads to long lifetime InAs quantum dot lasers on silicon at high temperatures," Appl. Phys. Lett. 118, 192101 (2021); https://doi.org/10.1063/5.0052316

Jennifer Selvidge, et al. "Defect filtering for thermal expansion induced dislocations in III–V lasers on silicon," Appl. Phys. Lett. 117, 122101 (2020); https://doi.org/10.1063/5.0023378

Jennifer Selvidge, et al. "Non-radiative recombination at dislocations in InAs quantum dots grown on silicon," Appl. Phys. Lett. 115, 131102 (2019); https://doi.org/10.1063/1.5113517

AWARDS

Best Student Paper, 62nd Electronic Materials Conference, virtual, 2020

Fellow, National Science Foundation Graduate Research Fellowship Program, 2016-2021

UCSB Graduate Division Doctoral Scholars Fellowship, University of California, Santa Barbara, 2015-2019

ABSTRACT

Reliability of InAs quantum dot lasers grown on silicon: Physics, Limits and Solutions

by

Jennifer Grace Selvidge

Direct crystal growth approaches for III-V/silicon integration are of great technological interest for photonic integrated circuit applications. However, historically, these approaches have been hindered due to the generation of large numbers of interfacial dislocations that form to mediate materials property mismatches between GaAs/InP based films and the silicon substrate. The presence of dislocations at this interface, far from critical device regions, is not inherently problematic. But their ends, termed threading dislocations, rise upward through all the subsequent device layers, facilitating non-radiative recombination losses where they cross the light-emitting 'active' region. Further, the energy released in these defect-assisted processes facilitates ongoing dislocation growth during laser operation. As a result, these runaway 'recombination enhanced dislocation climb' and 'recombination enhanced dislocation glide' (REDC and REDG, respectively) processes culminate in device failure. Thus, laser reliability engineers have traditionally focused on efforts to reduce threading dislocation densities and to develop dislocation tolerant infrared emitters. However, even with decades of research seeking to reduce threading dislocation densities and to develop more dislocation tolerant gain materials such as p-modulation doped InAs quantum dots (QD),

device lifetimes at industrially relevant temperatures (near 80°C) remained too short by orders of magnitude.

Seeking to better understand the mechanism by which even relatively low densities of threading dislocations led to failure in InAs QD lasers, my colleagues and I identified that the threading dislocations give rise to in plane misfit dislocations lying at the QD layers. This however was puzzling: these layers are designed to be too thin for misfit dislocations to form due to lattice mismatch during growth. We therefore proposed that these specific misfit dislocations formed instead during post-growth cooldown due to (1) thermal expansion mismatch between the (Al)GaAs layers and the silicon and (2) local mechanical hardening effects in the QD layers. To test this hypothesis, we then used metallurgical principles to intentionally widen the mechanically hardened region and thus displace misfit dislocation formation to less critical regions of the device.

This was very successful. Placing a single, thin, alloy-hardened 'misfit dislocation trapping layer' approximately 100-200 nm to either side of the quantum dot active region reduces the total QD adjacent misfit dislocation length by >10x and trapped misfit dislocations show no evidence of recombination enhanced dislocation climb (REDC) after more than 1000 hours of continuous operation at 60°C. Furthermore, lasers with misfit dislocation trapping layers operating 80°C demonstrate median extrapolated lifetimes significantly greater than 100,000 hours—meeting the requirements for data center operation. Thus, these results simultaneously emphasize both the importance of moving in earnest towards the advanced photonic integration schemes and the importance of continuing fundamental materials studies on III-V semiconducting systems.

TABLE OF CONTENTS

1. Introduction 1

2. Reliability Experimental Techniques 11

2.1. Introduction 11

2.2. High Level Optical Inspection Techniques 12

2.3. Micron and Submicron Techniques 13

2.3.1. SEM-Based Analyses 13

2.3.2. Focused Ion Beam (FIB) and SEM Dual Beam Analysis 18

2.3.3. S/TEM-Based Analyses 18

2.4. Summary 28

3. Mechanical Behaviors of III-V Systems 30

3.1. Introduction 30

3.2. Dislocations in Crystals 30

3.2.1. Fundamentals 30

3.2.2. Dislocation motion 32

3.3. Dislocations in Zinc-Blende Thin Films 39

3.3.1. Thin Film Dislocation Formation and Motion Mechanisms ... 41

3.3.2. Quantum Dot Specific Effects 46

3.4. Summary 50

4. Optoelectronic impacts of dislocations on quantum dots materials 52

4.1. Introduction 52

4.2. Carrier Recombination in Semiconductors 53

4.2.1. Auger Recombination 54
4.2.2. Shockley-Read-Hall Recombination 54
4.3. Shockley-Read-Hall Recombination Behaviors in Quantum Dots .. 57
4.3.1. Initial Expectations 57
4.3.2. Model Structure 59
4.3.3. Growth Details 61
4.3.4. Baseline Optoelectronic Measurements 61
4.3.5. Linking Dark Regions to Dislocations 63
4.3.6. Estimating Dark Line Width 65
4.3.7. Temperature and State Dependent Dark Line Behaviors in QD Materials 67
4.3.8. Source of Dislocation Tolerance in QD Model Structures 70
4.4 Non-radiative Recombination's effects on Dislocations 71
4.4.1. Recombination Enhanced Dislocation Glide (REDG) 71
4.4.2. Recombination Enhanced Dislocation Climb 73
4.5. Summary 76
5. Dislocation Filtering Strategies 78
5.1. Introduction 78
5.2. Threading Dislocation Density Reduction 78
5.2.1. Inherent dislocation reduction in zinc-blende films 78
5.2.2. Thermal Cyclic Annealing 80
5.2.3. Lattice Mismatch Based Dislocation Filtering Techniques 81
5.3. Misfit Dislocation Filtering 83

5.3.1. Investigation of Trapping Layers in Model Structures 84

5.3.2. Trapping Layer Laser Characterization 94

5.4. Summary 111

6. Laser Reliability 113

6.1. Introduction 113

6.2. Traditional Laser Failure Modes 115

6.2.1. Catastrophic Failure 115

6.2.2. Rapid Failure 116

6.2.3. Gradual Failure 117

6.2.4. Accelerating Factors 118

6.3. Failure Modes in Lasers with Misfit Trapping Layers 119

6.3.1. Lifetime Testing Conditions 120

6.3.2. Device Reliability Characterization 120

6.3.3. Evaluating Different Trapping Layer Spacings via STEM ... 127

6.4. Summary 136

7. Conculsions and Future Directions 138

7.1. Introduction 138

7.2. Future experimental Directions 140

7.2.1. Mechanical Properties Studies using Model Structures 140

7.2.2. Strategies for Reducing Un-Trapped Misfit Dislocations 144

7.2.3. Looking Beyond Misfit Dislocations to Improve Reliability 146

7.3. Summary 149

References.. 151

Chapter 1:

Introduction

As of the end of 2019, approximately 4 billion people use the Internet in some form.[1] Our telecommunications technologies seamlessly convert information back and forth between electrical and optical signals ones as the information travels around the globe. Nevertheless, as the demand for data continues to grow steadily, technology has struggled to keep up.[2] To address this, researchers have focused on converting electrical pathways to optical ones that promise not only substantial increases in data rates but also substantial reductions in energy costs. This is because, while it requires less energy to generate electrical signals, they suffer higher transmission losses. Thus, at some critical distance, it becomes more efficient to transmit data optically. Optical pulses of different wavelengths do not interact with one another, meaning tens or hundreds of different data streams can be sent simultaneously down a single path.[3]–[6] In contrast, an electrical signal sent down one path can affect a second electrical signal on a separate path through induction, if those paths are sufficiently close together; this also leads to substantial energy losses. Likewise, resistive heating, another process that leads to signal attenuation and energy waste in electrical systems, does not occur in optical waveguides the way it does in electrical wires. Loss in optical systems instead occurs through scattering processes, especially Rayleigh scattering, and through changes to the relative orientation of the light and the waveguiding materials, such as those occurring due to

bending.[7]–[9] Today, data is transmitted optically using infrared light over long and short distances alike, but work remains to be done.

When thinking about the path information takes, as it travels from person to person, there are several different trip lengths of interest ranging from hundreds of km down to meme microns, each with unique considerations. But, at their most fundamental, optical transmission systems require light sources to generate the signal, waveguides to carry it, and detectors to receive it. Lasers, that generate coherent light, are preferable over LEDs as data transmission light sources for transmission rates above 1 Gbps. While a variety of laser designs exist (gas, dye, solid-state/solid-state-fiber), semiconductor lasers are of particular interest because they can be directly electrically pumped and are significantly smaller than the other types. Furthermore, alloying various compound semiconductors with one another provides a broad range of available emission wavelengths, as shown in **Figure 1.1**. Silica waveguides are used in both modern long haul systems connecting data centers and chip to chip links within them, and so they use GaAs- and InP-based diode lasers as light sources. These systems have several key differences arising due to their dissimilar operating wavelengths, 1550 nm and 1310 for long haul systems and chip to chip linking, respectively, but the underlying technology platforms are fundamentally similar.

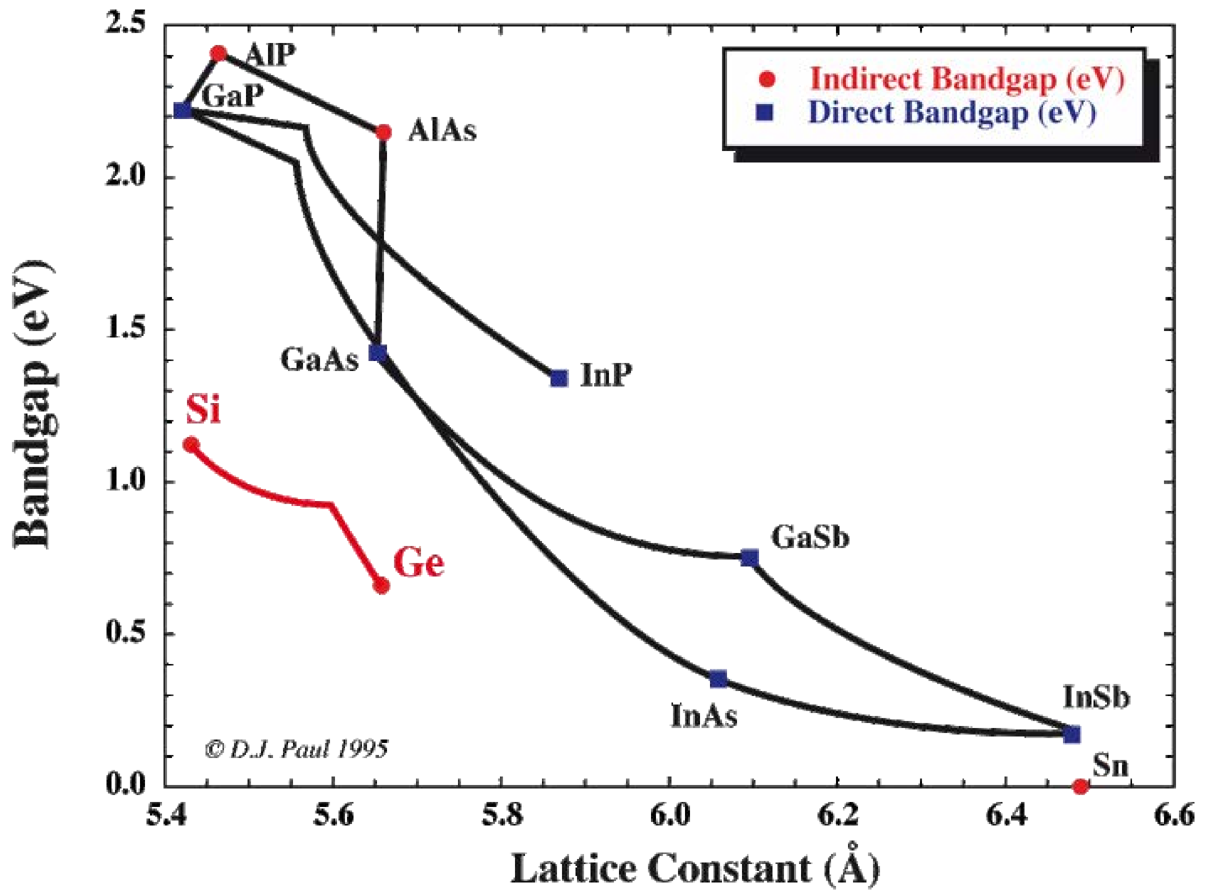

Figure 1.1 Bandgap energy versus lattice constant for common III-V zinc-blende semiconductors and Group IV semiconductors. Note both that the connecting lines between the III-V compounds are represented in black (rather than blue or red) and thus do not indicate whether the intermediary compositions will have direct or indirect bandgaps. After ref.[10]

In contrast, designing optical information pathways on individual chips necessitates more substantial changes to the optical technology platform. In addition to the III-V based systems already discussed, modern information systems also rely very heavily on traditional silicon based integrated circuit components, whose ever shrinking foot-prints remain an area of active development.[11] Additionally, decades of work have resulted in virtually dislocation free 300 mm diameter silicon substrates with costs as low as $0.47/cm^2.[12]

Silicon's high thermal conductivity also makes it an ideal platform choice for active components. Thus, researchers have sought to pathways to build optical systems on existing silicon-based integrated circuit platforms, leading to the rapid growth of silicon photonics which provides high-bandwidth interconnects at a low-cost. Combinations of silicon, germanium, silica, and silicon nitride provide excellent waveguiding materials with refractive indices suitable for wavelengths spanning the infrared to the ultraviolet and, due to the high quality interfaces between them and improved processing, losses as low as 0.1dB/m.[13]–[17] Likewise, both silicon and germanium have been historically used in photodetectors for a wide variety of applications. However, neither is particularly well suited as a light source: their indirect bandgaps lead to slow radiative recombination rates.[18] To date, neither high performance silicon-based lasers nor high performance germanium-based lasers have been demonstrated. Instead, the focus has been on integrating the existing highly-efficient, direct-bandgap III-V light sources with on-chip silicon photonics.

But integrating these two technology platforms has proven difficult; materials properties mismatches between silicon and the III-Vs lead to the generation of large numbers of crystal defects. As a result, two fundamental integration frameworks have emerged: (1) growing III-V light sources on native substrates to prevent defect formation and then integrating them with the silicon based components and (2) growing the III-V light sources directly on CMOS compatible substrates and attempting to mitigating the defects. Hybrid-integration approaches, using co-packaged III-V devices and silicon based devices, and heterogenous-integration approaches such as wafer-bonding, where light is evanescently coupled between bonded silicon and III-V regions are examples of the former framework.

While there are clear and important differences between approaches within the first framework (i.e., heterogenous integration strategies can be used for on chip data transmission and should substantially improve the energy efficiency over co-packaged designs) they are universally limited by use of expensive, small III-V native substrates. Nevertheless, most silicon PICs still rely on the co-packaging based approaches, despite substantial energy costs associated with re-timing the electrical signal.[17] **Figure 1.2** presents the projected evolution of these co-packaged approaches. Gen I-III have been commercially deployed as of 2020, while IV and V are projected.[17]

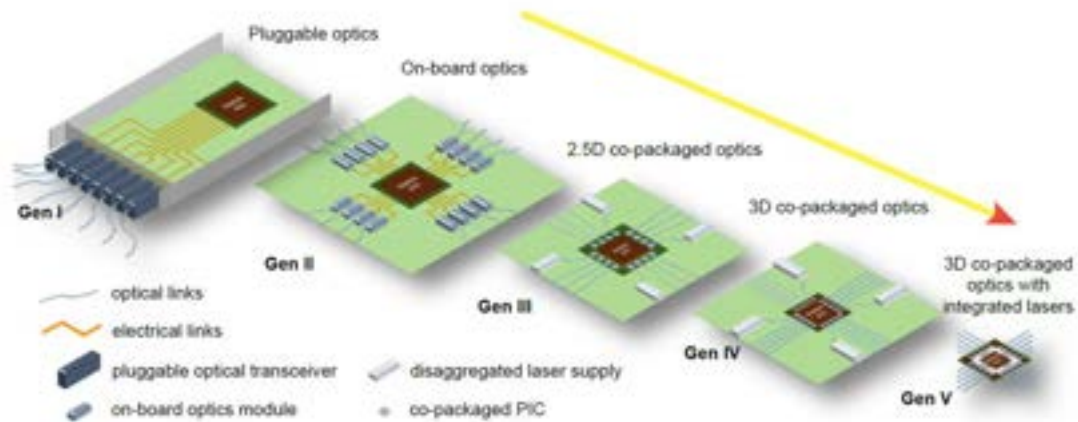

Figure 1.2 Generations of optics and the evolution of co-packaging technologies used in data center applications. Gen I-III have been deployed commercially, while IV and V are projected in the coming decade. Reprinted from N. Margalit, C. Xiang, S. M. Bowers, A. Bjorlin, R. Blum, and J. E. Bowers, “Perspective on the future of silicon photonics and electronics,” *Appl. Phys. Lett.*, vol. 118, no. 22, p. 220501, May 2021, doi: 10.1063/5.0050117, with the permission of AIP Publishing.

On the other hand, by eliminating the need for III-V native substrates, direct crystal growth methods promise easily scalable low-cost III-V integration solutions.[19] Nevertheless, they have yet to be adopted at an industrial level as fabricating reliable, high-

performance GaAs- or InP-based lasers on silicon has proven challenging.[20]–[22] During growth, dislocations nucleate to mediate lattice mismatch between the substrate and film and their ends thread upwards to the film surface.[22]–[25] These so called ‘threading dislocations’ have traditionally been the main limiting factor in both the performance and reliability of III-V lasers grown on Si.[20]–[22], [26]–[35] Where they intersect the device’s active region, they facilitate non-radiative recombination, degrading performance. The energy released causes dislocations to lengthen during device operation, a run-away degradation process ending in device failure.[20], [30], [31], [36] In conjunction with decades of work to reduce threading dislocation densities to 10^{6}–10^{7} cm^{-2},[37]–[41] use of more dislocation tolerant quantum dot based emitters substantially improved room-temperature device lifetimes from a few hundred hours to millions.[42]–[48] **Figure 1.3** presents an overview of improvements in room temperature device lifetimes.[49]

However, even using quantum dots and carefully designed threading dislocation filters, the lifetimes at industrially relevant temperatures for data center applications (65-85°C) remained short.[40] Using plan-view scanning transmission electron microscopy (PV-STEM), my colleagues and I identified an additional key, limiting defect: unexpected dislocations, termed ‘misfit dislocations,’ found lying flat at the uppermost and lowermost QD layers, in even record lifetime QD lasers.[46], [49]–[51] Using cathodoluminescence spectroscopy, we demonstrated that the misfit dislocations, have a much greater interaction area with the active region than threading dislocations and are potent non-radiative recombination centers.[52] Misfit dislocations generally form in layers exceeding a certain “critical thickness” during growth to mediate lattice mismatch.[53], [54] However, the active

region layers are designed to be misfit dislocation free.[25] Despite this, unexplained misfit dislocation formation has also been observed in nominally sub-critical thickness QW lasers.[35] Even more puzzling, in quantum-dot-in-quantum-well (DWELL) structures, the QDs provide a precipitate hardening effect that ought to hinder misfit dislocation formation.[55]

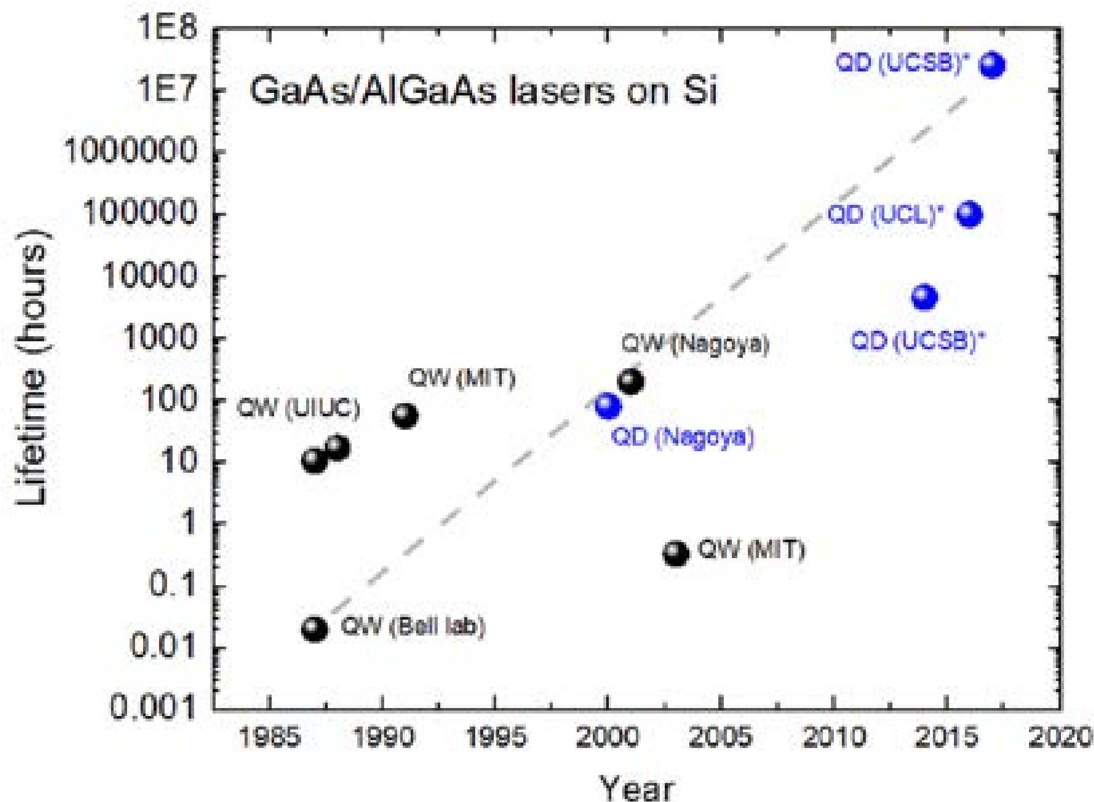

Figure 1.3 Room temperature lifetimes for experimental III-V lasers on silicon substrates over time. Reprinted with permission from D. Jung et al., "Recent Advances in InAs Quantum Dot Lasers Grown on On-Axis (001) Silicon by Molecular Beam Epitaxy," *Phys. Status Solidi A*, vol. 216, no. 1, p. 1800602, 2019, doi: 10.1002/pssa.201800602. © 2018 WILEY-VCH Verlag GmbH & Co. KGaA, Weinheim.

To explain their presence, my colleagues and I show that these MDs form through a previously unreported mechanism during sample cooldown due to the combined effects of (1) thermal expansion mismatch between (Al)GaAs and silicon and (2) mechanical hardening effects in the DWELL active region.[51] The MDs form when pre-existing threading dislocations glide in the cladding to relieve the increasing thermal stress, but are immobilized at the DWELLs. We hypothesized that this hardening arose from both the quantum dots' mechanical hardening and from previously reported alloy hardening[56] in the QW. My colleagues and I went on to validate said hypothesis: showing that by inserting a single indium-alloyed MD 'trapping layer' on both sides of the QD active region, we can engineer the local mechanical properties to shift MD formation away from the QD layers. While this is a somewhat unorthodox filtering strategy—it changes neither the total MD density nor the density of threading dislocations in the full device—we demonstrate that it substantially improves performance and reliability.[51], [57] In reliability studies on lasers without trapping layers, my colleagues and I identified extensive evidence of recombination-enhanced dislocation climb (REDC), a failure mechanism in GaAs-based lasers.[21], [46], [58], [59] In contrast, in devices with trapping layers, the vast majority of misfit dislocation formation is displaced to the doped cladding regions of the device; the trapped MDs show no evidence of REDC. **Table 1.1** presents power fit extrapolated lifetimes (failure criterion = time to double initial threshold current) for the highest performing device from Bowers group QD laser generations. The reader should note that, due to small sample sizes, these lifetimes are based on the highest performing devices. As such, fabrication variability, specifically voids in the p-cladding, plays a role in the reported numbers, helping to explain the apparent increase in lifetime with temperature in the Gen V.B set. Even despite these fabrication errors, my

colleagues and I demonstrate industrially relevant lifetimes at 80°C, with virtually no optimization. Based on these extremely promising results, early stage optimization efforts are already underway, and additional possible directions are proposed in **Chapter 7** of this work. In any case, although the III-V lasers presented here are preliminary materials designs fabricated into simple structures, they demonstrate that the more complex technologies required for photonic integrated circuits, once widely considered to be nearly impossible, are within reach.

Material Generation	**Innovation**	**TDD (cm^{-2})**	**TL position (nm)**	**pMD (cm^{-3})**	**Aging temp. (°C)**	**Extrapolated lifetime (hours) 35 °C**	**60 °C**	**80 °C**	**Reference**
Gen I	GaP/Si for remove APD	2×10^{8}	N/A	N/A	35	800			[40]
Gen II	TCA to reduce TDD	7×10^{7}	N/A	N/A	35	20 K			[40]
Gen III	SLS to reduce TDD	7×10^{6}	N/A	N/A	35	>1 M	2500		[40]
Gen IV	pMD for high T performance	7×10^{6}	N/A	5×10^{17}	60		70 K		[49]
Gen V.A		3×10^{7}	180	5×10^{17}	60		>1 M		[57]
Gen V.B	TLs to block MDs	3×10^{7}	80	5×10^{17}	60		80 K	100 K	[57]
Gen V.C		7×10^{6}	180	5×10^{17}	80			100 K	[60]
Gen VI	ASG filter for record low TDD	1×10^{6}	180	5×10^{17}	80			100 K	[60]

Table 1.1 Extrapolated lifetime values based on a ($y = a \times t^{b}$) power fit using 100% increase in threshold current for the failure criterion for the highest performing device from various QD laser generations in Bowers group. Temperature provides a significant accelerating factor in laser lifetimes, as shown. Red entries highlight devices with trapping layers. The reader should also note that fabrication variability (voids in the p-cladding) impacts the results of Gen V.A and Gen V.B, helping to explain the apparent increase in lifetime with increasing temperature in Gen V.B. Adapted from ref.[61] using most recent data from E. Hughes.

Although the thrust of this work is outlined in the preceding paragraphs, to assist the casual reader in their understanding, the Chapters in this thesis have been divided topically, rather than strictly chronologically. Thus, **Chapter 2** seeks to provide the reader with a baseline understanding of various electron microscopy methodologies used in reliability studies. Next **Chapter 3** discusses mechanical properties of crystalline systems in general as well as III-V semiconducting systems specifically. It focuses on the role dislocation motion plays in plastic flow and outlines the roles various metallurgical and thin film specific effects, including the formation of misfit dislocations in the active regions of QD lasers on silicon substrates. Next, **Chapter 4** provides the reader with an improved understanding of the optoelectronic behaviors of dislocations, discussing dislocations as non-radiative centers and recombination enhanced dislocation motion. Relying on the insight from **Chapters 2 – 4**, **Chapter 5** discusses various dislocation filtering and mitigation strategies. To lay the groundwork, I initially discuss various threading dislocation reduction strategies; this is followed by a full discussion of trapping layer implementation for misfit dislocation specific filtering. The subsequent discussion in **Chapter 6** serves to provide the reader with insight into various important failure mechanisms in semiconductor lasers in general, relying on the insight gained in the previous Chapters. This is followed by a discussion of the specific failure mechanisms we have observed to be active in our devices, recombination enhanced dislocation climb, and provides the reader with insight into how trapping layers substantially mitigate those processes. In the final Chapter, **Chapter 7**, I briefly conclude the important points discussed in the previous Chapters and launch into a more substantive discussion of interesting future experimental directions. Thus, **Chapter 7** may be the most interesting to readers whose goal is to continue the work outlined here.

Chapter 2:
Reliability Experimental Techniques

2.1 Introduction

While **Chapter 1** provides the reader with insight into the results composing the bulk of this thesis, it gives very little practical advice as to how my colleagues and I identified a strategy to improve 80°C lifetimes. Thus, the aim of this Chapter is to provide the reader with an overview of the microscopy-based failure analysis techniques employed. Ueda and Herrick can broadly characterize these techniques into two major categories: "high level" and "micron and sub-micron" inspection techniques. I, too, have found to be a useful formalism in my own thinking and in assisting others in their efforts to better understand why their devices are behaving the way they do. However, while most failure analysis can be done with optical microscopy, for detailed materials defects studies, micron and sub-micron techniques are often the only ones that can provide the necessary information. For this reason, and due in part to difficulties arising from the COVID-19 pandemic, the experiments presented in this thesis were performed entirely on electron microscopes. Likewise, some electron microscopy-based experiments were originally planned, but due to COVID-19 restrictions, were not possible in this time frame. Nevertheless, they deserve some discussion due to their importance in the field of semiconductor device reliability engineering in general.

2.2 High Level Optical Inspection Techniques

High-level inspection techniques can help to identify consistent problem areas and large scale nonuniformities. These techniques, in general, are simpler to perform than micron or submicron based alternatives and have fewer equipment requirements. A standard optical microscope, for example, can be used to identify large-scale fabrication errors such as obvious shorts, metal delamination, and scratches. Light emitting devices, like lasers and LEDs, lend themselves well to analyses like electroluminescence (EL) imaging, a technique in which the device is operated, and an optical microscope is used to map its local luminescence. Electrically active defective regions appear dark, and we describe them based on their shape (i.e., dark spot defects and dark line defects). Like other optical microscopy techniques, EL is useful in identifying problem areas and can be used as a guide for more detailed inspection techniques. Depending on the device geometry this can either be done from the backside, mapping the luminescence through the substrate or top-down. For Fabry-Perot lasers, the sample geometry used in the experiments outlined in the subsequent Chapters, EL is generally done from the backside. **Figure 2.1** shows three segments of a quantum dot laser imaged through the silicon substrate via electroluminescence. The arrows highlight dark lines defects both parallel and perpendicular to the laser bar.

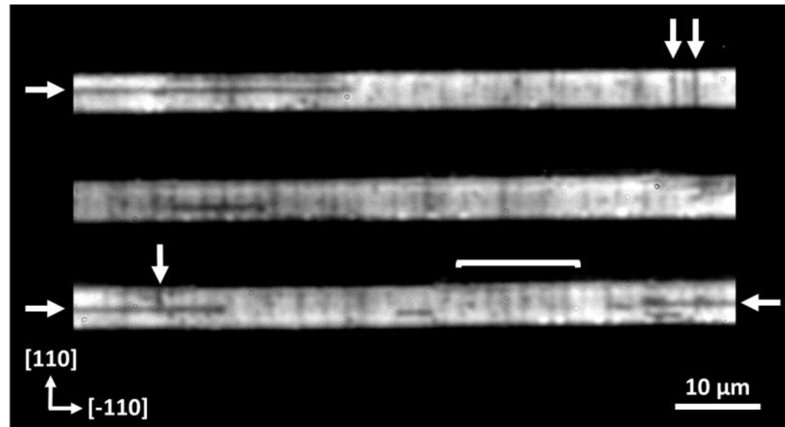

Figure 2.1 Three sections of an InAs QD laser structure imaged through the silicon wafer via electroluminescence. Arrows highlight examples of dark lines defects. After ref.[62]

2.3 Micron and Submicron Techniques

In addition to high-level optical microscopy-based techniques discussed, researchers have relied heavily on micron and submicron inspection techniques. The experiments described in the subsequent Chapters rely heavily on both scanning electron microscopy (SEM)-based techniques and transmission electron microscopy (TEM)-based techniques. As a wide variety of these methods have proven instrumental in this work, they warrant a full discussion.

2.3.1 SEM-Based Analyses

Universal Techniques

SEM uses a relatively low energy processing beam of electrons provide information about the sample's surface and a very shallow depth below it. It can be used to collect localized physical, chemical, and optoelectronic information. To assess physical structure, researchers often

measure Techniques measuring secondary electrons—those emitted as ionization products—and backscattered primary electrons (i.e., from the incident beam) provide insight into physical structure, as well as some limited chemical information. Electron backscatter diffraction based techniques are particularly important in mapping crystalline information and can be used for applications such as grain, phase, and defect mapping. One such technique used extensively in this work, Electron Channeling Contrast Imaging (ECCI), provides surface level structural defect visualization by relying on the localized changes in the backscattering behavior as shown in **Figure 2.2.** The yellow arrow indicates the location of a dislocation, made visible due preferential backscattering in its vicinity.

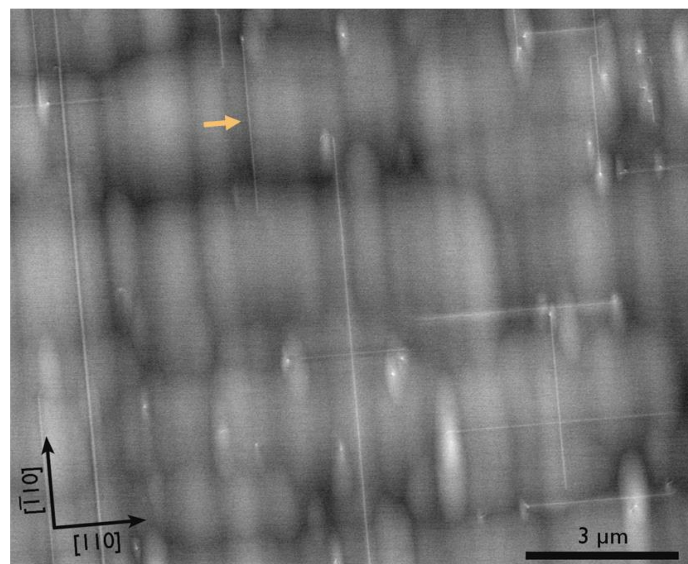

Figure 2.2 ECCI image of threading dislocations and near surface misfit dislocations (channeling condition = (400)/(220) in quantum dot model structure (for additional details see **Figure 4.3)** The orange arrow marks a misfit dislocation with a threading end that terminates at the film surface (point contrast at top).

In addition, both secondary electrons and backscattered electrons can provide some basic compositional information as heavier atoms will generate larger numbers of both secondary and backscattered electrons, a phenomenon known as mass contrast. The interactions between incident electron beam and core shell electrons in the atoms of sample also result in the generation of characteristic x-rays. Detecting these x-rays and mapping them, a technique referred to as energy dispersive x-ray spectroscopy (EDS), provides precise chemical information about the sample surface and a shallow depth beneath it. While not explicitly mentioned in the subsequent analysis, I relied heavily on compositional information, especially mass contrast imaging during sample preparation using both secondary electron and backscattered electron detectors. The ability to unambiguously distinguish indium containing layers from the surrounding material has proven critically important, as it enables precise localization of the areas of interest within these samples. **Figure 2.3** shows presents a side-view of a portion of a quantum dot laser being prepared for scanning transmission electron microscopy (STEM) analysis. The vertical dark stripe in the center of the sample is due to the higher average atomic mass in the quantum dot layers.

Figure 2.3 Through lens detector SEM image of plan-view scanning transmission microscopy foil of a laser active region in preparation. The dark vertical band down the center of the sample indicates a compositional change. In this case, this is due to the increased indium content in the active region.

Semiconductor-Specific Techniques

In semiconductors specifically, because the incident beam generates charge carriers, it is also possible to map the local optoelectronic properties of a sample using an SEM. Cathodoluminescence spectroscopy (CL), for example, uses a photodetection system to map the local luminescence behavior of the sample at each scan point. Thus, CL, like EL, can be used to map optically active defects. CL can have significant advantages as the analysis can be performed on undoped bare semiconductor, rather than requiring an operational device. CL systems with spectrum analyzers enable insight into precise localized wavelength information, as shown in **Figure 2.4**. In addition to providing insight into luminescence behaviors in

quantum dot materials, spectrally resolved CL information has also proven particularly important in the study of yellow defects in GaN systems.[63] Nevertheless, using CL to analyze full device structures has proven impractical in our case, as QD layers are far from the sample surface.

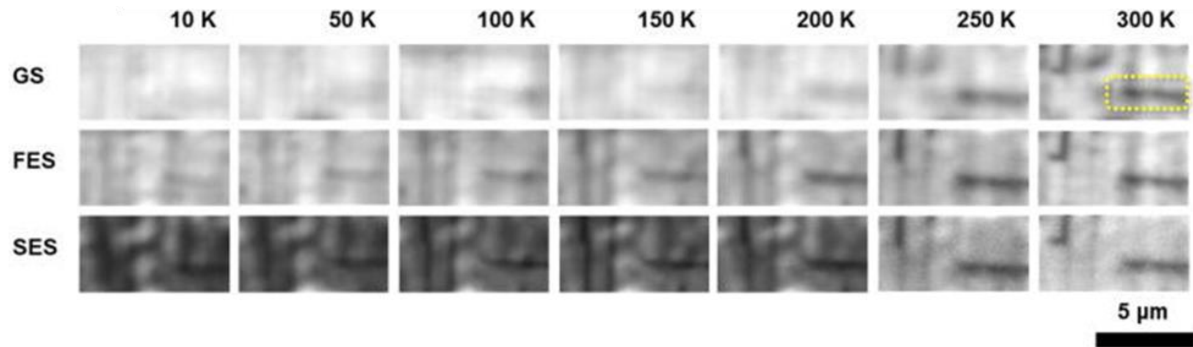

Figure 2.4 Wavelength filtered cathodoluminescence maps of quantum dot ground state (GS) emission, first excited state (FES) emission, and second excited state (SES) emission for a single, near-surface quantum dot layer across the temperature range 10 K–300 K. For additional details on sample structure, see **Figure 4.3**. Reprinted from J. Selvidge et al., "Non-radiative recombination at dislocations in InAs quantum dots grown on silicon," *Appl. Phys. Lett.*, vol. 115, no. 13, p. 131102, Sep. 2019, doi: 10.1063/1.5113517, with the permission of AIP Publishing.

Although I did not use electron beam induced current spectroscopy (EBIC), another SEM based optoelectronic analysis technique, in my work, it warrants mentioning as it offers some the advantages of both CL and EL. In complete circuits including a p-n junction or Schottky diode, the incident electron beam induces a measurable current response. This response is sensitive to the presence of electrically active defects, so their locations and relative impacts can be identified using a standard electrical multimeter. Unfortunately, however, this technique, like CL, is not well suited for analysis of our full lasers as the quantum dots active region is simply too far from the sample surface.

2.3.2 Focused Ion Beam (FIB) and SEM Dual Beam Analysis

Before moving on to a discussion of S/TEM based techniques, it is also worth mentioning SEM and focused ion beam (FIB) dual beam analyses. Focused ion beam systems use a beam of charged particles to irradiate the sample surface, in much the same way SEM systems do. However, due their much larger mass, the incident ions can be used to intentionally mill into samples to expose previously inaccessible material, in addition to facilitating sample imaging. For this reason, FIB is a critical tool in STEM and TEM sample preparation and cross sectional SEM analysis. One additional key feature of dual beam systems is the presence of a gas injection system (GIS). GISs flow metal-organic precursors into the path of the electron beam or ion-beam. When the incident beam interacts with the metal-organic gas it destabilizes the molecular bonds resulting in the deposition of the metal atom on the sample surface. This capability is critical for creating high quality FIB cross-sections and STEM samples alike. Although I performed my work using a Ga^{+} ion FIB system, many in the semiconductor community uses Xe^{+} plasma FIB systems for a variety of wafer scale failure analyses and to eliminate gallium implantation as a source of error. Although this effect is a concern, none of the conclusions in this work rely on precise chemical compositions.

2.3.3 S/TEM-Based Analyses

In both TEM and STEM systems, high energy (generally > 100 kV) electrons are transmitted through the full width of a thin sample. Various kinds of information (e.g., structural,

compositional, and opto-electronic) about the sample can be extracted by (1) measuring changes in the electron beam after it passes through the sample and (2) measuring the sample's response to the incident beam. The key difference between TEM and STEM is the shape of the electron beam: TEM uses a parallel electron beam that simultaneously images the entire sample, while STEM uses a converged processing beam with each pixel image sequentially. However, this change in beam shape, although quite simple to describe, involves a change in the lens layout, specifically, the removal of an objective lens. This change in lens layout uniquely suits STEM systems for the experiments performed in this work. Because the removed lens inherently introduces some degree of chromatic aberration in TEM systems, STEM systems substantially improve the spatial resolution in thick samples. **Figure 2.5** demonstrates this effect, showing two images of the same 1.1 μm thick sample, imaged with 100 kV excitation voltage in STEM (**Figure 2.5a**) and in conventional TEM (**Figure 2.5b**).[64]

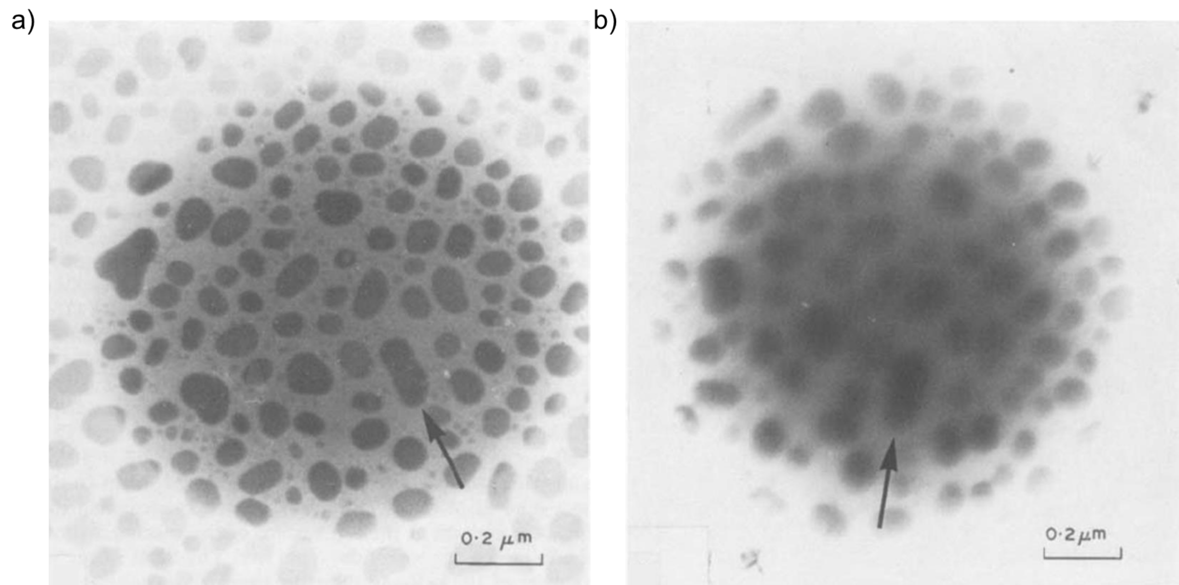

Figure 2.5 1.1 μm indium and polystyrene sample imaged with 100 kV excitation voltage in **(a)** STEM and **(b)** TEM modes. STEM mode provides substantially improved spatial resolution due to the elimination of objective lens chromatic aberration. Reprinted with permission from P. Gentsch, H. Gilde, and L. Reimer, "Measurement of the top bottom effect in scanning transmission electron microscopy of thick amorphous specimens," *J. Microsc.*, vol. 100, no. 1, pp. 81–92, 1974, doi: https://doi.org/10.1111/j.1365-2818.1974.tb03915.x, 1974 Blackwell Science Ltd.

Features of STEM Systems

STEM systems are designed to facilitate the simultaneous collection of both structural and compositional information and often include several annular detectors and a single circular detector as shown in the **Figure 2.6**. STEM annular detectors are commonly used to collect electrons whose path of travel has been changed due to interactions with sample. As this generally constitutes a relatively small fraction of the total transmitted electrons, we refer to these detectors as 'dark field detectors.' Annular detectors are also characterized by their collection angle. Those with a minimum acceptance angle greater than 100 mrad are characterized as high angle annular dark field (HAADF) detectors, while those with acceptance angles on the order of a few tens of mrad are referred to simply as annular dark

field (ADF) detectors. HAADF detectors are often used to collect high level compositional information because much of the signal arises from Rutherford scattering processes, which depend strongly on atomic number; while ADF detectors are commonly used to image strain contrast as their acceptance angles collect diffracted electrons. STEM systems often also include a circular detector that collects those electrons whose paths have not been significantly altered by features in the sample, an imaging modality referred to as 'bright field' (BF).

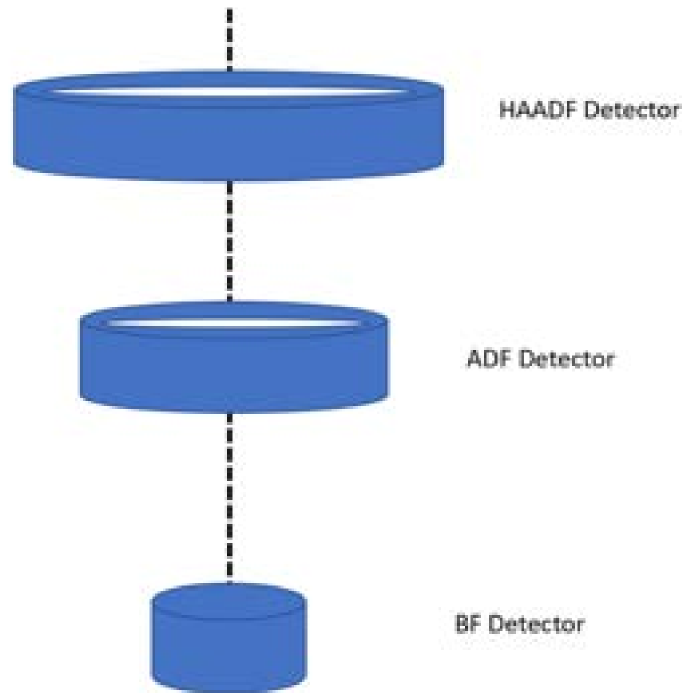

Figure 2.6 Standard STEM detector set-up. High angle annular dark field (HAADF) detectors have a minimum acceptance angle of ~100 mrad, annular dark field (ADF) detectors have a minimum acceptance angle on the order of a few 10s of mrad, and bright field circular detectors have a maximum acceptance angle of a few 10s of mrad.

While the three detector types mentioned in the preceding paragraph are the most common, TEM and STEM systems frequently come equipped with additional detector types

including EDS detectors and electron energy loss spectroscopy (EELS) detectors. Both these techniques are used for more advanced chemical analysis than simple HAADF imaging. Additionally, more exotic techniques including STEM-EBIC, STEM-CL, and TEM electron holography can be used to provide insight into the optoelectronic properties of semiconducting materials. These, however, are relatively uncommon. Nevertheless, in each case, as before, the information is extracted by measuring the response of the electron beam to the sample or the response of the sample to the electron beam.

Diffraction Contrast Imaging

Although the preceding Section offers some insight into the collection of structural, compositional, and optoelectronic information using STEM and TEM systems, diffraction contrast imaging techniques are the most frequently used for dislocation imaging and these do not require any specialized detectors in either TEM or STEM. Instead, they simply rely on the ability to carefully orient the sample with respect to the beam. Tilting the sample to specific positions leads to preferential diffraction of the incident electrons beam off specific crystalline planes. Often, the desired result is the splitting of the incident beam into a single transmitted spot and a single strongly excited diffracted spot, a condition referred to as two beam imaging. These conditions are identified by the set of planes associated with the strongly excited spot and are reported as $\boldsymbol{g} = \boldsymbol{hkl}$. An aperture is used such that the resulting image is formed from one of these beams. For two beam imaging in STEM, often the beam convergence angle is set such that the detectors themselves function as the aperture.[65]–[67] This is shown schematically in **Figure 2.7** (ref. [66]). Breaks in the crystal symmetry, such as dislocations

and stacking faults, generally diffract the incident beam more strongly than surrounding material. This is explained in more detail in **Chapter 3**. As a result, they appear as dark features in the transmitted image and bright features in the diffracted one, and these imaging modes are referred to as bright-field (BF) and dark-field (DF), respectively.

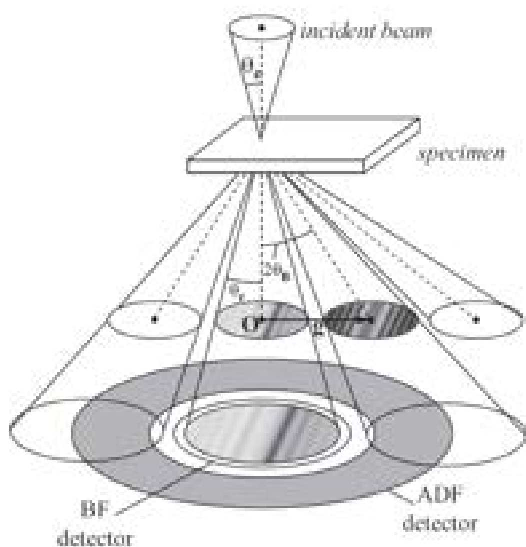

Figure 2.7 Illustration of two beam imaging configuration in STEM mode. Reprinted from *Ultramicroscopy*, 111/9, P. J. Phillips, M. C. Brandes, M. J. Mills, and M. De Graef, "Diffraction contrast STEM of dislocations: Imaging and simulations," 1483-1487, Copyright (2011), with permission from Elsevier.

Two-beam imaging is particularly useful when studying dislocations as their appearance can vary widely between diffraction conditions. In certain diffraction conditions ($\boldsymbol{g} \cdot \boldsymbol{b} = 0$) dislocations will appear invisible, a key tool in burgers vector ($\boldsymbol{b}$) identification. This, however, is an important consideration in dislocation counting and can be addressed by taking images in multiple diffraction conditions or with on-zone imaging.[65], [66] For additional information on burgers vectors, see **Chapter 3**.

It is also worth noting that STEM BF two-beam can provide improved resolution over BF-TEM when imaging dense dislocation networks. **Figure 2.8** compares the same dislocation networked imaged in BF-TEM (**Fig. 2.8a**) and BF-STEM (**Fig. 2.8b**).[68] This is because the convergent beam in STEM provides an averaging effect that reduces the background contrast from the dislocations' elastic fields, which facilitates distinguishing between closely spaced defects.

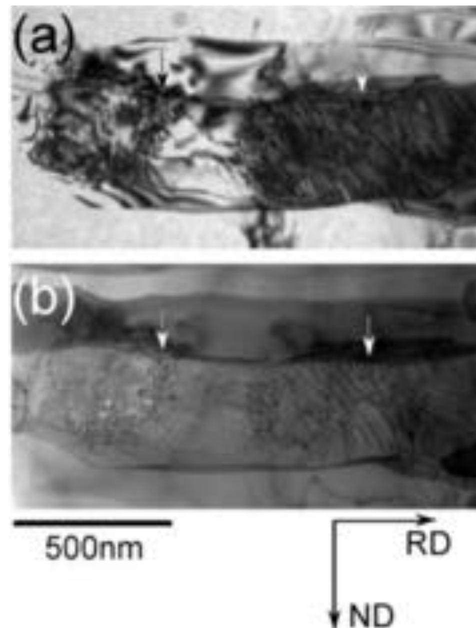

Figure 2.8 **(a)** TEM image and **(b)** STEM image of dislocation networks in highly deformed, high purity aluminum. Reprinted from *Mater. Sci. Eng. A*, 528/2, Y. Miyajima, M. Mitsuhara, S. Hata, H. Nakashima, and N. Tsuji, "Quantification of internal dislocation density using scanning transmission electron microscopy in ultrafine grained pure aluminium fabricated by severe plastic deformation," 776-779, Copyright (2010), with permission from Elsevier. From ref.[68]

Special Considerations when Imaging Dislocations in Quantum Dot Systems

Dislocation imaging whether in an SEM or a TEM, as discussed in the previous Sections, is done using strain contrast based techniques. However, this can prove somewhat problematic

when imaging dislocations in quantum dot materials for the simple reason that quantum dots themselves generate significant strain contrast. Traditionally, most dislocation analysis in thin film systems is performed using cross-sectional S/TEM imaging, but in QD systems this can lead to very ambiguous contrast, making dislocations very easy to overlook.

Figure 2.9 presents an example of this effect. I intentionally lifted out this foil along the [100] direction such that all the in-plane misfit dislocations, marked with black arrows, will appear the same length (proportional to the foil thickness). To increase the clarity, I also performed contrast enhancement in post-processing. Even so, the strain contrast from the misfit dislocations is very difficult to distinguish from the contrast due to the dots themselves. Unfortunately, in more conventional [110] lift out orientations, misfits will appear as black dots (see ref.[49]) that are nearly indistinguishable from the dots themselves or as long segments of slightly increased contrast. Depending on the length of the misfit dislocation segments parallel to the [110] oriented foil, the slight increase in contrast can extend for the length of the foil. Thus, although the [100] geometry can offer a stop-gap imaging solution, generally plan-view imaging techniques are far more appropriate when trying to make a conclusive statement about the presence or absence of dislocations near quantum dots.

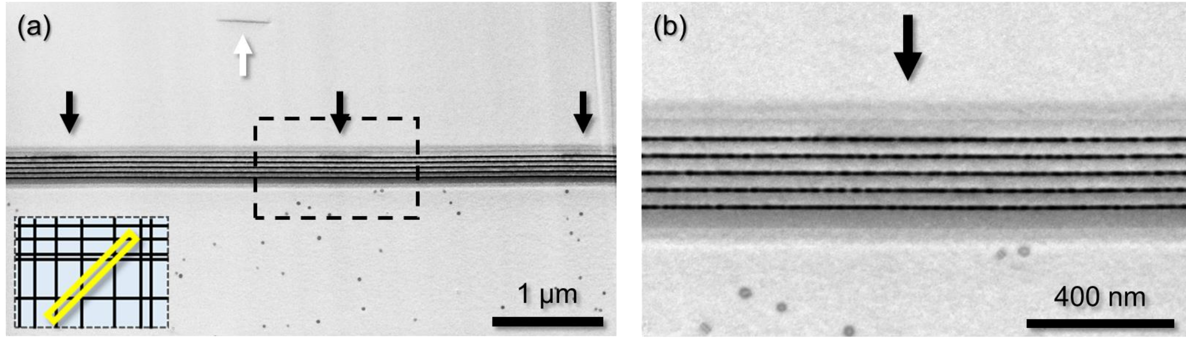

Figure 2.9 (a) Cross-sectional scanning transmission electron microscopy image of misfit dislocations lying at the uppermost quantum dot layer in a quantum dot laser stack imaged along the [100] zone axis. Because the lift-out geometry (inset) ensures all the misfit dislocations will appear the same length, we can use that to identify them. Black arrows mark the locations of QD adjacent misfit dislocations while the white arrow denotes a misfit dislocation elsewhere in the structure. Post-processing contrast-enhancement was used to maximize misfit dislocation visibility. **(b)** At higher magnification (boxed area in (a)), the misfit dislocation's strain contrast is rendered nearly invisible by the quantum dots own strain contrast.

Electron Tomography for Dislocation Studies

Although cross sectional dislocation imaging is often difficult and unreliable in quantum dot systems, cross sectional information may still be necessary. To address this need, I used specialized electron tomography to perform parts of the analysis discussed in the subsequent Chapters. Electron tomography, in general, involves the acquisition of a relatively large number of images taken at different tilts for the same sample area. From this set of images, the positions of various features with respect to each other can be unambiguously determined. **Figure 2.10** provides a schematic representation of the basic process.[69] Variants of the fundamental technique can be performed using both TEM and STEM systems. These methods have been successfully applied to a variety of biological and materials science problems.

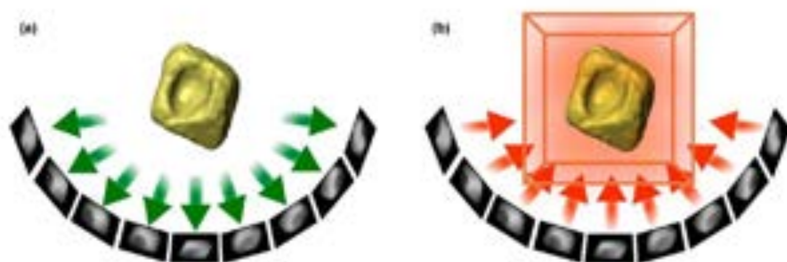

Figure 2.10 Schematic representation of **(a)** the acquisition of a 2D image "tilt series" and **(b)** back-projection of these images to obtain a 3D reconstruction. Reprinted (adapted) with permission from R. Leary, P. A. Midgley, and J. M. Thomas, "Recent Advances in the Application of Electron Tomography to Materials Chemistry," *Acc. Chem. Res.*, vol. 45, no. 10, pp. 1782–1791, Oct. 2012, doi: 10.1021/ar3001102. Copyright (2012) American Chemical Society.

Dislocation tomography, the specific application relevant to this work, is generally performed by following a specific diffraction condition during the acquisition of the tilt series. Imaging with different portions of the signal has provides researchers, including myself, a great deal of flexibility. Techniques utilizing the transmitted beam,[70]–[72] a single strongly excited diffracted spot,[67] a single weakly excited diffracted spot,[73], [74] several higher order reflected beams,[75], [76] and systematic row imaging using the transmitted spot a small number of low angle diffracted spots[50], [51] have all been demonstrated to work well. Some researchers report that STEM based techniques provide improved reconstructions due to the convergent beam's inherent averaging effect, which suppresses contrast variation due to slight changes in specimen thickness and diffraction condition.[67], [71] Note also that diffraction contrast based tomography is particularly well suited to imaging quantum dots, as they too have significant strain contrast. **Figure 2.11** presents a sample plan-view (top down) diffraction contrast BF-STEM image from tomographic reconstruction series and the associated reconstruction (**Figure 2.11a** and **Figure 2.11b**, respectively). The strain contrast

from the quantum dots allows us to identify five distinct layers, and the additional contrast from the dislocation allows us to localize it at the fifth dot layer.

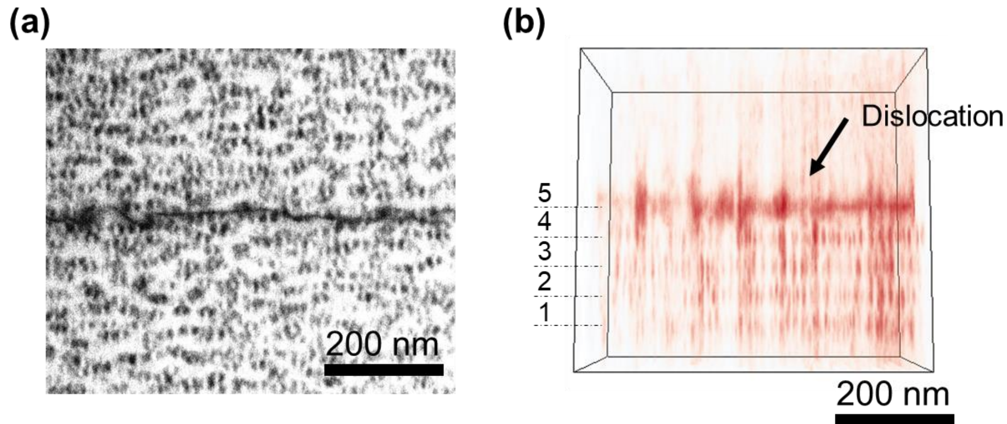

Figure 2.11 (a) Bright field plan-view scanning transmission electron micrograph ($\boldsymbol{g} = \mathbf{220}$) showing a misfit dislocation among a field of quantum dots from the active region of a lifetime tested InAs quantum dot laser on silicon. **(b)** The tomographic reconstruction reveals that the misfit dislocation lies at the fifth quantum dot layer. Reprinted from J. Selvidge et al., "Defect filtering for thermal expansion induced dislocations in III–V lasers on silicon," *Appl. Phys. Lett.*, vol. 117, no. 12, p. 122101, Sep. 2020, doi: 10.1063/5.0023378, with the permission of AIP Publishing.

2.4 Summary

Defects in semiconductors lend themselves well to both structural and optoelectronic microscopy characterization using optical microscopy, SEM-based techniques, and S/TEM based techniques. Optical microscopy based techniques provide insight into large scale features, while electron microscopy based techniques are better suited for detailed micron-scale characterization. In general, SEM based techniques are only suited to surface and shallow depth characterization studies, while S/TEM techniques provide improved insight

for studying buried device regions. Diffraction based techniques in both SEM and S/TEM systems can be particularly powerful in understanding defect structures, but, for our system, the quantum dots' own strain contrast can be a complicating factor, especially in S/TEM cross-sectional analyses. Techniques like electron tomography offer alternative pathways to access similar cross sectional information using plan-view imaging.

Chapter 3

Mechanical Behaviors of III-V Systems

3.1 Introduction

The mechanical properties of ductile crystalline materials, including semiconductors at elevated temperatures, arise due to the presence of defects in the system. Although a variety of defects are important in understanding their mechanical properties, dislocations are of particular importance. As such, the aim of this Chapter is to provide the reader with insight into the properties of dislocations, both in general, and in III-V zinc-blende thin film semiconductors, specifically. The influence of additional structural and compositional features on the behavior of dislocations are discussed. The Chapter concludes with a discussion of both the traditional dislocation formation mechanism in thin films and the alternative pathway we identified during this work.

3.2 Dislocations in Crystals

3.2.1 Fundamentals

A dislocation is a missing or extra half plane of atoms in a crystal that, in general, are nucleated to relieve mechanical stress. Although it is a simplification, for convenience, we often think of them as an extra half plane of atoms as terminating in a line of dangling atomic bonds.

However, while dislocations are nucleated to relieve global strain fields, they themselves generate a local strain field. Nearby atomic bonds are stretched and compressed to accommodate extra half plane as shown in **Figure 3.1**. The deformed bonds, as well as the broken bonds along the dislocation core itself, result in a localized break in the overall symmetry of the crystal. We describe dislocations using two vectors: the line's direction **u** and a vector describing the magnitude and direction of the associated lattice distortion, referred to as the Burgers vector **b**. In **Figure 3.1a**, the dislocation's line direction is perpendicular to the plane of the page and its Burgers vector points to the right.

In naming dislocations, we describe the relationship of these two vectors to each other. An edge dislocation describes a dislocation in which the line direction and burgers vector are perpendicular to one another. In the case where the line direction and the burgers vector are parallel, the dislocation is referred to as screw type. Dislocations with line directions that are neither perpendicular nor parallel to their Burgers vectors are referred to as mixed as they have both screw components and edge components. However, while the Burgers vector is a fixed a single dislocation will often have multiple different line directions along its length. **Figure 3.1b** provides an example of this, showing a dislocation with screw, edge, and mixed regions.

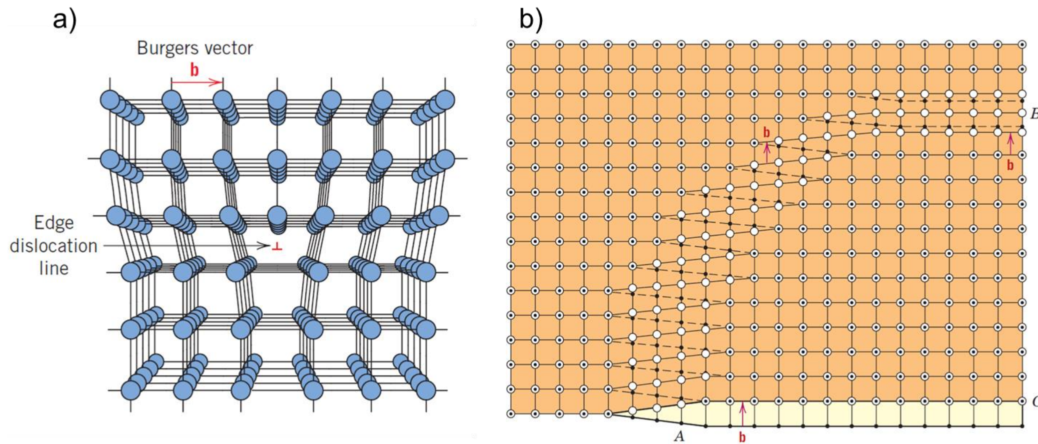

Figure 3.1 (a) 3D schematic representation of atomic positions around an edge dislocation; the line direction **u** is perpendicular to the page. **(b)** Top down representation of a dislocation that has edge, screw, and mixed character portions along its length. Open and closed circles denote atomic positions above and below the slip plane, respectively. The dislocation is pure screw at point A and pure edge at point B. After ref.[77]

3.2.2 Dislocation motion

Glide Mechanism

Glide occurs in response to mechanical stress through a 'slip' process whereby bonds are atomic broken and reformed, allowing the dislocation line to move, while the atoms themselves remain relatively stationary. The motion is "conservative" meaning it does not involve the addition or removal of atoms and is constrained to planes containing both their defining vectors (**b** and **u**). This process of bond-rearrangement occurs most readily between atoms on close packed planes along close packed directions. We refer to these combinations of planes and line directions as the system's primary slip systems. When a dislocation's glide plane is a primary slip plane for the system, we refer to it as 'glissile', meaning able to glide,

dislocations who do not satisfy this criterion are referred to as 'sessile'. In general, this process occurs readily for screw type dislocations (**b**||**u**), which can glide on any of the primary slip planes of a system. Note that for a dislocation to glide the applied mechanical stress must have some shear component that acts along its glide plane.

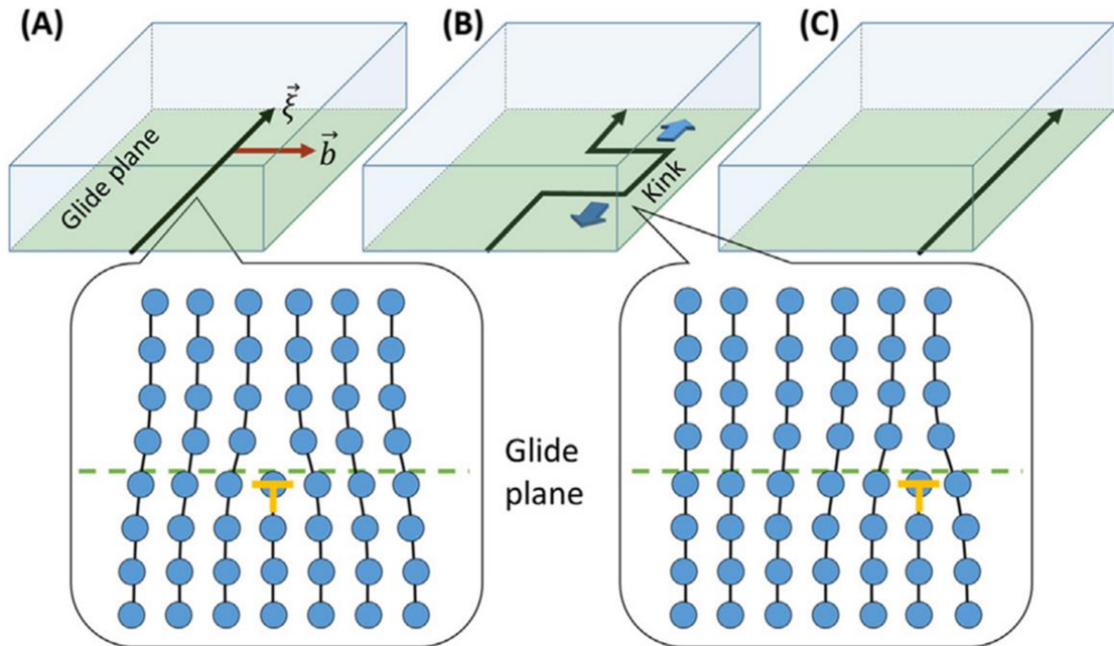

Figure 3.2 (a) Schematic showing the atomic structure of an edge dislocation and its glide plane (green). The glide plane contains both the line direction (referred to here as ξ) and the Burgers vector **b**. **(b)** An atomic scale excursion of the dislocation (kink) forms in the glide plane and expands laterally. **(c)** The expansion of the kink eventually leads to the dislocation moving rightward by |**b**|. Reprinted from *Reliability of Semiconductor Lasers and Optoelectronic Devices*, K. Mukherjee, "Chapter 4 - Materials science of defects in GaAs-based semiconductor lasers," 113-176, Copyright (2021), with permission from Elsevier.

As simultaneous rearrangement of the bonding along the entire length of a dislocation line is both energetically and statistically unlikely, the motion instead happens via excursions in the dislocation line on the order for a few atoms, which expand over time. **Figures 3.2a-**

3.2c (ref. [78]) show this process schematically. For double kink-formation to occur the excursion must overcome the short-range, interatomic Peierls stress, τ_p (~4 GPa in GaAs[79]). This happens readily with relatively small resolved shear stresses at elevated temperatures; but it is prohibitive at room temperature leading GaAs's observed brittle characteristics in this temperature range.[80] We can model the thermal glide velocity (note that this is distinct from the recombination enhanced glide velocity) using the following equation from Alexander and Haasen:

$$v = v_0 \left(\frac{\tau_{ex}}{\tau_0}\right)^m \exp\left(-\frac{Q}{k_B T}\right)$$

where τ_{ex} is the net resolved shear stress measured in MPa, v_0, m, and Q are experimentally determined parameters, and $\tau_0 = 1$ MPa.[81] Note that all three experimentally determined parameters (including the exponential terms) are dependent on factors such as the dislocation's line direction. Yonenaga and Sumino report that this can vary significantly between different dislocation types within a single GaAs based sample.[82] Likewise, they report that electrically charge impurities, generally referred to in the semiconductor community as 'dopants' can dramatically influence these parameters as well as shown in **Figure 3.3**. Indeed, they show that screw dislocation velocities in GaAs doped with silicon (n-type) can be as much as four orders of magnitude lower than screw dislocation velocities in GaAs doped with zinc (p-type) for a given temperature (550 °C in the case of **Figure 3.3**).

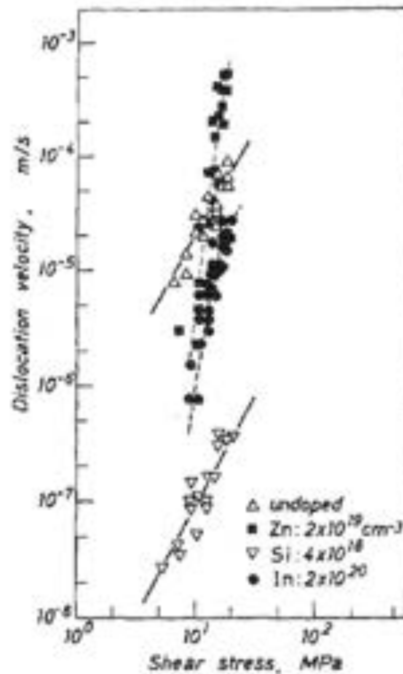

Figure 3.3 Screw dislocation velocity as a function of applied stress (three point bending) at 550°C in undoped GaAs and GaAs with acceptor (Zn), donor (Si), and isovalent (In) impurities. Reprinted from I. Yonenaga and K. Sumino, "Impurity effects on the generation, velocity, and immobilization of dislocations in GaAs," *J. Appl. Phys.*, vol. 65, no. 1, pp. 85–92, Jan. 1989, doi: 10.1063/1.343380, with the permission of AIP Publishing.

Additional Mechanical Hardening Effects

The dramatic reduction in glide velocities in n-doped GaAs samples are an example of a much broader phenomenon referred to as 'mechanical hardening.' As **Figure 3.3** demonstrates, dislocation glide can be hindered even at higher temperatures by impurities; features such as precipitates and grain boundaries can also provide similar effects. This is because these features, much like dislocations, generate localized athermal stress fields portions of which oppose glide.[83]–[87] Indeed, dislocation glide can even be hindered by the presence of large numbers of other dislocations.[54] Even small compositional fluctuations, such as those that

occur in a random alloy been observed to provide in plane stress fields, leading to mechanical hardening effects in several semiconductor systems including in SiGe,[88] GaAsP,[89] and low-indium InAlGaAs alloys.[56] **Figure 3.4** and **Figure 3.5** compare the extent of recombination enhanced dislocation glide (REDG) (for a fuller discussion of REDG see **Chapter 4**) observed in $In_x(Al_{0.15}Ga_{0.85})_{1-x}As/In_x(Al_{0.25}Ga_{0.75})_{1-x}As$ heterostructures on silicon for x=0 (**Figure 3.4**) and x=0.05 (**Figure 3.5**). In the latter case, an overshoot layer was added to ensure the strain state in the film was equivalent. **Figures 3.4a-b** present selected CL images from early and late in the image series, respectively. From these images, the paths and speeds of various glissile dislocations were tracked, as presented in **Figure 3.4c**. Note that the inclined paths arise due to substrate offcut.

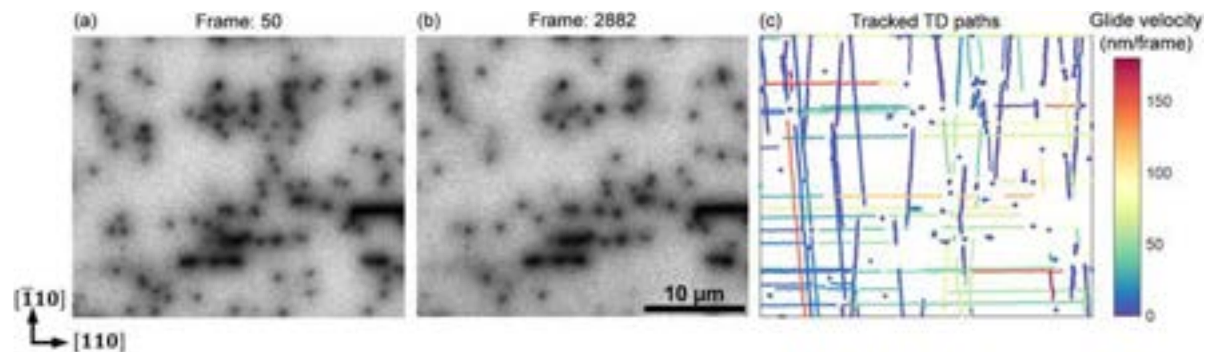

Figure 3.4 Panchromatic cathodoluminescence map from an $Al_xGa_{1-x}As$ heterostructure showing threading dislocations as dark spots. The images selected imaged were taken after **(a)** 50 frames and **(b)** 2882 frames. Some dislocations have undergone REDG and exited the imaging area. **(c)** Tracks of the gliding threading dislocations from the same area, colored by the glide velocity. The substrate offcut results in inclined paths. Reprinted from E. T. Hughes, R. D. Shah, and K. Mukherjee, "Glide of threading dislocations in (In)AlGaAs on Si induced by carrier recombination: Characteristics, mitigation, and filtering," *J. Appl. Phys.*, vol. 125, no. 16, p. 165702, Apr. 2019, doi: 10.1063/1.5088844, with the permission of AIP Publishing.

The addition of 5% indium to the structure reduces the observed threading dislocation speed by approximately 20X, despite an equivalent driving force and equivalent illumination

conditions, as shown in **Figure 3.5**. In this case, even though InAs is softer than GaAs, the difference in covalent radii[90] between gallium (124 pm) and indium (142 pm) leads to a varying stress field which opposes glide.

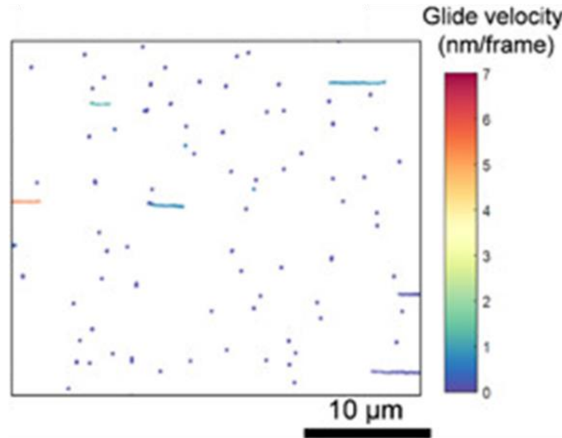

Figure 3.5 Tracks of threading dislocations undergoing REDG colored by their velocity in $In_{0.05}(Al_xGa_{1-x})_{0.95}As$ heterostructure with overshoot layer. Despite the equivalent driving force to **Figure 3.4**, most threading dislocations are stationary. The few that do move have dramatically reduced glide velocities. Reprinted from E. T. Hughes, R. D. Shah, and K. Mukherjee, "Glide of threading dislocations in (In)AlGaAs on Si induced by carrier recombination: Characteristics, mitigation, and filtering," *J. Appl. Phys.*, vol. 125, no. 16, p. 165702, Apr. 2019, doi: 10.1063/1.5088844, with the permission of AIP Publishing.

Climb

Dislocations can also move and change in length by absorbing and/or emitting point defects. Thus, it is generally a 'non-conservative' process. We classify climb by whether the extra half plane of atoms is contracting (positive climb) or expanding (negative climb). **Figure 3.6** (ref. [78]) presents a dislocation undergoing negative climb, by expelling vacancies into the crystal. Much like dislocation glide, dislocation climb occurs in small unit steps, referred to as 'jogs,' which expand outwards, as shown in **Figure 3.6b**. However, unlike kink formation, as jog

formation and expansion necessitate the participation of point defects, climb can effectively be halted due to an opposing chemical driving force (e.g., local depletion of the required interstitial atoms), referred to as an osmotic potential. However, just as chemical driving forces can oppose climb, they can also enable it. For example, in our system we observe negative climb, which we expect is driven in part by an undersaturation of Ga vacancies at relevant temperatures.[50] Dislocations can also climb in response to a mechanical stress, however, as glide occurs far more readily, this occurs primarily in cases where there is not a net shear acting along the glide plane.

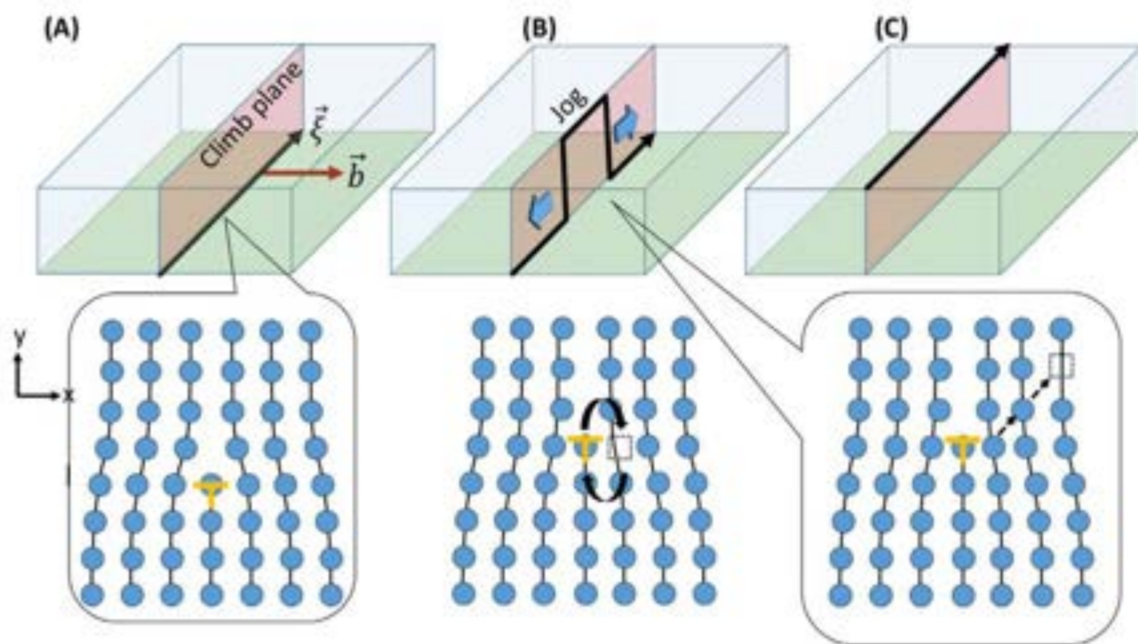

Figure 3.6 Schematic of an edge dislocation undergoing negative climb by emitting vacancies. **(a)** The climb plane (red) is orthogonal to the Burgers vector **b**. **(b)** The edge dislocation emits a vacancy, creating an upward excursion in the climb plane (jog). The jog expands laterally by emitting additional vacancies such that **(c)** the dislocation has climbed upward a distance equal to the jog height. If conditions permit, the vacancies diffuse away from the dislocation core, if they do not, osmotic pressure builds, opposing further climb. Reprinted from *Reliability of Semiconductor Lasers and Optoelectronic Devices*, K. Mukherjee, "Chapter 4 - Materials science of defects in GaAs-based semiconductor lasers," 113-176, Copyright (2021), with permission from Elsevier.

3.3 Dislocations in Zinc-Blende Thin Films

In hetero-epitaxially grown zinc-blende semiconductors, mixed type 60° dislocations are of particular interest. It is more energetically favorable accommodate the lattice distortion associated with these dislocations over a larger area. **Figure 3.7** shows two 60° dislocations at an $In_{0.08}Ga_{0.92}As$/GaAs interface. The dislocation in **Figure 3.7a** that has dissociated into a 30° and a 90° partial dislocation bounding a planar defect (stacking fault), while the dislocation in **Figure 3.7b** remains perfect. The red line in **Figure 3.7b** indicates the position of the extra half plane of atoms.

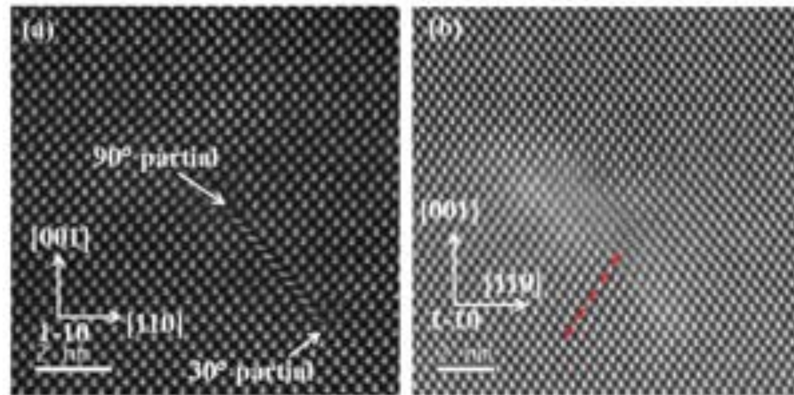

Figure 3.7 Aberration corrected HAADF-STEM images of **(a)** dissociated and **(b)** perfect 60° dislocations at an $In_{0.08}Ga_{0.92}As$/GaAs interface. The red line in (b) marks the extra half plane. After ref.[91]

Dislocations in GaAs based compounds can either terminate on either the group III or the group V sublattice. **Figure 3.8** shows the structure of 30° and 90° partial dislocations for both arsenic and gallium terminated dislocation types; these are referred to as α and β type dislocations, respectively. Although the differences between these two structures are relatively

subtle, their behaviors are quite distinct: Yonenaga and Sumino report an order of magnitude increase in dislocation velocities in α dislocations over β dislocations.[82], [92]

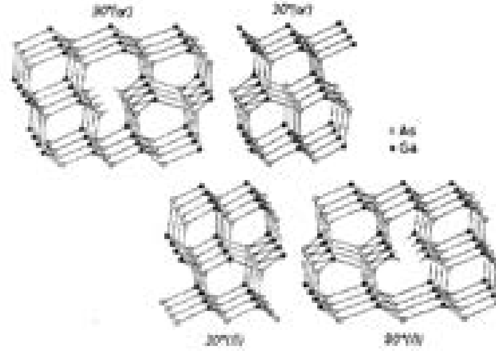

Figure 3.8 30° and 90° partial dislocation structures for arsenic-terminated α and gallium-terminated β dislocations. Reprinted from I. Yonenaga and K. Sumino, "Effects of In impurity on the dynamic behavior of dislocations in GaAs," *J. Appl. Phys.*, vol. 62, no. 4, pp. 1212–1219, Aug. 1987, doi: 10.1063/1.339672, with the permission of AIP Publishing.

In thin films, we are often also concerned with the angle between the dislocation's line direction and the film growth direction. We refer to dislocations with some component of their line direction in the growth direction as 'threading dislocations' and dislocations that lie directly in the growth plane (have no component of their line direction in the growth direction) are referred to as 'misfit dislocations'. **Figure 3.9** shows an example of a dislocation with both a MD segment and a TD segment.

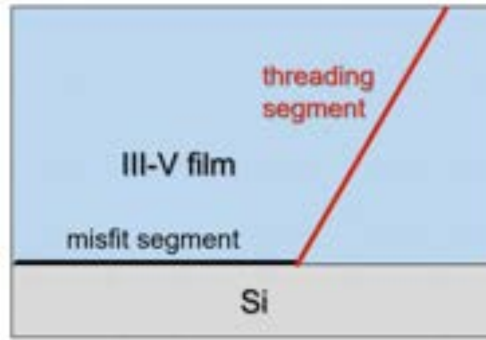

Figure 3.9 Diagram of a dislocation in a III-V film on a silicon substrate with a misfit dislocation segment (black) at the interface, and a threading dislocation segment (red) extending from the interface to the surface of the film.

3.3.1 Thin Film Dislocation Formation and Motion Mechanisms

Lattice Mismatch

Misfit dislocations, as their name implies, form at the interface between two dissimilar materials to mediate their lattice mismatch in most cases. For the simple case of a single lattice mismatched layer grown on a substrate with a pre-existing threading dislocation, the Matthews-Blakeslee critical thickness describes the layer thickness, h_c, above which dislocation glide in the threading segment in the upper layer becomes energetically favorable. Below this thickness, although the layer experiences net shear forces due to the lattice mismatch, the dislocation's line tension is sufficient to prevent glide. **Figure 3.10** shows the critical thickness for an $In_xGa_{1-x}As$ layer grown on GaAs as a function of indium fraction, assuming an anisotropic and isotropic calculation of the biaxial Young's Modulus. However, for device design purposes, strain thickness product, based on the assumption that the misfit dislocation should not generate more strain than it relieves, is often a more useful metric.[93]

Below a strain thickness product of 20 nm% the layer remains pseudomorphic (i.e., misfit dislocation formation does not occur).[94], [95]

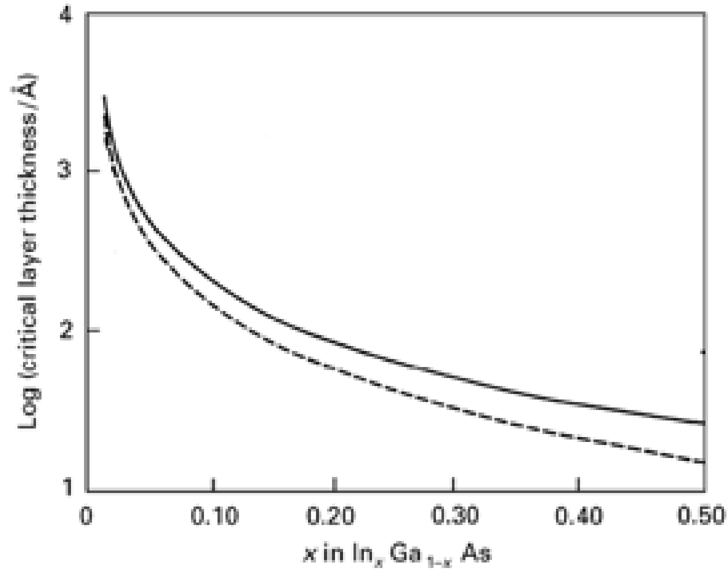

Figure 3.10 $\log(h_c)$ for a single $In_xGa_{1-x}As$ on GaAs as a function of $In_xGa_{1-x}As$ composition calculating the anisotropic Young's modulus (—) and assuming an isotropic Young's modulus (---). Reprinted by permission from Springer Nature Customer Service Centre GmbH: Springer Nature, *Journal of Materials Science: Materials in Electronics*, "Strain and strain relaxation in semiconductors," D. J Dunstan, © 1997 Chapman & Hall.

Under certain circumstances, the dislocation density in a substrate is insufficient to relieve the strain arising from lattice mismatch. As a result, additional dislocations are nucleated through processes such as half loop nucleation whereby a dislocation forms at the film surface and glides downward to the interface. This results in a misfit segment lying at the interface with threading segments that extend to the surface on either end. This process is important in the plastic relaxation of GaAs-based films deposited on silicon wafers, as these systems have substantial lattice mismatch (4% compressive), and Si substrates are effectively

defect-free. Additionally, in cases where there are some existing threatened dislocations, spiral and Frank-Read multiplication processes can help to increase the overall dislocation density as well.[54]

Thermal Expansion Mismatch

Due to a substantial thermal expansion coefficient mismatch between GaAs and silicon ($\alpha_{GaAs} - \alpha_{Si} \approx 3 \times 10^{-6}$ K^{-1}), tensile stress builds in thick GaAs-on-Si films during cooldown. But the measured 0.15–0.17% tensile elastic strain is lower than expected,[96] consistent with plastic relaxation via dislocation glide during cooldown. As is the case in **Figure 3.4**, the incident SEM beam enables dislocation glide at room temperature via REDG (see **Chapter 4** for additional details on REDG), allowing us to observe this process continue at room-temperature, as shown in **Figure 3.11a**. As carrier recombination does not induce a driving force for glide and nearly equally lattice-mismatched GaAs-on-GaP structures ($\alpha_{GaAs} - \alpha_{GaP} \approx 1 \times 10^{-6}$ K^{-1}) of similar thickness show no evidence of *in situ* REDG,[97] this motion must be a result of the residual thermal stress.

The reader should note that the GaAs-on-Si thermal-strain relaxation behavior is quite distinct from classical misfit dislocation formation due to lattice mismatch. Firstly, rather than nucleation and growth of tensile-strain relieving misfit dislocations by the standard mechanism (**Figure 3.11b**), we expect that relaxation occurs through (1) reverse glide of pre-existing threading dislocations shrinking their compressive-strain-relieving misfit dislocation segments (**Figure 3.11c**) and (2) vertical glide of entire compressive-strain-relieving misfit dislocation segments (**Figure 3.11d**). Note that as the relevant misfit dislocation segments are buried deep below the sample surface, we cannot resolve them using SEM based techniques;

for additional detail on ECCI and other SEM-based characterization methods, refer to **Chapter 2**. Secondly, the relaxation process occurs spontaneously: extending a misfit segment leads to a line tensional force that opposes glide, but the line tension of a shrinking misfit segment acts in the direction of glide and thus pulls the threading dislocation along.

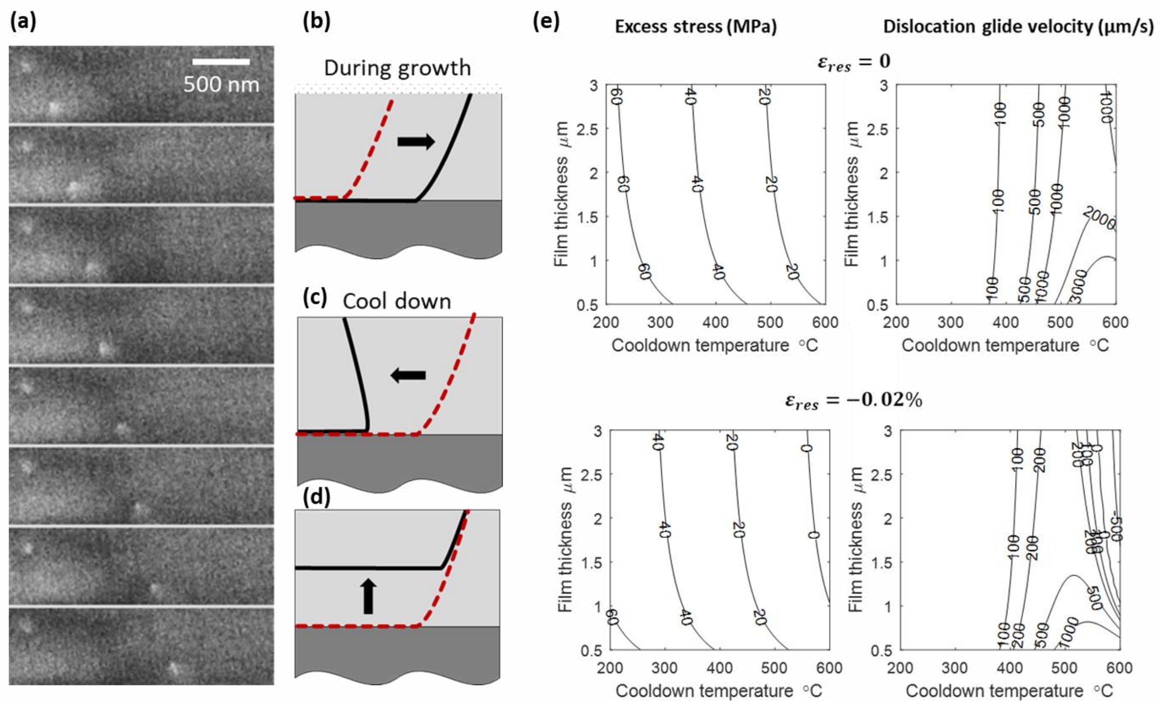

Figure 3.11 (a) Time-lapse electron channeling contrasting imaging sequence of showing recombination-enhanced threading dislocation glide (one moving and one stationary) due to thermal mismatch strain. **(b)** Schematic of classical misfit dislocation formation mechanism, this occurs during growth to form compressive-strain-relieving misfit dislocations at a GaAs/Si interface. However, plastic relaxation does not occur through this pathway during cooldown. Instead, the system removes the existing compressive-strain-relieving misfit dislocations **(c,d)** through **(c)** reverse glide of the existing threading dislocations, as shown in (a), and **(d)** upward glide of the misfit dislocation segments. **(e)** Excess stress on the threading dislocation segment and corresponding dislocation glide velocity for an α-type core in undoped GaAs calculated for a GaAs/Si structure with two values of residual compressive strain 0% and 0.02% at the end of the growth. The former case results in spontaneous dislocation motion due to a persistent positive excess stress. After ref.[62]

To better understand this counterintuitive effect, it is useful to apply the concept of excess stress on a TD developed by Dodson and Tsao,[98] and expanded upon by [99]–[101]. By this formalism, the excess stress, τ_{ex}, on the TD segment is given by the sum of the resolved shear stress on the glide plane in the direction of the Burgers vector, τ_{rs} and the interfacial misfit dislocation's line tension, τ_l, i.e., $\tau_{ex} = \tau_{rs} + \tau_l$. In this case, a positive value of τ_{ex} provides a driving force for MD contraction. Assuming no plastic relaxation, the biaxial strain ε during cool down from a growth temperature, T_{gr}, to a temperature, T, is:

$$\varepsilon = (\alpha_{GaAs} - \alpha_{Si})(T_{gr} - T) + \varepsilon_{res},$$

where ε_{res} is the post-growth residual strain at T_{gr}. Thus, for a given film thickness (h), we have:

$$\tau_{rs} = 2\mu\varepsilon \sin\alpha \cos\alpha \sin\beta \left(\frac{1+\nu}{1-\nu}\right)$$

and

$$\tau_l = \frac{\mu b \cos\alpha\,(1 - \nu\cos^2\beta)}{4\pi h(1-\nu)} \log\left(\frac{4h}{b}\right).$$

Here, μ is the shear modulus of the film (assumed to be equal to the shear modulus of the substrate) and Poisson's ratio $\nu = 0.3$. α is the inclination angle of the glide plane to the interface normal (α = 54.74°); β is the angle of the Burgers vector $\vec{b}$ and the MD line direction (β = 60° or 120°). For simplicity we assume a dislocation cut-off radius of $b/2$.

Assuming T_{gr} = 600 °C, **Figure 3.11e** shows how τ_{ex} varies as a function of h and T for two cases: $\varepsilon_{res} = 0$ and $\varepsilon_{res} = -0.02\%$ (compressive strain). In the former case, τ_{ex} is

positive for all thicknesses at all points during cool down. While in the latter case, the misfit dislocations initially expand (τ_{ex} is negative) before they begin to contract. As the line tension begins to decrease with increasing thickness (i.e., $\lim_{h\to\infty}\frac{\log(h)}{h}=0$), τ_{ex} also decreases for increasing h. This reduction in the driving force for dislocation glide is consistent with observations of cracking in thick films of GaAs-on-Si.[102] Finally, using mobility parameters for α-type TDs $v_0 = 1.9\times10^9\ \mu m/s$, $Q = 1.3\ eV$, and $m = 1.7$ from Yonenaga and Sumino, we calculate the corresponding glide thermal velocities for both cases using Alexander and Haasen's model (**Section 3.2.2**). As shown in **Figure 3.11e** although the excess stress continues to increase with decreasing temperature, the dislocation velocity begins to decrease noticeably below 500 °C, freezing out below 300 °C.

3.3.2 Quantum Dot Specific Effects

Quantum Dot Formation

Nevertheless, while these both the strain thickness product and Matthews-Blakeslee models are a useful guideline for the design of planar layers, quantum dots provide yet another layer of complication. Like dislocations, quantum dots form, in this system, due to lattice mismatch after some critical thickness, which I will refer to as h_{QD} to differentiate it from the Matthews-Blakeslee critical thickness for dislocation glide. Balancing the surface energies of the substrate, γ_s, epitaxial film surface, γ_f, and the thickness dependent substrate/film interfacial energy, $\gamma_i(h)$, allows us to predict whether the two materials will wet for a given film

thickness, h. **Figure 3.12** shows three cases of epitaxial deposition that occur under different circumstances. **Figure 3.12a**, Volmer-Weber growth, occurs when $\gamma_f + \gamma_i(h) > \gamma_s$ for $h > 0$. **Figure 3.12b**, Frank-van der Merwe growth, occurs when $\gamma_f + \gamma_i(h) < \gamma_s$ for $h > 0$. As shown, this does not lead to quantum dot formation. **Figure 3.12c**, Stranski-Krastanov growth, occurs when $\gamma_f + \gamma_i(h) \leq \gamma_s$ for $0 < h \leq h_{QD}$ but $\gamma_f + \gamma_i(h) > \gamma_s$ for $h > h_{QD}$. Stranski-Krastanov growth generally produces greater dot uniformity than Volmer-Weber growth. For additional details, see ref.[103]

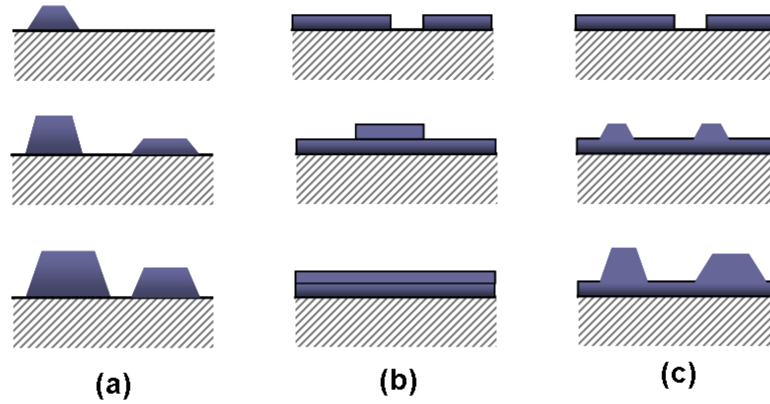

Figure 3.12 Schematics of various epitaxial growth modes that arise as a function of the relative interfacial and surface free energies between the film and substrate. **(a)** Volmer-Weber or island growth occurs when $\gamma_f + \gamma_i(h) > \gamma_s$ for $h > 0$. **(b)** Frank-van der Merwe or layer by layer growth occurs when $\gamma_f + \gamma_i(h) < \gamma_s$ for $h > 0$. **(c)** Stranski-Krastanov growth occurs when $\gamma_f + \gamma_i(h) \leq \gamma_s$ for $0 < h \leq h_{QD}$, leading to 2D growth, but $\gamma_f + \gamma_i(h) > \gamma_s$ for $h > h_{QD}$ leading to subsequent 3D growth. After ref.[104]

Quantum Dot Mechanical Hardening

As the self-assembled quantum dots in this system form due to lattice mismatch, it should not come as a surprise that they generate localized 3D strain fields in their vicinity, much like dislocations. Indeed, Beanland et. al demonstrate that they provide a mechanical hardening

effect akin to that of precipitates in metals. Assuming a hard sphere (R = 5 nm) InAs quantum dot at the bottom of an $In_xGa_{1-x}As$ quantum well (dot-in-well or DWELL) on a GaAs substrate, they calculate a significant increase in critical thickness for the case in which a dislocation bends over the quantum dots and glides above them in the quantum well, as shown in **Figure 3.13**.[55] They also report that QDs precipitate hardening like behavior seemingly suppress dislocation growth via both glide and climb during device operation.[43] Li reports a similar increase in critical thickness in quantum dot structures.[105]

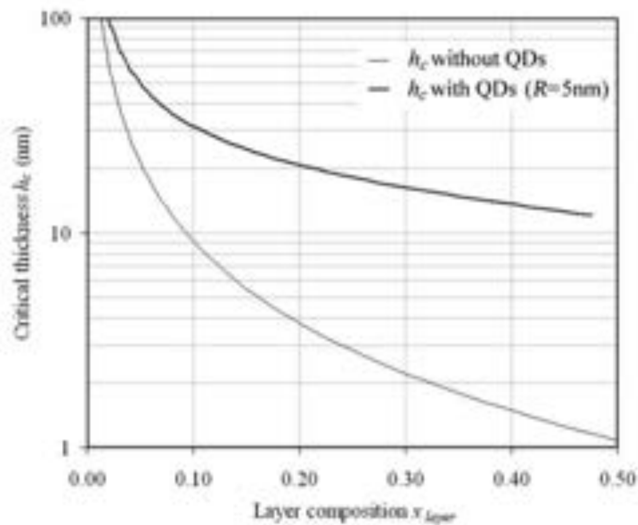

Figure 3.13 Calculated increase in critical thickness for InAs quantum dot in $In_xGa_{1-x}As$ quantum well structures as a function of quantum well composition assuming spherical, 5 nm radius InAs quantum dots at the bottom of the quantum well. Reprinted from R. Beanland, J. P. R. David, and A. M. Sanchez, "Quantum dots in strained layers—preventing relaxation through the precipitate hardening effect," *J. Appl. Phys.*, vol. 104, no. 12, p. 123502, Dec. 2008, doi: 10.1063/1.3028270, with the permission of AIP Publishing.

Misfit Dislocation Formation in QD Structures from Thermal Expansion Mismatch

As previously mentioned, GaAs has a larger coefficient of thermal expansion than Si ($\alpha_{GaAs} - \alpha_{Si} \approx 3 \times 10^{-6}$ K^{-1}), which my colleagues and I have demonstrated also is a key factor in misfit dislocation generation.[51] As shown in **Figure 3.14a**, after the termination of growth, but before cooldown begins (T = 580°C), we don't expect any misfit segments at the quantum dot layers: the 7 nm thick layers are far below critical thickness. However, during cooldown, tensile strain builds in GaAs layers as they approach 300 °C for the reasons discussed previously. The existing threading dislocations—nucleated to relieve the III-V/Si interfacial lattice mismatch—experience a glide force in any GaAs layers that are thicker than a few hundred nanometers (evaluated approximately using the strain-thickness product). The QD layer, however, prevents the threading dislocation segment it contains from gliding, referred to as pinning. As the free threading dislocation segment glides away, it lays down a misfit segment at the GaAs/QD layer interface (**Figure 3.14b**). The precipitate-like quantum dots and alloy hardening effects in $In_{0.15}Ga_{0.85}As$ QW mentioned previously provide the pinning shear. We do not expect the magnitude of these two effects to be the same, however, which is explored in greater depth in **Chapter 5**.

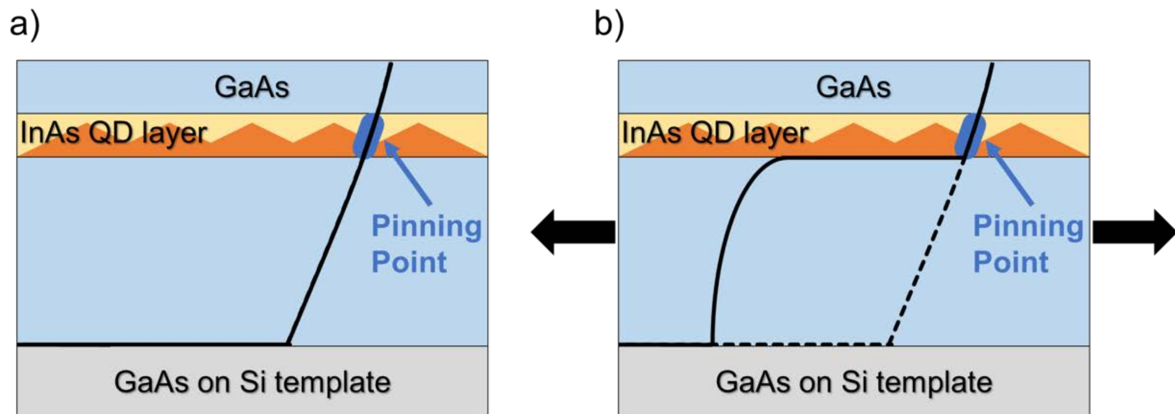

Figure 3.14 Schematic representation of dislocation structure in a single DWELL model structure during the post growth cool down process. **(a)** Immediately following growth (T = 580°C) the film is relaxed so there is no net glide force on the existing threading dislocations. While the DWELL itself is compressively strained, it is sub-critical thickness (i.e., no misfit dislocation segments should be present). **(b)** As the structure cools towards 300°C the film contracts more quickly than the substrate leading the existing threading dislocations to glide in the thick underlying GaAs layers. However, within the DWELL itself, the threading dislocation is pinned, leading to the formation of a misfit dislocation segment at the interface between the DWELL and thick underlying GaAs. The upper GaAs layer is assumed to be too thin for glide to occur at these small strains ($\varepsilon \approx 0.1\%$).

3.4 Summary

Dislocations in thin film semiconductors, in general, form and move due to an applied mechanical stress. They can do so conservatively via glide processes or non-conservatively via climb processes. Glide occurs significantly faster than climb, but glide rates are very sensitive to a variety of factors such as doping, dislocation structure, alloying, and the presence of other structural features, including quantum dots. In-plane misfit dislocations are generally thought to arise due to the initiation of glide in lattice mismatched layers exceeding critical thickness, but my colleagues and I propose an alternative formation mechanism for misfit dislocations in critical regions of the device, as the layers in question

should be below critical thickness. We propose instead that localized mechanical hardening in the quantum dot layers prevents glide there, forcing misfit dislocation segments to form as the underlying thick GaAs layers relax in response to an increasing thermal tensile stress.

Chapter 4:
Optoelectronic impacts of dislocations on quantum dots materials

4.1 Introduction

While the preceding Chapter offers insight into the presence of dislocations in III-V films grown on silicon substrates, these defects could have substantial negative impacts on both device performance and lifetime may not be immediately apparent. In semiconducting systems, the crystal symmetry and atomic bonding results in a bandgap—a set of forbidden energy levels with allowed energy levels on either side where the energy levels in the valence band (below the gap) are filled and those in the conduction band (above the gap) are empty. When the material is provided with sufficient energy, electrons in the valence band are excited across the bandgap into the conduction band. This results in an electron in the conduction band as well as an empty state, referred to as a hole, in the valence band. When conduction band electrons and valence band holes recombine the energy can released as light in radiative recombination processes (both spontaneous emission and stimulated emission in lasers). However, electrons and holes can also recombine through two non-radiative pathways: Auger recombination and defect assisted Shockley-Read-Hall (SRH) recombination. This Chapter first provides the reader with some context on these non-radiative processes and the factors that influence them. Next, I detail an experiment my colleagues and I performed to characterize defect assisted non-radiative recombination processes in quantum dot materials.

Finally, I conclude by discussing the effects of non-radiative recombination on the structure of the dislocations themselves, discussing both recombination enhanced dislocation glide and recombination enhanced dislocation climb process.

Note that I performed the InAs quantum cathodoluminescence work in this Chapter at EAG Laboratories-Eurofins Materials Science in Raleigh, NC under the supervision and with the assistance of Dr. Michael E. Salmon during a summer internship. The InAs QD CL work in **Chapter 5** was also performed at EAG in Raleigh, however, as I had returned to UCSB at the point, those measurements were performed by Dr. Salmon. Note also that the single quantum dot layer sample analyzed in **Section 4.3** was grown by Dr. Justin C. Norman who at the time was with the Bowers group and has subsequently joins Quintessent, Inc. Its threading dislocation density reducing buffer (for more details on TDD filtering, see **Chapter 5**) was grown by Dr. Daehwan Jung who at the time was with the Bowers group and has subsequently joined the Korea Institute of Science and Technology. Note also that the ECCI measurements in the same Section were performed by Mr. Eamonn T. Hughes who is a current student in the Bowers and Mukherjee groups.

4.2 Carrier Recombination in Semiconductors

As we are not considering full laser structures in this Chapter, we can model the change in number of charge carriers, N, over time ($\frac{dN}{dt}$) with the equation:

$$\frac{dN}{dt} = -AN - BN^2 - CN^3$$

where BN^2 represents the radiative recombination rate due to spontaneous emission, AN represents SRH recombination rate, and CN^3 represents the Auger recombination rate. A, B, and C are the rate constants for SRH recombination, radiative recombination, and Auger recombination, respectively.

4.2.1 Auger Recombination

Unlike radiative recombination which requires the simultaneous participation of two charge carriers, an electron and a hole, Auger processes require three. In these processes, an electron and a hole recombine across the bandgap, however, the resulting energy is passed to the third charge carrier, which can be either an electron or a hole, exciting it away from the band edge. The energy is released as heat when the high-energy carrier subsequently decays back the band edge. Although microstructure, including quantum dots, can impact Auger recombination rates,[106] we generally treat them as materials properties.

4.2.2 Shockley-Read-Hall Recombination

SRH recombination rates, in contrast, are heavily dependent on microstructure. Because crystal defects locally break the crystal symmetry, they give rise to their own set of available energy states. Often this leads to available energy states within the bandgap referred to as trap states. These trap states provide an alternative carrier recombination pathway that results in the generation of heat rather than light. Unlike radiative recombination which requires the simultaneous participation of the electron-hole pair, non-radiative recombination at defects occurs sequentially because an empty trap state cannot capture any additional holes, nor can a filled trap state capture any additional electrons. Instead, the carriers effectively swap places.

As a result, the non-radiative recombination rate arising from defects is necessarily a function of the concentration of both electrons and holes and their respective capture times. The capture times in turn are function of the total number of trap states available as well as the efficiency of individual trap states. We describe the non-radiative recombination rate due to defects using the following equation:

$$R_{defect} = \frac{NP - N_i^2}{(N^* + N)\tau_h + (P^* + P)\tau_e}$$

where R_{defect} is the defect recombination rate, N is the electron density, P is the hole density, N_i is the intrinsic carrier concentration, N^* and P^* are the electron and hole densities that would exist if the fermi level were aligned to the energy level of the trap state. τ_e and τ_h and represent the time to capture an electron from the conduction band, assuming all trap states are empty and the time to capture a hole from the valence band assuming all trap states are full, respectively. Under device operating conditions ($P = N \gg N^*, P^*, N_i$) this expression simplifies to $R_{defect} = \left(\frac{1}{\tau_h + \tau_e}\right) N$. As the rate depends on sum of the capture times, a trap located near the center of the bandgap which will capture both carriers similarly efficiently maximizes its recombination rate.

Mitigating Shockley-Read-Hall Recombination

However, while Shockley-Read-Hall recombination is problematic, it is substantially easier to mitigate than Auger recombination. As each defect has a finite number of trap states and each SRH event takes a finite amount of time. Thus, reducing defect densities, reduces SRH losses. Likewise, limiting the number of carriers that can reach the trap states can also

minimize SRH losses. GaN-based devices, for example, often have relatively high dislocation densities. But, as GaN based alloys have short minority carrier lengths, dislocations effectively have access to only a tiny fraction of the total carriers in the material. Under such a scenario, even with very high dislocation densities, cathodoluminescence maps, like the one shown in **Figure 4.1**, show clear bright areas.[107] The many small dark spots, on the order of 100 nm, are attributed to threading dislocations; dark spot sizes (a convolution of minority carrier length and incident beam size) are consistently reported in GaN to be on the order of 10s to 100s of nm. [107]–[109] While it is clear from these images that threading dislocations are very non-radiative, the short diffusion length and thus relatively small number of trap-accessible carriers means that high electron mobility transistors with threading and light emitting diodes with dislocation densities as high as 10^8-10^9 cm^{-2} demonstrate reasonably reliable operation.[110], [111] Unfortunately, in arsenide-based QW systems, rather than a few 10s of nm, this length is on the order of a few microns, meaning that each individual dislocation reduces the carrier concentration in several square microns of material.[112]–[115]

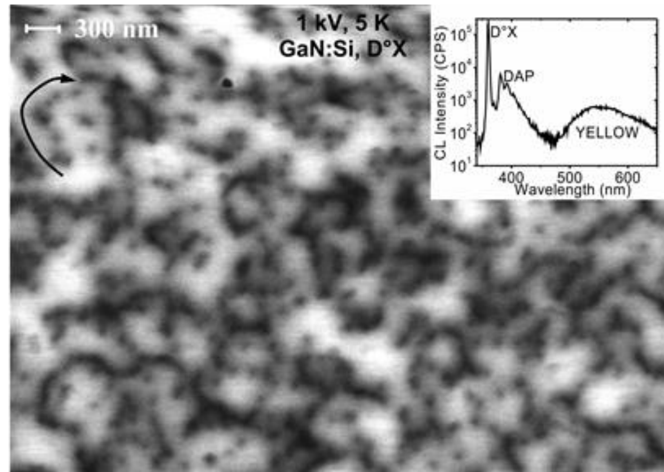

Figure 4.1 Monochromatic CL micrograph (λ=360 nm) acquired at 5 K using 1 kV excitation voltage of silicon doped GaN. Inset shows the corresponding 5 K CL spectra. Reprinted from N. Pauc, M. R. Phillips, V. Aimez, and D. Drouin, "Carrier recombination near threading dislocations in GaN epilayers by low voltage cathodoluminescence," *Appl. Phys. Lett.*, vol. 89, no. 16, p. 161905, Oct. 2006, doi: 10.1063/1.2357881, with the permission of AIP Publishing. After ref. [107]

4.3 Shockley-Read-Hall Recombination Behaviors in Quantum Dots

4.3.1 Initial Expectations

However, although the presence of both threading and misfit dislocations within the active regions of experimental quantum dot lasers on silicon have been observed previously,[46], [49] these defects' optoelectronic impacts in quantum dot systems were not well characterized prior to this work. As noted previously, quantum dot based devices demonstrate substantial improvements in laser performance and reliability over quantum well based devices.[40] Researchers frequently attributed this behavior to the quantum dots' atom-like density of

states, arguing it should prevent carriers from reaching the trap states generated by dislocations.[42], [45], [46], [112] **Figure 4.2** presents a comparison of carrier diffusion in quantum wells and the assumed diffusion in quantum dots. **Figure 4.2a** and **Figure 4.2b** show a structural schematic and band diagram of a quantum well containing a threading dislocation. Carriers sufficiently close to the dislocation, within the minority carrier diffusion length, diffuse freely to its trap states and recombine non-radiatively via Shockley-Read-Hall recombination. Conversely, as shown in **Figure 4.2c** and **Figure 4.2d**, in quantum dot based systems, researchers expected diffusion lengths to be on the order of a few tens of nm, approximately the spacing between the quantum dots. The quantum dots were assumed to be ideal, meaning that once carriers were captured by a quantum dot they would be strongly confined and thus unable to diffuse to available energy states arising from nearby quantum dots or defects.[116] In this case, only those carriers within a single dot length would be able to reach the dislocation's trap states, as free carriers further away would be captured by non-defective quantum dots. This should result in performance similar to GaN based systems, and indeed, quantum dot lasers on silicon have been shown to operate for thousands of hours with threading dislocation densities on the order of 10^8 cm^{-2},[46] as compared to but their lifetimes have been shown to depend strongly on threading dislocation density.[40]

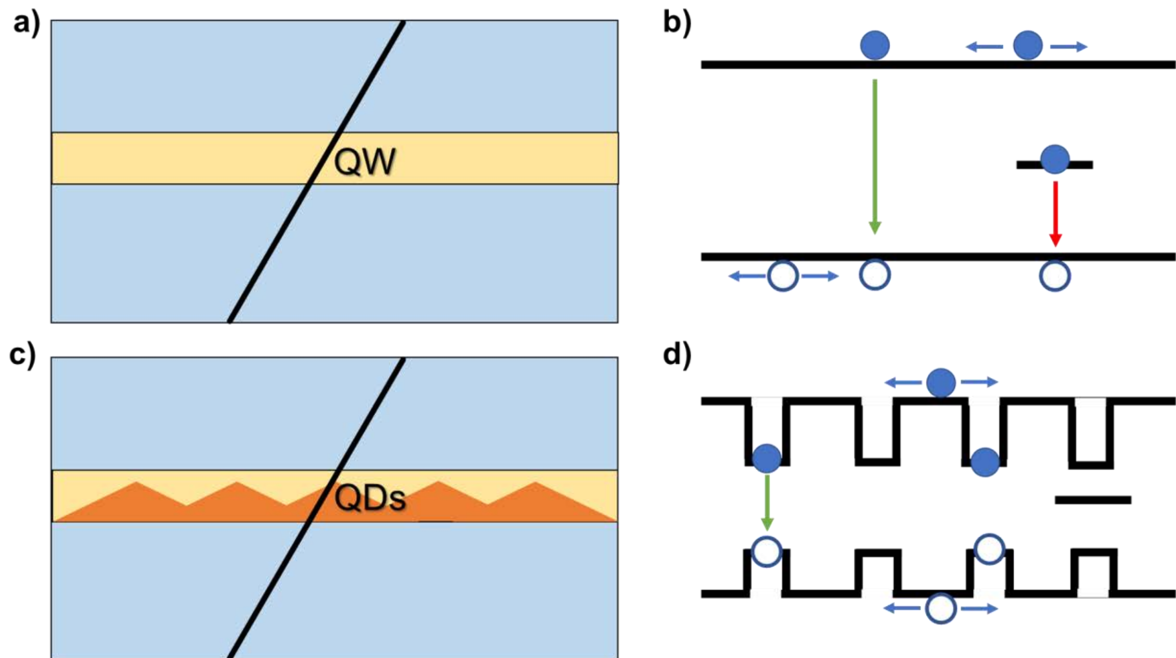

Figure 4.2 **(a)** Schematic and **(b)** band diagram of a threading dislocation crossing a QW. Carriers can easily laterally diffuse to the mid-gap trap state generated by the dislocation, allowing them to recombine non-radiatively (red arrow) as opposed to radiatively (green arrow). **(c)** Schematic and **(d)** band diagram of a threading dislocation crossing a QD layer. Only those carriers sufficiently close to the dislocation can reach the trap state; carriers within non-dislocated dots are assumed to stay there and recombine radiatively.

4.3.2 Model Structure

To better understand dislocations' optoelectronic impacts in quantum dot material, we investigate these defects using two SEM based techniques: ECCI and CL. As these techniques require that the area of interest be accessible via a low excitation voltage, we grew a QD model structure via molecular beam epitaxy, as shown in **Figure 4.3**. It consists of single QD layer 100 nm from the surface on a GaAs buffer containing defect filter layers on Si as shown both schematically and via bright field STEM. The inset shows a higher

magnification bright field image of the dot layer. The stark contrast between the DWELL and the surrounding GaAs matrix arises from the change in composition and the high degree of strain in the dot layer. Note that I acquired the STEM images in this Chapter, on a ThermoFisher Talos G2 200× TEM/STEM using a 160 mm camera length and a Thermo Scientific BFSTEM circular detector.

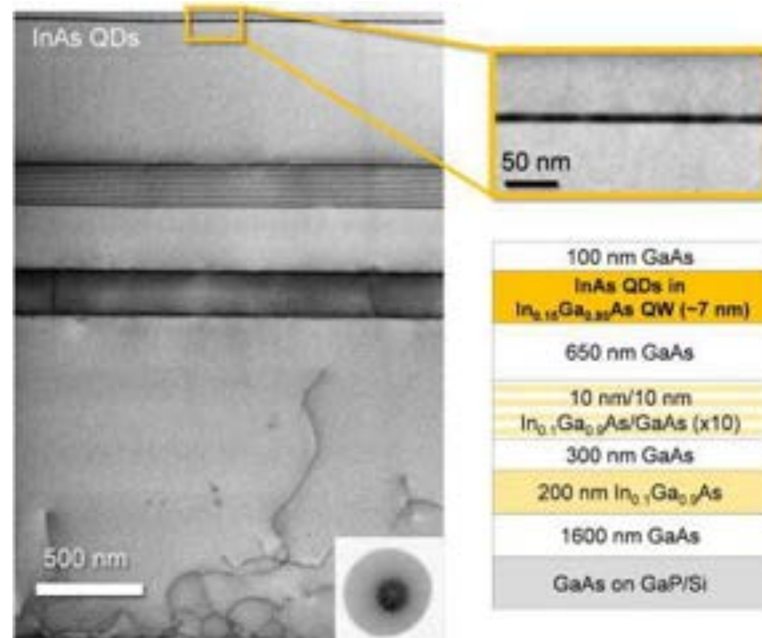

Figure 4.3 Cross-sectional [110] zone axis bright field scanning transmission electron micrography (BFSTEM) image and schematic showing the model structure. Inset shows a higher magnification BFSTEM image of the quantum dot layer. Reprinted from J. Selvidge et al., "Non-radiative recombination at dislocations in InAs quantum dots grown on silicon," *Appl. Phys. Lett.*, vol. 115, no. 13, p. 131102, Sep. 2019, doi: 10.1063/1.5113517, with the permission of AIP Publishing.

4.3.3 Growth Details

The details of the buffer design are discussed in detail in by Jung *et al.* in ref. [39], resulting in a threading dislocation density in the sample of 7×10^6 cm^{-2}.The InAs QDs were grown in an $In_{0.15}Ga_{0.85}As$ QW at 500 °C, with 2 nm of $In_{0.15}Ga_{0.85}As$ below the dots and a 5 nm cap above, and 2.5 monolayers of InAs grown for the dots themselves at 0.03 nm/s. We grew the $In_{0.15}Ga_{0.85}As$ layer below the dots with a V/III ratio of 10 and the dots and capping layers at a V/III ratio of 35. After growth of a 2.5 nm GaAs cap, we annealed the dots-in-a-well structure at 580 °C for 5 min, followed by growing the top 97.5 nm GaAs layer at 580 °C.

4.3.4 Baseline Optoelectronic Measurements

We performed some initial room temperature (RT) characterization of our structure using photoluminescence (PL) spectroscopy. This provided a baseline spectrum for comparison with the RT CL measurements. The PL spectrum allowed us to identify distinct peaks, as shown in **Figure 4.4**. In order of increasing energy, the peaks correspond to the QD ground state (GS), first excited state (FES), and second excited state (SES) emissions, respectively. The broad peak near 1000 nm we attribute to the wetting layer (WL) emission. From the PL spectrum, we measured energy separations between the bound states to be 58 meV from the GS to the FES and 48 meV from the FES to the SES—shown schematically. The reader should note that this diagram is a simplification by necessity; the higher order emission peaks are particularly sensitive the strain state and shape of the dots, so assigning them specific electron and hole states is difficult.[117]–[119] There is also some evidence that the SES peak may involve transitions with hybrid QD-2D-continuum states,[120] in agreement

with the results discussed in this Chapter. Note that we also see a PL emission peak at approximately 1080 nm in Fig. 4.4; we attribute to an artifact from the optics of the measurement setup.

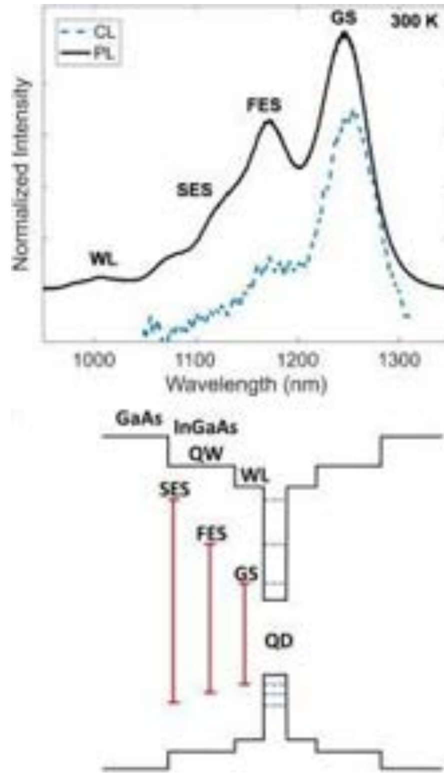

Figure 4.4 Room-temperature photoluminescence (PL) and cathodoluminescence (CL) spectra from the structure showing emission from the quantum dot and wetting layers (shown offset vertically); the labeled peaks correspond to the ground state (GS), first excited state (FES), second excited state (SES), and wetting layer (WL). These transitions are also represented schematically. Reprinted from J. Selvidge et al., "Non-radiative recombination at dislocations in InAs quantum dots grown on silicon," *Appl. Phys. Lett*., vol. 115, no. 13, p. 131102, Sep. 2019, doi: 10.1063/1.5113517, with the permission of AIP Publishing.

The area-averaged CL spectrum also presented in **Figure 4.4** closely matches the PL spectrum. I collected this spectrum, and all subsequent CL data in this Chapter, using an Attolight Rosa System with an Andor iDus InGaAs detector. In all cases, emission intensity

values were collected over a 262 nm wavelength range (0.5 nm step-size) at each pixel. The spectrum here and the luminescence maps in **Figure 4.5b** and **Figure 4.7a** were generated using a 10 kV excitation voltage and 5 nA beam current. Note that for this CL spectrum, and for all subsequent CL measurements, RT correspond to the system's ambient temperature with neither heating nor cooling: 281 K.

4.3.5 Linking Dark Regions to Dislocations

After marking the sample with fiducials using a focused ion dual beam system, we found dislocations in these marked areas using ECCI (**Figure 4.5a**). ECCI data was collecting using a 30 kV electron beam, a probe current of 3.4 nA. The (400) / (220) channeling condition should render all the expected dislocations visible,[39] however, only if those dislocations are sufficiently near to the sample surface—and thus the shallow QD layer. **Figure 4.5b** shows a panchromatic CL map imaged at RT. The 10 kV excitation voltage and 5 nA probe current results in a ~400 nm diameter carrier generation volume. The relatively low densities of both misfit dislocations and threading dislocations allow us to correlate individual dark lines and spots to specific misfit and threading dislocations, respectively. We note that the presences of QD-adjacent misfit dislocations in our model structures was unexpected. Their formation mechanism is outlined briefly in **Chapter 3**, and their mitigation strategy is outlined in **Chapter 5**.

I additionally performed PV- BFSTEM (using a (220) two beam condition) of this site after the conclusion of ECCI and CL studies (**Figure 4.5c**). Yellow arrows mark a few selected misfit dislocations and their corresponding optical signatures in all three images.

Further examination of **Figure 4.5c** shows that some misfit dislocations are present in the PV-STEM foil but do not appear in the ECCI or CL. The location of one such dislocation has been marked with a red arrow in all three images.

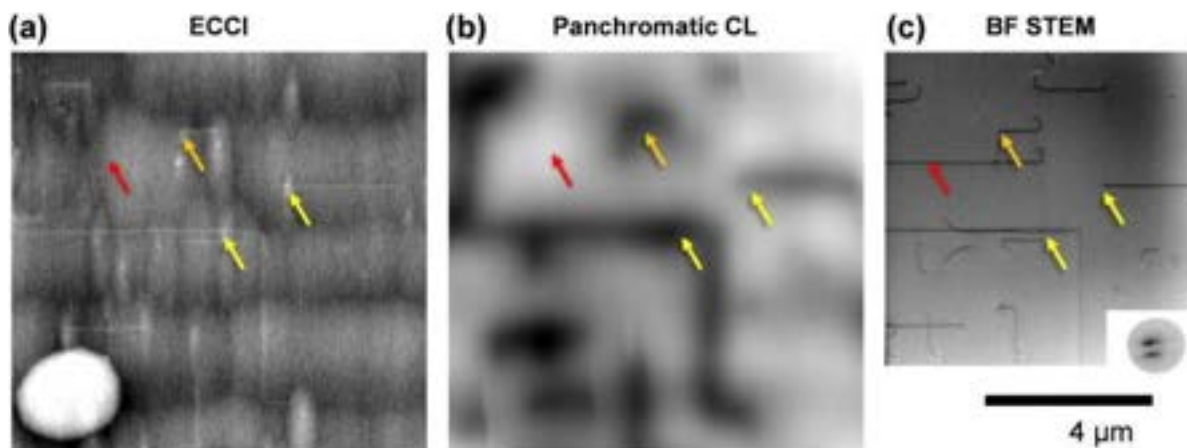

Figure 4.5 Corresponding **(a)** electron channeling contrast imaging (ECCI) map [channeling condition = (400)/(220)], **(b)** room temperature panchromatic cathodoluminescence (CL) map (10 kV excitation voltage), and **(c)** plan-view bright field scanning transmission electron micrography image for a single region (**g**=**220**). Yellow arrows denote misfit dislocations that appear in all three images, while the red misfit dislocation appears only in the STEM image. Comparing the threading dislocation segments for the dislocation marked with the red arrow and the dislocation marked with the orange arrow allows us to identify that they are different depths from the sample surface. Reprinted from J. Selvidge et al., "Non-radiative recombination at dislocations in InAs quantum dots grown on silicon," *Appl. Phys. Lett*., vol. 115, no. 13, p. 131102, Sep. 2019, doi: 10.1063/1.5113517, with the permission of AIP Publishing.

To understand why certain misfit dislocations might be visible in STEM but invisible via SEM based techniques, we measure their associated threading dislocation segments' lengths. Threading dislocation segments in this system are lie on {111} planes. Therefore, the misfit dislocation marked with the red arrow lies 400–500 nm below the surface—too far from the QD layer to impact its luminescence and too deep to be detected via ECCI. In

contrast, by examining the threading segment associated with the dislocation marked with the orange arrow, we can deduce the misfit segments lies 100–150 nm from the surface. Thus, we would expect this misfit dislocation to be visible in ECCI and to be sufficiently close to the QD layer to generate a dark line in the CL emission.

While a full analysis of the dark spot behaviors arising from threading dislocations is important, threading dislocation clustering makes it more difficult to analyze the behavior of a single thread. On the other hand, as the long segment of misfit dislocations have larger impacts on the active layer and are generally isolated, they have been used for the subsequent analysis. It is also worth noting that direct comparison to CL studies of dislocations in the literature is difficult. Dark line characteristics are governed not only by the recombination strength of the defect and the carrier capture lengths, but also by the sample structure and the excitation conditions.

4.3.6 Estimating Dark Line Width

Figure 4.6a shows a RT filtered CL GS emission intensity map with dark line defects. The 5 kV excitation voltage and 2 nA beam current yield a carrier generation volume diameter of approximately 100 nm. For this and all subsequent wavelength filtered CL maps, we selected a wavelength range consisting of the full peak width at half-maximum intensity for the ground state (GS) first excited state (FES) and second excited state (SES), averaging the intensity at each pixel from that subset. **Figure 4.6b** shows the intensity profiles across the marked dark line regions in **Figure 4.6a**. We measure ≈40% peak relative intensity loss due to misfit dislocations. The fine-probe CL-measured dark-line half width of 0.5 μm provides

a very rough estimate of the carrier capture length[121] for the high injection regime in this system at RT. This length is much larger than the mean QD spacing (20–40 nm). Instead it is in line with carrier diffusion lengths for QD samples reported on native substrates.[112], [122] Notably, it is also only two to four times shorter than the carrier diffusion lengths reported for QW samples.[114] This implies that carriers are not nearly as confined to the quantum dots as initially expected. Instead thermally excited carriers[123] can travel through the two-dimensional QW-like WL to dislocations. Thus, the WL, rather than the quantum dots, controls the dislocations' area of influence.

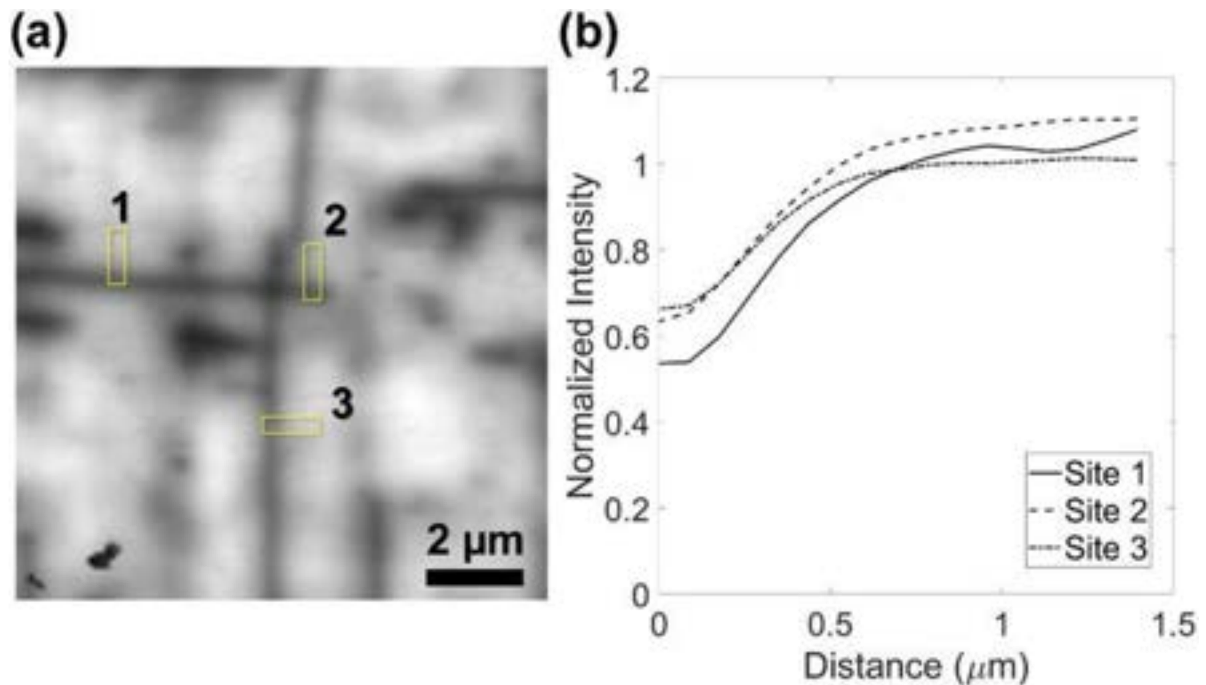

Figure 4.6 (a) Room temperature filter ground state emission cathodoluminescence map (5 kV excitation voltage) showing misfit and **(b)** half side normalized intensity (averaging across a 1.18 μm width) as a function of distance from the dislocation's center for the sites indicated in (a). Reprinted from J. Selvidge et al., "Non-radiative recombination at dislocations in InAs quantum dots grown on silicon," *Appl. Phys. Lett.*, vol. 115, no. 13, p. 131102, Sep. 2019, doi: 10.1063/1.5113517, with the permission of AIP Publishing.

4.3.7 Temperature and State Dependent Dark Line Behaviors in QD Materials

Measuring the peak CL emission loss at misfit dislocations and their dark line width as a function of temperature provides insight into the mechanism by which dislocations capture carriers from QDs. **Figure 4.7a** shows CL maps from a typical region containing misfit dislocations across a temperature range of 10 K–300 K. I collected and processed each map using the 10 kV imaging conditions and filtering described previously. **Figure 4.7b** shows the intensity profile across the indicated misfit dislocation in **Figure 4.7a** for each temperature and emission state. As shown in **Figure 4.7a**, the dark line width remains constant with temperature, but the peak intensity loss is strongly dependent on both the temperature and the state. The SES emission loss appears to be nearly temperature invariant, whereas the behaviors in both the GS and the FES depend strongly on temperature.

To assess this behavior more robustly, **Figure 4.7c** present mean peak intensity loss and standard deviation from five misfit dislocations. At 300 K, there is no clear difference in the peak intensity loss at misfit dislocations between the GS, FES, and SES: all values fall within the error. This, combined with the temperature and state independence of the dark line width, suggests a common pathway for carrier capture at dislocations across all states. However, lowering the temperature below 200 K dramatically reduces the emission loss from first the GS and then the FES. Below 100 K, the GS and FES peak intensity loss at the dislocation drops to ≈10% and ≈15%, respectively. In contrast, the maximum SES emission

loss at the dislocation remains ≈40%–50% across the entire temperature range, in agreement with the temperature invariance noted previously in **Figure 4.7b**.

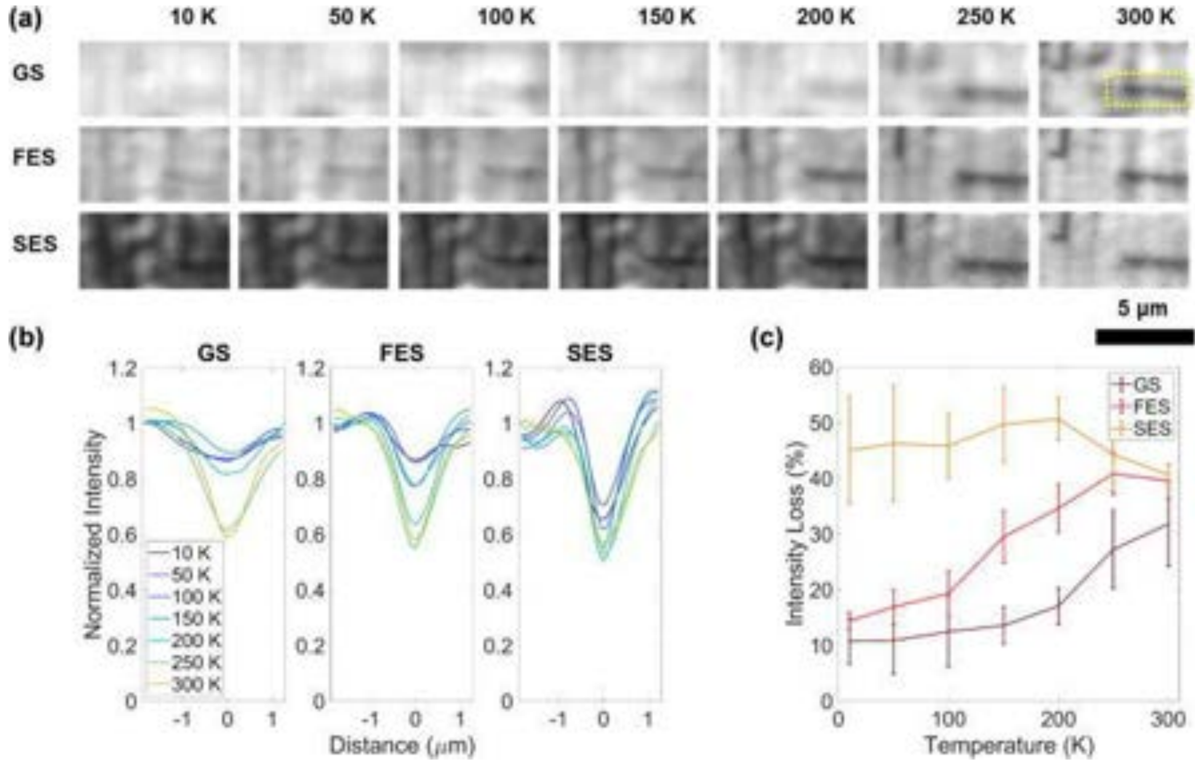

Figure 4.7 (a) Filtered 10 kV cathodoluminescence maps of the ground state (GS), first excited state (FES), and second excited state (SES) emissions across the temperature range 10 K–300 K. **(b)** Normalized GS, FES, and SES CL intensities as a function of distance across the dislocation indicated in (a) over the same temperature range. **(c)** Mean peak intensity loss as a function of temperature for the GS, FES, and SES emission; the error bars indicate the standard deviation from the five dislocation sample. Reprinted from J. Selvidge et al., "Non-radiative recombination at dislocations in InAs quantum dots grown on silicon," *Appl. Phys. Lett*., vol. 115, no. 13, p. 131102, Sep. 2019, doi: 10.1063/1.5113517, with the permission of AIP Publishing.

Note that I performed these experiments in order of increasing temperature from 10 K to 300 K. In some cases, as the temperature crossed 250 K, a change in the dislocation structure accompanies the increase in GS nonradiative recombination. The change in the dislocation

segment on the top left of each image in **Figure 4.7a** provides direct evidence of recombination enhanced dislocation glide, a known failure mechanism in QD lasers on Si.[46]

While the wide dark line widths at room temperature suggest that the WL controls dislocations' impacts in this system, the strong temperature and state dependences of the dark line intensity loss suggests that the situation is more complex. The quantum dots' temperature dependent carrier occupation behavior appears to control the reduction in emission. At 300 K, all the QD states are in thermal equilibrium with the WL and so show similar emission loss profiles. Thus, non-radiative recombination at the dislocation will proportionally reduce carriers in all three QD states. However, at lower temperatures the GS and FES occupation probabilities becomes increasingly random.[116], [124], [125] Each QD accepts any available carriers until all its states are filled. The low temperature prevents the carriers from thermalizing to the WL, preventing them from traveling to adjacent dots or nearby dislocation trap states, consistent with a reduction in emission loss. Temperature-dependent PL measurements on InAs QDs on Si also show a drop in GS luminescence starting at 200 K due to increasing carrier thermalization.[126] As the SES shows no such change, we expect that the WL has a relatively wide emission band. Its trailing lower energy states may even hybridize with SES dot states, as the SES carriers appear to have an escape pathway at all temperatures. This difference is shown schematically in **Figure 4.8**.

We additionally considered that the incident beam could generate high kinetic energy carriers that could recombine directly at dislocations via diffusion in the GaAs or QW layers prior to capture by the dots.[127] But, we expect that direct diffusion of carriers to

dislocations would be temperature invariant. The strong temperature and state dependences therefore imply that the QDs capture the electron beam-generated carriers rapidly; these carriers simply subsequently thermalize and diffuse to the dislocations at sufficiently high temperatures. While in theory the carriers could also travel to adjacent dots, we expect that at these high carrier injection levels the neighboring dots should also be occupied, making re-trapping unlikely.

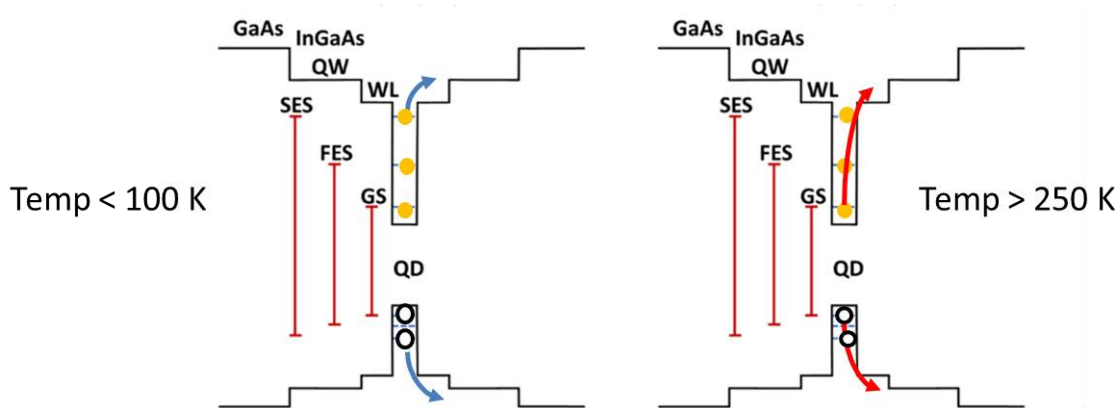

Figure 4.8 Schematic comparing carrier escape from quantum dot states at low temperatures (T<100 K) and near room temperature (T >250 K). At low temperatures, only carriers in the second excited state can thermalize to the wetting layer, but near room temperature, all the quantum dot's energy states are in thermal equilibrium with the wetting layer.

4.3.8 Source of Dislocation Tolerance in QD Model Structures

Our results suggest that carrier confinement in InAs QDs plays a secondary role in improving device performance. And at industrially relevant device temperatures, near 80°C, this benefit is virtually eliminated by easy carrier escape. However, the basic premise for defect tolerance due to carrier confinement remains interesting: as is, the GS and the WL thermally equilibrate

at 300 K. Slightly increasing this energy separation between the states could push this equilibrium point to higher temperatures but doing so is likely non-trivial. That said, our current QD designs show substantially improved defect tolerance over QWs. We expect that this in part because carriers simply cannot travel as far to reach dislocation trap states in QD material—rendering these defects less harmful. The more limited diffusion in the WL may be the result of increased carrier scattering, as we expect the WL to be far less uniform than a standard QW.

4.4 Non-radiative Recombination's effects on Dislocations

To this point, I have been considering the impacts of defects on carrier recombination but have only alluded to the impacts of carrier recombination on defects briefly, however, the effects in that direction are equally important. Both glide and climb can occur because of carrier recombination, and the recombination enhanced dislocation motion (REDM) processes constitute an important failure mechanism in III-V on Si lasers.

4.4.1 Recombination Enhanced Dislocation Glide (REDG)

GaAs experiences what is referred to as a 'negative photo-plastic effect' meaning the material softens when illuminated with light whose energy is near the bandgap as a result of increased dislocation mobility.[128], [129] Thus, while to this point I have mostly treated the system's optoelectronic and mechanical properties as independent entities, that is a clear over-simplification. Likewise, electron beam illumination in an SEM,[51], [52], [56], [97], [130],

[131] TEM,[132] and current injection[133]–[135] (i.e. device operation) have all been shown to facilitate dislocation glide at ambient temperatures. We understand this phenomenologically to be due to direct coupling of the energy released via SRH recombination and bonding at the dislocation core which leads to a momentary reduction in the Peierls barrier.[131] As an example, **Figure 4.9** presents the initial and final frames of an electron-channeling contrast imaging (ECCI) time-lapse sequence in a single quantum dot model structure (for acquisition details, see **Chapter 5**). Newly grown misfit dislocation segments are visible both in the $[110]$ and $[\bar{1}10]$ directions, an example of which has been marked with the orange arrow.

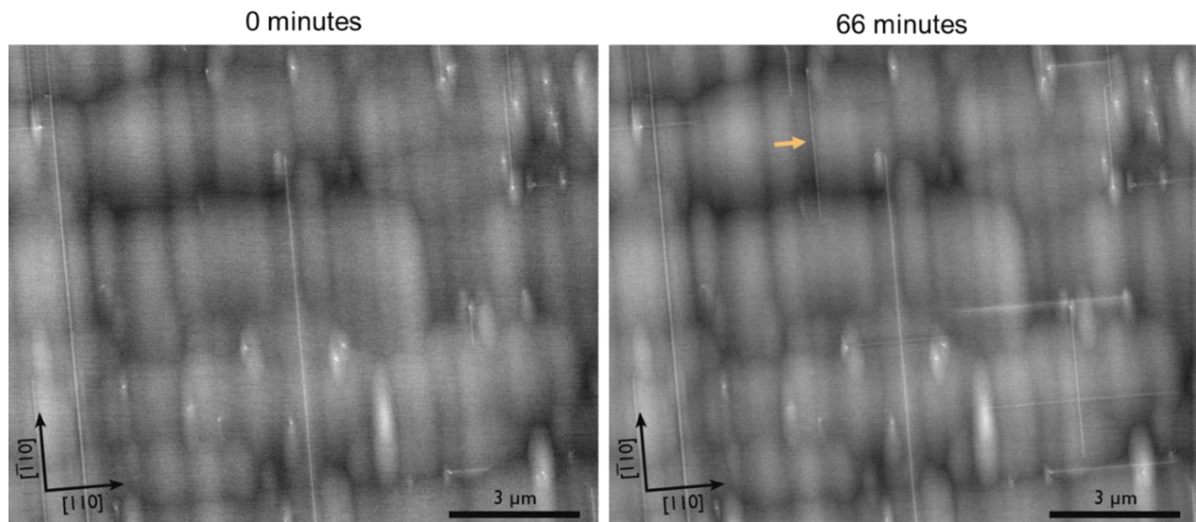

Figure 4.9 ECCI images of a single DWELL model structure before imaging (left) and after 66 minutes of continuous image acquisition (right). The orange arrow indicates an example of a misfit dislocation segment that formed through REDG during imaging.

4.4.2 Recombination Enhanced Dislocation Climb

Carrier recombination also substantially increases the rate of dislocation climb and often results in the growth of extensive, complex, <100> oriented networks[133], [136]–[138] an example of which is presented in **Figure 4.10**.[139] The stereo image pair (a technique akin to tomography) using $\boldsymbol{g} = \bar{\mathbf{2}}\mathbf{20}$ as the tilt axis (tilt angle demonstrating the three-dimensional nature of the dislocation networks marked “A” and “B.”[139] The three-dimensional nature of these structures, and the presence of dislocation loops like the one marked “D” in **Figure 4.10**, suggest that climb occurs in these systems via the attachment of prismatic dislocation loops to the dislocation line. With that said, our understanding of the exact mechanism is somewhat unrefined. We know that REDC occurs generally occurs more readily in wider bandgap zinc-blende semiconductors, however, InP is far less prone than GaAs despite their relatively similar bandgap energies. Another important factor appears to be whether the defects generate deep level trap states within the system, which, occurs in GaAs based compounds (and InGaAsP lattice matched to GaAs) but does not occur in InP (and InGaAsP latticed matched to InP).

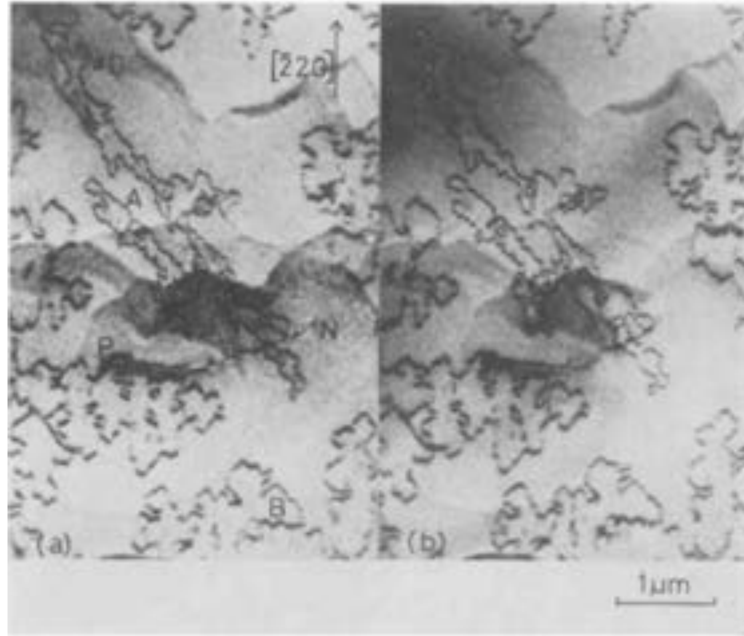

Figure 4.10 Stereo image pair (tilt axis: g=220, tilt angle: 25°), illustrating the three dimensional nature of the dislocation networks labeled A and B. The beam directions are close to **(a)** $[\bar{1}\bar{1}6]$ and **(b)** $[116]$. The threading dislocation PN intersects the p AlGaAs layer surface at point P and the n AlGaAs layer at point N. After ref.[139]

We can also understand the increased rate in part due to recombination enhanced defect reactions, which dramatically increase point defect diffusion rates. But it is not fully clear why the necessary point defects would existence in the first place. Two models, referred to as the intrinsic model and the extrinsic have been proposed, each with several variants. The first, initially proposed by O'Hara[59], and later modified by Tan et al. to include a more clear driving force,[140] argues that the non-radiative recombination at the dislocation provides the energy to generate the necessary point defects. Our preliminary results reported in ref.[50] support this conclusion. Nevertheless, the extrinsic model, which states that the necessary point defects already exist in the system[141] or may be due to a free surface[142], may yet still have merit.

We find that the climbed structures that form are quite different in our quantum dot based devices than traditional quantum well structures; we do not see the growth dislocation networks due to threading dislocation climb.[46], [49], [50] Because we expect climb in this system to proceed via the emission of vacancies into the bulk,[50] we expect that the compressively strained quantum dot layers may resist the expansion of the extra half plane of atoms, as observed by Wang, Hopgood and Ng.[136] We have also confirmed, using tomography, that recombination enhanced dislocation climb on misfit dislocations results in two-dimensional, rather than three-dimensional growth.[50]

To understand the two-dimensional climb on the misfit dislocations, consider, for example, the position of the misfit dislocation segment adjacent to the quantum dot layer in **Figure 4.11a.** At the quantum dot layers, the sign of strain switches from tensile in the underlying GaAs layers to compressive in the quantum dot layer itself. The misfit dislocation should lie in a position where it experiences no net shear in the in the z-direction. Consider the addition of a prismatic loop with the same burgers vector as the dislocation itself, **Figure 4.11a**. The attachment of the prismatic loop to the dislocation causes the portions of the misfit dislocation to lie outside the plane of neutral strain, such that it experiences a restoring glide force, along a cylindrical glide surface,[143] as shown in **Figure 4.11b**. REDG facilitates the glide portion of the process.

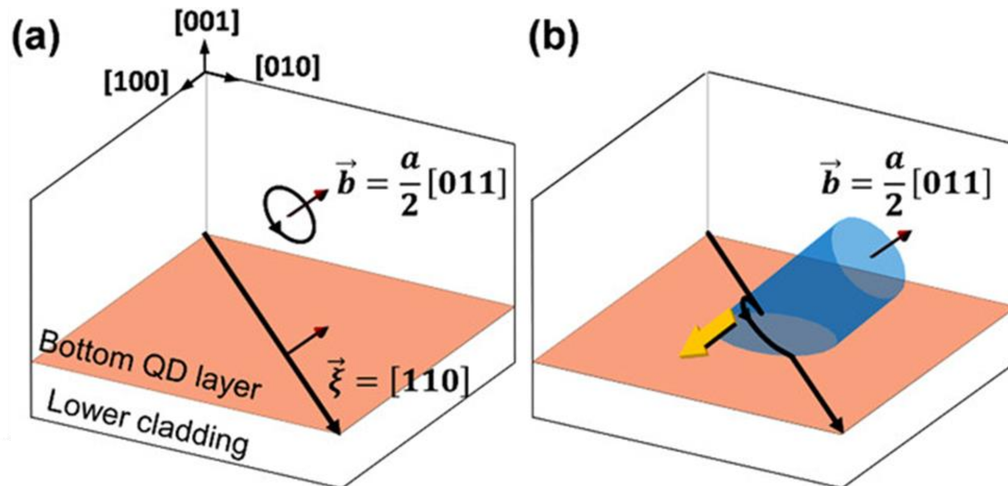

Figure 4.11 (a) A misfit dislocation (ξ = $\mathbf{1\bar{1}0}$ and $\mathbf{b} = \frac{a}{2}[\mathbf{011}]$) at lying at the neutral strain interface between the bottom QD layer and the lower cladding. For simplicity, we assume the dislocation relieves compressive strain is undergoing negative climb. Therefore, we represent the required point defects as an interstitial prismatic dislocation loop. **(b)** Attachment of the loop results in a curved protrusion segment out of the neutral strain plane. The protrusion experiences a restoring glide force (yellow arrow) along a cylindrical glide surface (blue) due to compressive stress in the QD layer and returns to the neutral strain plane. Reprinted from K. Mukherjee et al., "Recombination-enhanced dislocation climb in InAs quantum dot lasers on silicon," J. Appl. Phys., vol. 128, no. 2, p. 025703, Jul. 2020, doi: 10.1063/1.5143606, with the permission of AIP Publishing.

4.5 Summary

Although quantum dot based structures were expected to be more dislocation tolerant than quantum well based structures due to carrier confinement within the dots, my colleagues and I found that, at room temperature, the affected area associated with dislocations is only two to four times smaller in QD systems as compared to similar QW systems. However, we also identify that this behavior is highly dependent on both state and temperature, suggesting that additional optimization could provide improved dislocation tolerance due to increased carrier

confinement within the dots. We suggest instead the observed dislocation tolerance at and above room temperature arises due to scattering within the wetting layer and due to the QDs' mechanical properties which resist the growth of extensive dislocation climb networks.

Chapter 5:

Dislocation Filtering Strategies

5.1 Introduction

As dislocations have proven to be quite problematic, even in quantum dot systems, decades of work have gone into identifying strategies to mitigate their impacts. Generally, these efforts have focused on pathways to reduce the absolute number of threading dislocations within device active regions. Thus, this Chapter provides a review of some common threading dislocation reduction strategies, which are frequently pursued in tandem. However, as discussed in **Chapters 3&4**, my colleagues and I additionally identified a previously unaddressed misfit dislocations lying within the lasers' active regions. To address these, we propose an alternative filtering method whereby misfit dislocation formation is displaced, rather than halted. As detailed, this strategy proves very successful.

5.2 Threading Dislocation Density Reduction

5.2.1 Inherent dislocation reduction in zinc-blende films

Fortunately, we have found that simply growing thicker layer offers some inherent reduction in threading dislocation density (TDD). In GaAs, threading dislocations lie on {111} planes, as the thickness increases in the [001] direction, there is a finite probability they will get

sufficiently close to one another (50-100 nm)[144] to interact with one another. If they do not repel one another, they may simply annihilate, as shown in **Figure 5.1**.

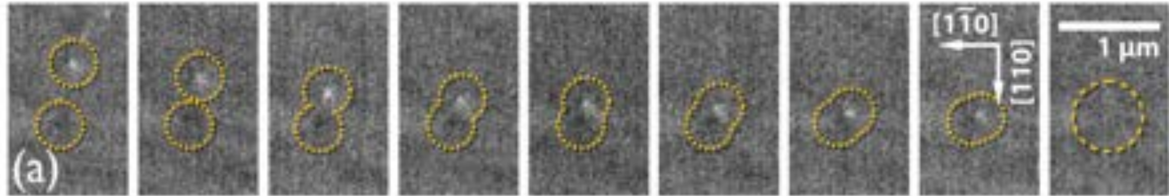

Figure 5.1 Two dislocations migrate towards each other on parallel glide planes and annihilate. Reprinted figure with permission from P. G. Callahan, B. B. Haidet, D. Jung, G. G. E. Seward, and K. Mukherjee*, Phys. Rev. Mater.*, 2, 081601, 2018. Copyright (2018) by the American Physical Society.

2→1 dislocation fusion reactions are more likely, but these too reduce TDD. And due to the face-centered cubic basis, fusions necessarily require the participation of two glissile dislocations and one sessile one. Thus, Ward et al. report that the fraction of glissile dislocations in will approach 0.5 in GaAs, which in turn will enable continued TDD reduction.[145] Note that there is some variance in the reported the literature regarding the exact relationship between TDD and thickness—Speck et al. report TDD [144] while George et al. report TDD —[38] and that this technique is not a practical dislocation reduction strategy for dislocation densities cm^{-2}. Note also that while the threading dislocation density reduces with increasingly thick layers of GaAs on Si, the stress due to the thermal expansion mismatch increases. This results in crack formation, an alternative strain relief mechanism.[102]

5.2.2 Thermal Cyclic Annealing

Thermal Cyclic Annealing (TCA) takes advantage of the mismatch in CTE between silicon and GaAs and intentionally exploits it for the purposes of dislocation reduction.[146] After growth, the temperature is ramped between up to intentionally put the film under compressive stress and drive dislocations to glide. This is because moving threading dislocations are far more likely to encounter another threading dislocation than static ones. Next the temperature is ramped down below the growth temperature. This in turn introduces tensile stress and drives the TDs to glide again. Cycling the temperature between a low and high temperature limits is the most effective method for a significant reduction in TDD in GaAs/Si films. Comparing a simple anneal of the structure to cycling with an equivalent amount of time spent high temp (800 °C) Yamaguchi et al. found the latter decreases TDD by 10X more than the former, as shown in **Figure 5.2**.[37]

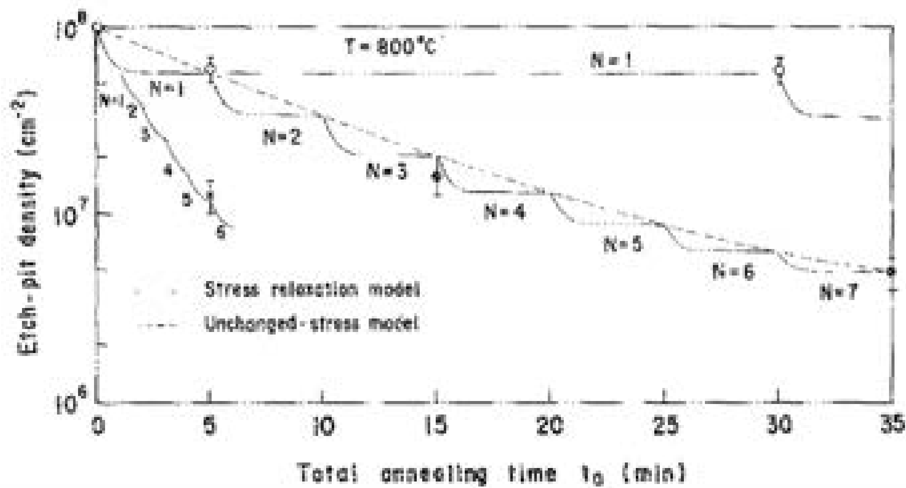

Figure 5.2 Changes in etch pit density in GaAs films on Si due to thermal annealing and thermal cycle growth under several conditions. Case 1: a single 30 minute anneal at 800°C (N = 1); case 2: 5 minute anneals at 800°C with 1, 3, and 7 temperature cycles; case 3: 1 minute anneals at 800°C and 6 temperature cycles. The solid lines show the calculated results using an exponential stress relaxation model $\sigma = \sigma_0 \exp\left(\frac{-t}{r}\right)$ where r is the stress relaxation time constant and the dotted lines present an unchanged stress model, respectively. Reprinted from M. Yamaguchi, A. Yamamoto, M. Tachikawa, Y. Itoh, and M. Sugo, "Defect reduction effects in GaAs on Si substrates by thermal annealing," *Appl. Phys. Lett.*, vol. 53, no. 23, pp. 2293–2295, Dec. 1988, doi: 10.1063/1.100257, with the permission of AIP Publishing.

5.2.3 Lattice Mismatch Based Dislocation Filtering Techniques

Just as thermal expansion both can generate defects and be leveraged for their reduction, so too can lattice mismatch. Likewise, the goal in both cases is to induce dislocation glide such that fusion (2→1) and annihilation (2→0) reactions occur. This is done through the intentional inclusion of additional heteroepitaxial layers with thicknesses ($h > h_c$). Often, for our system, $In_xGa_{1-x}As$ alloys are used. There are two main approaches: block single-composition interlayers[41], [147], [148] and strained layer super lattices[38], [39], [149]. **Figure 5.3** and

Figure 5.4 show these two approaches, the dark contrast in both images is due to large amounts of strain contrast in the relevant layers. In both cases, the TDD is noticeably reduced. Although it is not visible at this magnification, the three horizontal regions of dark contrast are comprised of five 10 nm $In_{0.18}Ga_{0.82}As$ layers and four 10 nm GaAs layers in **Figure 5.4**. There are scattered reports in the literature that, much like growth of thick films, some of these strategies lead to cracking.[60], [148] However it is unclear how common this is due to possible underreporting.

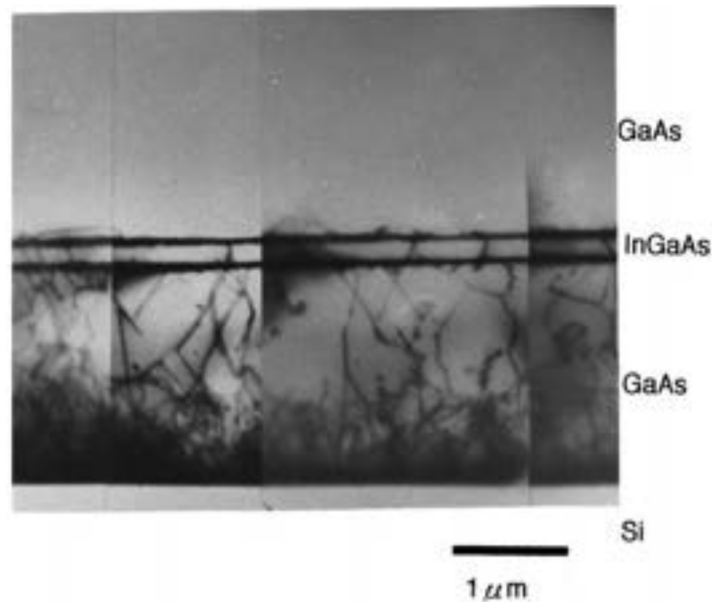

Figure 5.3 Cross-sectional TEM image of GaAs with an $In_{0.07}Ga_{0.93}As$ interlayer on a Si substrate (**g** = **220**). Reprinted from Y. Takano, M. Hisaka, N. Fujii, K. Suzuki, K. Kuwahara, and S. Fuke, "Reduction of threading dislocations by InGaAs interlayer in GaAs layers grown on Si substrates," *Appl. Phys. Lett.*, vol. 73, no. 20, pp. 2917–2919, Nov. 1998, doi: 10.1063/1.122629, with the permission of AIP Publishing.

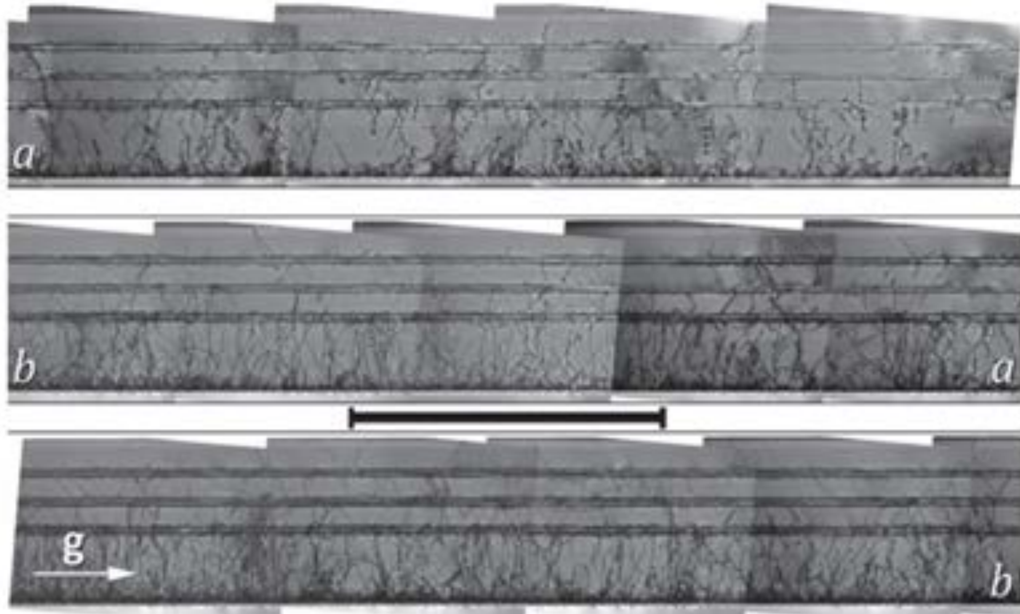

Figure 5.4 13 bright field TEM cross sectional images (**g**=**220**) of a sample with three strained superlattice dislocation filters, each composed of five 10 nm $In_{0.18}Ga_{0.82}As$ layers and four 10 nm GaAs layers. The images join at edges a–a and b–b. Scale bar = 5 μm. After ref. [38]

5.3 Misfit Dislocation Filtering

As I previously alluded to briefly, our team identified key components that enable the formation of misfit dislocations in the active region of our QD lasers:

(1) lattice hardening in the active region due to alloy hardening and coherent strain hardening and,

(2) tensile stress in the film from thermal expansion mismatch.

We took a non-traditional approach to address this, rather than attempting to remove the misfit dislocations entirely, we inserted thin (i.e., $h < h_c$), strained indium-alloyed "trapping layers" a short distance both above and below the laser active region. This has the effect of extending

the mechanically hardened region, displacing misfit dislocation formation away from the QDs. We validated this approach using both studies on model structures and studies on full lasers, as detailed below. Note that, all the samples in **Section 5.3** were grown using molecular beam epitaxy by Dr. Justin C. Norman and Mr. Chen Shang. Dr. Norman was with the Bowers group at the time of these experiments and has subsequently joined Quintessent, Inc.; Mr. Shang remains a student in the group. Note also that the CL measurements in **Section 5.3** were performed by Dr. Michael E. Salmon at EAG Laboratories-Eurofins Materials Science in Raleigh, NC. Finally, note that the ECCI measurements were performed by Mr. Eamonn T. Hughes who remains a student in the Bowers and Mukherjee groups at UCSB.

5.3.1 Investigation of Trapping Layers in Model Structures

Model Structure

Throughout this Section I refer to structures with trapping layers as "trapping layer" structures and those without as "baseline" structures. Here, the baseline consists of a single molecular-beam-epitaxy-grown QD layer capped with 100 nm of GaAs and grown on a GaAs-on-Si template. **Figure 5.5a** presents a schematic of the full baseline structure, while **Figure 5.5b** presents the buffer structure. The trapping layer structure, **Figure 5.5c**, includes a 7 nm $In_{0.15}Ga_{0.85}As$ and an addition 100 nm GaAs spacer, separating it from the QD layer, but it otherwise equivalent.

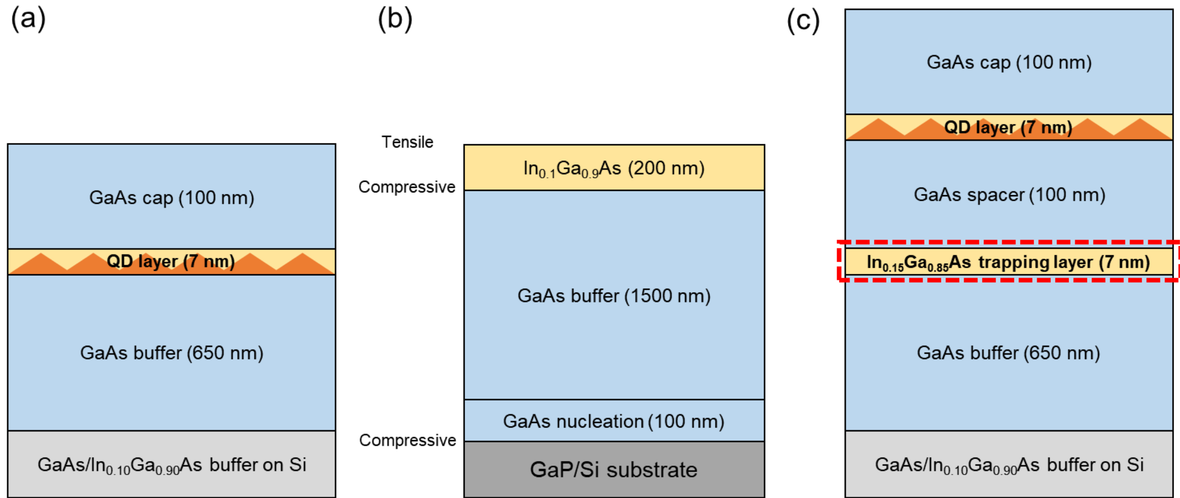

Figure 5.5 Schematics of **(a)** the baseline model structure, **(b)** the buffer design used for samples in this **Chapter** and, **(c)** the trapping layer model structure. In (b) mismatched interfaces, where misfit dislocations nucleate during growth, are marked with the sign of strain relieved.

The III-V/Si buffer was grown on a commercially available GaP/Si template available from $NAsP_{III/V}$, GmbH. My colleagues grew a 100-nm GaAs nucleation layer at 500 °C with 0.1 µm/h growth rate. Next, they grew a 1500-nm GaAs buffer at 580 °C and 1 µm/h. Subsequently, a twelve cycle TCA was performed with max. temp. = 700 °C and min. temp. = 400 °C. After the TCA, a 200-nm $In_{0.1}Ga_{0.9}As$ layer was grown. The DWELLs were grown at 490 °C and annealed at 580 °C for 5 min before growing the spacer layer. Each DWELL has a V/III ratio of 15 in the 2-nm $In_{0.15}Ga_{0.85}As$ below the dots. To form the dots themselves, 2.55 ML of InAs were deposited at .11 ML/s with V/III of 35. This was immediately followed by the deposition of the 5 nm $In_{0.15}Ga_{0.85}As$ cap which was also done with V/III of 35. Following the anneal, spacer layers were grown at 530 °C. The trapping layer here and the subsequent ones in this Chapter were grown at 530 °C with a V/III of ~35 and a growth rate of 2.12 Å/s.

CL Investigation of Model structures

Using SEM CL, to investigate the baseline, we observe a network of dark lines (misfit dislocations) and dark spots (threading dislocations), consistent with the experiment outlined in **Chapter 4**. The CL maps presented in this Section, (**Figures 5.6a-b** and **Figure 5.6d-e**) were collected at room temperature using an Attolight Rosa system with an accelerating voltage of 10 kV, ≈10-nA probe current, and 0.1s per pixel exposure. The QD wetting layer and ground state emission maps were collected using an Andor Newton CCD DU920P-Bx-DD silicon detector and an Andor iDus InGaAs detector, respectively.

In **Figure 5.6a**, the sharp, dark lines in the wetting layer emission map indicate that the misfit dislocation segments lie adjacent to the QDs, consistent with the analysis of **Figure 4.6c**. While, they appear more diffuse from inhomogeneous strain and uneven carrier confinement, the InAs QD ground-state luminescence map presented in **Figure 5.6b** has equivalent dark features.

As discussed in more detail in **Chapter 3**, we believed the misfits formed not due to lattice mismatch, but instead due to thermal strain and localized mechanical hardening in the QD layer. However, our attempts to alloy harden the entire laser stack by adding indium throughout resulted in an even large number of misfit dislocations at the QD layer from lattice mismatch.[62] Thus, we expected misfit dislocation formation would be very difficult to avoid entirely and sought instead to extend the lattice hardened region slightly further by adding a trapping layer and thus prevent misfit dislocation formation at the QD layer itself. The results—a 95% reduction in total dark line length—are presented in **Figure 5.6d-e**. We believe that the faint broad dark lines are a result of limited SRH losses at trapped misfit

dislocations. The trapping layer introduces an additional threading dislocation pinning point, as shown in **Figure 5.6f**. Because the thin intermediate GaAs is below the *thermal* critical thickness, dislocation glide and misfit formation occur almost exclusively below the trapping layer. Nevertheless, the presence of a few remaining dark-line segments indicated some misfit segments have not been trapped. While these un-trapped are clearly in the minority, identifying their formation mechanism remains an active area of research in Bowers and Mukherjee groups.

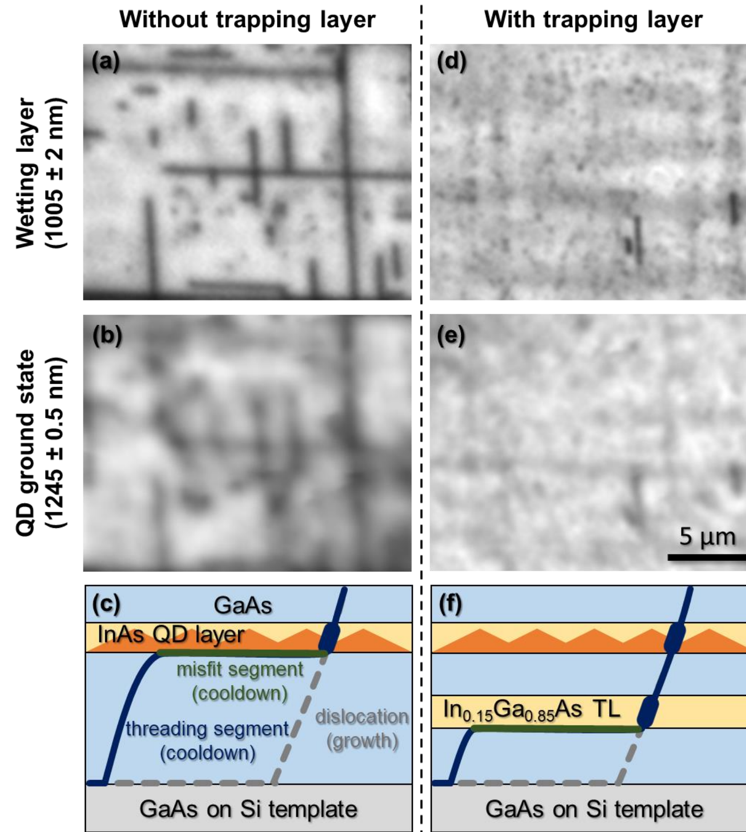

Figure 5.6 (a-b) Monochromatic cathodoluminescence images of the baseline structure from **(a)** QD wetting-layer emission (1005 nm) and **(b)** QD ground-state emission (1245 nm). **(c)** Schematic representation of misfit dislocation formation in the baseline. During cooldown, tensile stress builds in the film, because the film contracts more quickly than the substrate. The threading segment (blue line) in the thick underlying GaAs layer glides from its growth position (gray dotted line) to relieve the strain. The threading segment is pinned where it crosses the QD layer (blue box), causing a misfit segment (green line) to form at the bottom interface. **(d-e)** CL emission maps of the trapping layer structure from **(d)** the wetting layer **(e)** and the QD ground state. The trapping layer reduces the dark line defect length by 95% by **(f)** introducing an additional threading segment pinning point to displace misfit dislocation formation. Reprinted from J. Selvidge et al., "Defect filtering for thermal expansion induced dislocations in III–V lasers on silicon," *Appl. Phys. Lett.*, vol. 117, no. 12, p. 122101, Sep. 2020, doi: 10.1063/5.0023378, with the permission of AIP Publishing.

Comparing Mechanical Properties in QD layers and Trapping Layers

While the pinning points appear identical in the schematic in **Figure 5.6f**, we do not expect the magnitude of the pinning shear to be equivalent in the two layers. To better understand the

differences, **Figure 5.7** presents a somewhat more nuanced, although admittedly still simplified picture of pinning in the two adjacent layers. We consider the threading dislocation in **Figure 5.7a** to be completely mobile in GaAs and pinned in both the $In_{0.15}Ga_{0.85}As$ trapping layer and the QD layer above it.

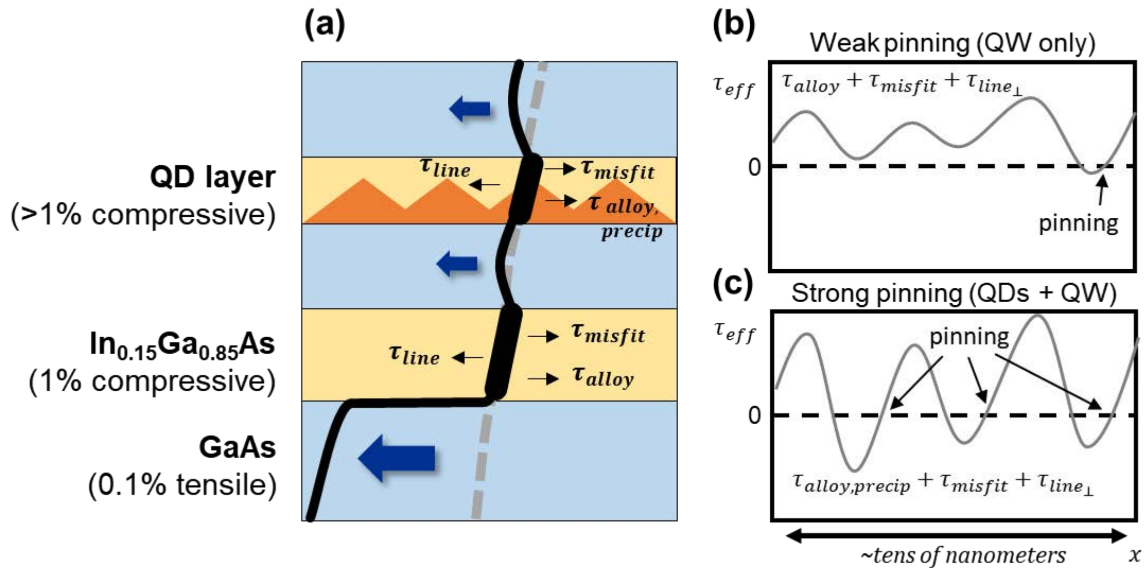

Figure 5.7. **(a)** Schematic showing a threading dislocation in a GaAs-based film on Si that is pinned at two points: an InAs DWELL layer and an $In_{0.15}Ga_{0.85}As$ trapping layer. In the $In_{0.15}Ga_{0.85}As$ trapping layer and the QD layer, τ_{line} represents the shear due to dislocation line tension; τ_{misfit}, the shear due to lattice mismatch between GaAs and the strained indium-alloyed layers, τ_{alloy} represents the resistive alloy hardening shear due to alloy compositional fluctuations and, τ_{precip} represents the resistive shear due to the precipitate-like quantum dots. **(b-c)** Rough sketches of the effective stress landscape in **(b)** the $In_{0.15}Ga_{0.85}As$ trapping layer and **(c)** the QD layer. While the pinning in the TL is relatively weak, the combination of QDs inside a QW results in strong pinning. Reprinted from J. Selvidge et al., "Defect filtering for thermal expansion induced dislocations in III–V lasers on silicon," *Appl. Phys. Lett.*, vol. 117, no. 12, p. 122101, Sep. 2020, doi: 10.1063/5.0023378, with the permission of AIP Publishing.

To glide in the high crystalline quality GaAs, the threading dislocation segment only needs to overcome the short-range, interatomic Peierls stress, τ_p. The situation is more complex in trapping layer and the DWELL, so we apply the concept of an effective stress (τ_{eff}). By our

convention, the threading segments here can only glide leftward if τ_{eff} is positive.[98], [99], [101], [150] During cooldown, the sub-critical thickness $In_{0.15}Ga_{0.85}As$ and DWELL layers remain compressively strained. Thus, although threading segments in these layers experiences a shear stress (τ_{misfit}) due to this strain, it is, by definition, smaller, than the maximum value of the line tension of the dislocation ($\tau_{line_{\perp}}$). Normally, the shear from the dislocation line tension would drag these short threading segments along so no misfit segments would form.[99]

Yet misfit segments do form. Somewhere $\tau_{eff} = 0$. Alloy hardening (τ_{alloy}) provides this additional stress in the trapping layer. As alluded to previously, compositional variation in the alloy leads to a long-range varying stress landscape. We see misfit formation because at some point $|\tau_{alloy} + \tau_{misfit}| \geq \tau_{line\perp}$. When this occurs, the threading dislocation segment is pinned in the trapping layer, while the free segment glides away. The magnitude of the stress field in the QD layer is substantially larger (**Figure 5.7c**). In addition to the resistive shear due to the alloy hardening effect in the QW, the precipitate-like QDs also provide their own far stronger resistive shear, τ_{precip}, as discussed in **Chapter 3**. Note also that both the compressively strained trapping layer and QD layer will prevent misfit segments from gliding upward through them.

ECCI Investigation of Model Structures

We used ECCI, aligning to the intersection of the (400) and (220) channeling conditions in all cases, to gain additional insight into the misfit and threading dislocations' structural characteristics. Although the films experience a 0.15% tensile strain at room temperature,

glide kinetics normally prevent plastic relaxation below ~300 °C. However, electron irradiation in an SEM, revives misfit dislocation formation *in-situ* via REDG. The ECCI time-lapse series in **Figure 5.8a** presents the evolution of a single threading dislocation in the baseline. The time-lapse sequence was performed using a ThermoFisher Apreo S SEM scanning a 200 μm^2 area for 66 min at 30-kV accelerating voltage and 3-nA beam current. By chance, this dislocation did not glide during cooldown. But, assisted by REDM, now glides below the QD layer, forming lengthening a misfit segment. Note that the threading dislocation's point contrast, visible only where it exits the film surface, remains stationary. The contrast from the moving end gradually fades as the dislocation sinks below the ECCI detection depth. The threading dislocation segment at the film surface is stationary, while its opposite end glides freely, in agreement with the pictures presented in **Figure 5.6c**.

To gain a more complete picture, we compare misfit dislocation densities between the baseline and the trapping layer structure before and after heavy SEM irradiation (**Figure 5.8b-e**). Pre-imaging, post-imaging, and irradiation was performed using FEI Quanta 400F SEM. We observe misfit dislocations, marked with black arrow, in the as-grown baseline structure (**Figure 5.8b**). From their sharp contrast we know the lie near film surface; we expect they are just below the QD layer. Next, SEM irradiation was performed at 30-kV acceleration voltage and 100-nA beam current, scanning a 1725 μm^2 area for 14 min. After SEM irradiation, additional sharp-contrast misfit dislocation segments, marked with orange arrows, appear (**Figure 5.8c**).

The as-grown trapping-layer structure, presented in **Figure 5.8d**, has substantially fewer high-sharpness misfit dislocations; sharpness indicates depth in ECCI. Over 2500 μm^2,

we measure a twenty-fold reduction in QD-adjacent misfit dislocation length near the QDs, in agreement with the CL results. Following equivalent electron-beam irradiation we observe a high-density network of diffuse-contrast lines (**Figure 5.8e**). REDM continues to enable plastic flow, but the dislocations' diffuse contrast that they lie farther deeper in the structure.[151] We suspect they lie at the trapping layer. As the density of high-sharpness dislocations remains constant, SEM irradiation apparently does not lead to further glide at the QD layer.

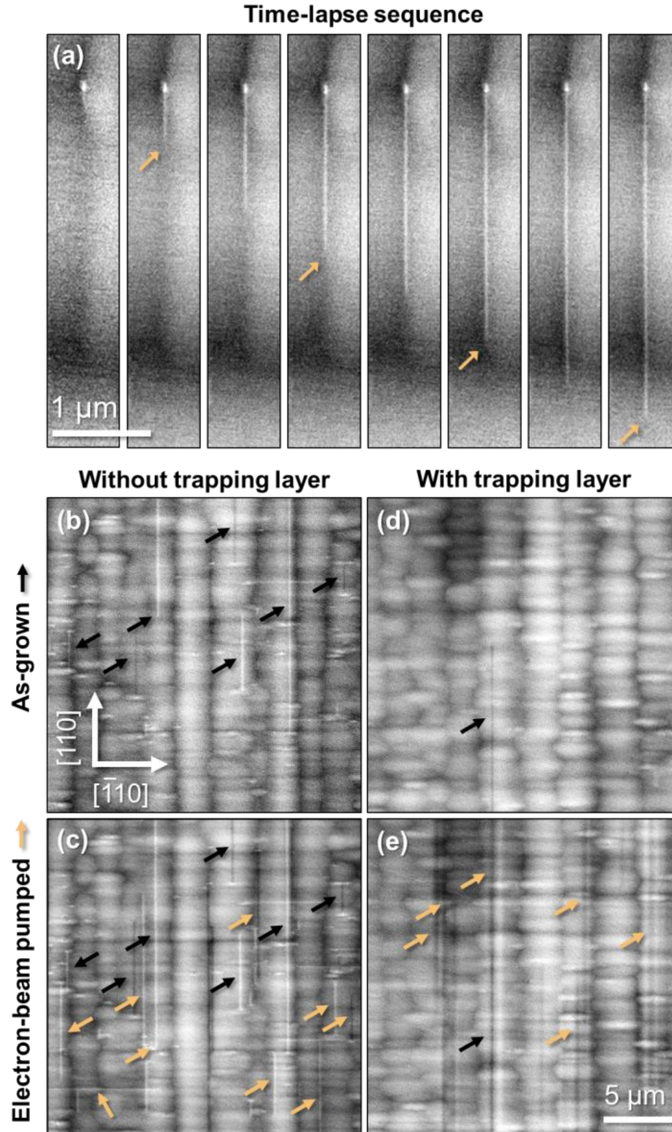

Figure 5.8 **(a)** ECCI time-lapse sequence (~550 s image interval) showing a misfit dislocation growing through REDG from an existing threading dislocation. As only the portion of the threading dislocation below the QD layer is free to move, the point contrast associated with termination of the threading dislocations at the top surface is stationary. **(b-c)** ECCI micrographs of the baseline structure **(b)** before and **(c)** after heavy *in situ* electron-beam irradiation. Black arrows indicate post-cooldown misfit dislocations and orange arrows indicate misfit-dislocation growth due to electron-beam irradiation. **(d-e)** Analogous ECCI micrographs of the trapping layer structure **(d)** before and **(e)** after electron-beam irradiation. Compared to the sharp line contrast misfit dislocations in (b-c), The more diffuse line contrast associated with the misfit dislocations in (e) arises because they are farther from the sample surface. Reprinted from J. Selvidge et al., "Defect filtering for thermal expansion induced dislocations in III–V lasers on silicon," *Appl. Phys. Lett.*, vol. 117, no. 12, p. 122101, Sep. 2020, doi: 10.1063/5.0023378, with the permission of AIP Publishing.

5.3.2 Trapping Layer Laser Characterization

Laser Design

We fabricated InAs DWELL ridge structures on (001) Si with trapping layers in the epitaxial stack, as shown schematically in **Figure 5.9**, alongside a baseline (**Fig. 5.9a**) sample with no trapping layers.[48] The growth details remained the same as in the model structures, with the following adaptations: layers prior to the QD layers were grown at 580 °C, while those following were grown at 540 °C. Additionally, the active region p-modulation doped to a level of 5×10^{17} cm^{-3}. However, unlike in the model structure, the material above the active region is sufficiently thick to relax during cooldown, so we insert a single 7-nm layer of $In_{0.15}Ga_{0.85}As$ above at and a single 7-nm layer of $In_{0.15}Al_{0.85}As$ below the active region to prevent of misfit-dislocation formation on both sides. We placed these layers at either 80 nm or 180 from the nearest QD layer and refer to these structures as 'TL80' (**Fig. 5.9b**) and 'TL180' (**Fig. 5.9c**), respectively.

The asymmetric alloys ($In_{0.15}Ga_{0.85}As$ on the p-side and $In_{0.15}Al_{0.85}As$ on the n-side) were selected to minimize electron and hole barriers formed by unfavorable band alignments in the laser. **Figure 5.10** demonstrates the reasoning behind this choice. Although these Silvaco simulations are clearly only an active region approximate band structure (they neglect the QD layers), they allow us to qualitatively compare the band offsets for structures (1) without trapping layers, (2) using $In_{0.15}Al_{0.85}As$ trapping layers on both sides of the junction, (3) using $In_{0.15}Ga_{0.85}As$ trapping layers on both sides of the junction, and (4) using $In_{0.15}Al_{0.85}As$ on the n-side and $In_{0.15}Ga_{0.85}As$ on the p-side. The fourth option minimizes the

valence band offset on the p-side and the conduction band offset on the n-side as shown. More accurate simulations are a subject of ongoing work in the Bowers and Mukherjee groups.

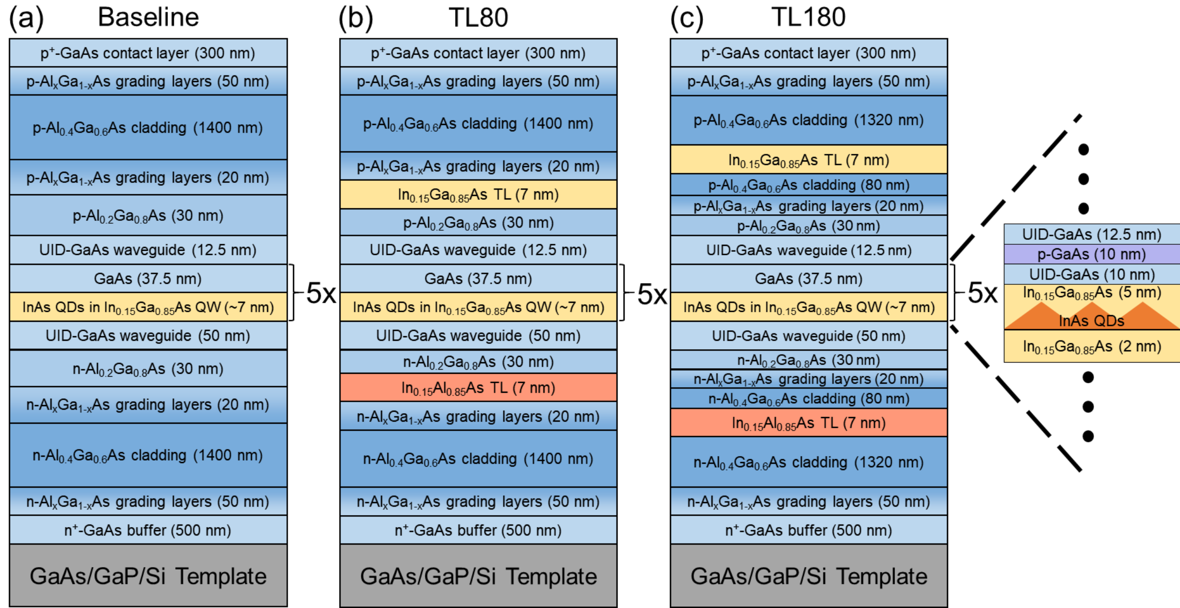

Figure 5.9 Schematics for **(a)** baseline, **(b)** TL80 (trapping layers 80 nm from quantum dots (QDs)), and **(c)** TL180 (trapping layers 180 nm from QDs) lasers.

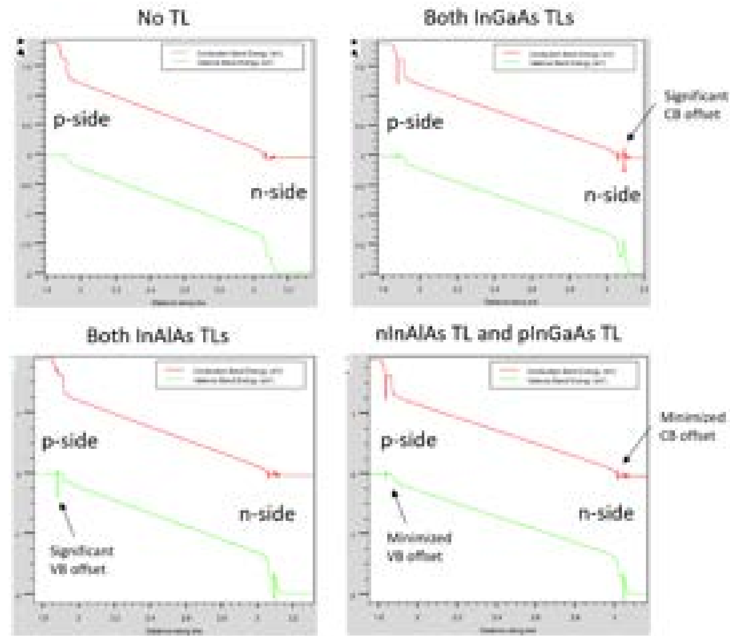

Figure 5.10 Simplified Silvaco band diagram simulations for devices with symmetrical and asymmetrical TL compositions. Using $In_{0.15}Al_{0.85}As$ in the n-cladding and $In_{0.15}Ga_{0.85}As$ in the p-cladding minimizes conduction band and valence band offsets, respectively. Note that these simulations neglect the quantum dots in the active region.

Cross-Sectional STEM Characterization

I first examined a laser with trapping layers located at 80 nm from the nearest QD layer using cross-sectional BF-STEM. Samples were prepared using standard lift out procedures on a FEI Helios Dualbeam Nanolab 600 and thinned to approximately 400 nm. All STEM images were acquired on a ThermoFisher Talos G2 200X TEM/STEM, using an excitation voltage of 200 kV, standard BF STEM circular detector, double tilt holder, and beam convergence angle of 10.5 mrad. The [100] foil orientation and on zone acquisition ensured the capture of misfit dislocation segments from the orthogonal ⟨110⟩ misfit dislocation networks. Misfit dislocations lie 45° to the foil thickness, thus their observed length is proportional to it. As

shown, misfit dislocations, marked with black arrows, lie at both the upper and lower trapping layers, successfully displaced away from the active region.

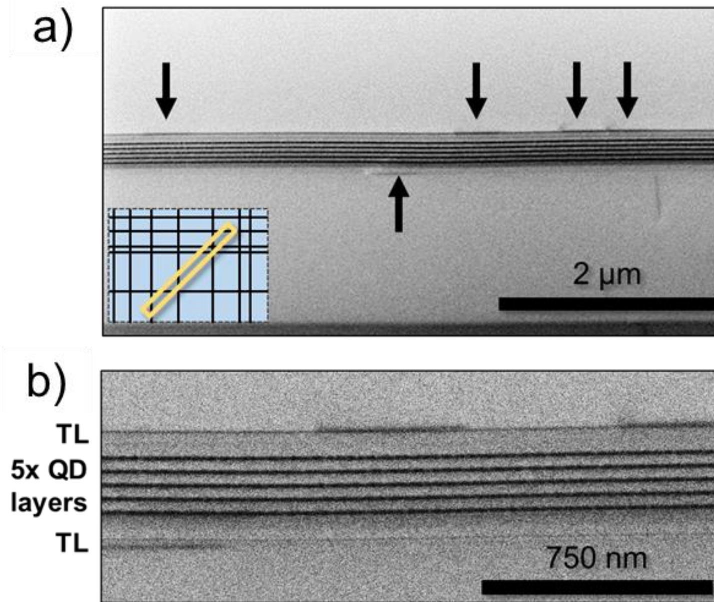

Figure 5.11 (a) Cross-sectional bright-field STEM image of a TL180 laser ([100] zone axis, convergence angle = 10.5 mrad). The foil is orientated at 45° to both orthogonal misfit dislocation networks, as shown schematically in the inset. Arrows mark misfit segments at the trapping layers which all appear the same length due to the foil orientation. **(b)** High-magnification image of (a) showing misfits trapped both above and below the active region. Reprinted from J. Selvidge et al., "Defect filtering for thermal expansion induced dislocations in III–V lasers on silicon," *Appl. Phys. Lett.*, vol. 117, no. 12, p. 122101, Sep. 2020, doi: 10.1063/5.0023378, with the permission of AIP Publishing.

For secondary verification I performed additional XSTEM using a [110] foil orientation. The images, acquired in a **g** = **002** diffraction condition, are presented in **Figure 5.12**. Threading dislocations, marked with black arrows, pass through the QD layers, and give rise to misfit segments at the top trapping layer. Due to the foil tilt, although the misfit segments connected to the threading dislocations in both images lie at the trapping layer, they appear to differ in height. From this, we can infer that the misfit segments (marked with white

arrows) lie at different depths from the surface of the foil. As a result of the tilt, the misfit dislocations lying in the direction of the foil thickness, marked with white arrows appear inclined.

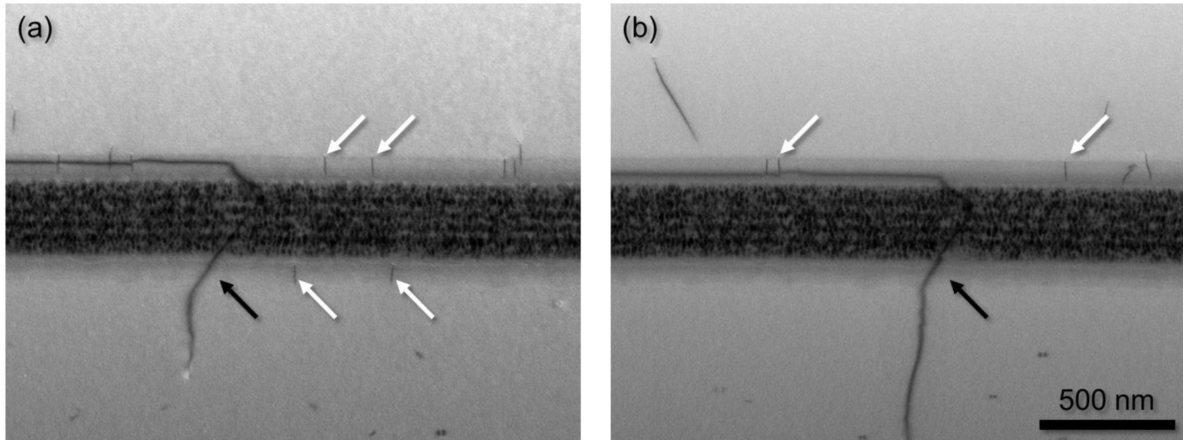

Figure 5.12 Both **(a)** and **(b)** show cross sectional scanning transmission electron micrographs of both misfit and threading dislocations in a TL80 laser (**g** = **002**). As the sample was lifted out parallel to the $[1\bar{1}0]$ oriented laser bars, certain misfits run parallel to the length of the foil and other run perpendicular to it (marked with white arrows). Due to the tilt, the perpendicular misfit dislocations appear as vertical lines. Likewise, the spacer layers between the quantum dots (QDs) are masked by the QD strain contrast. In agreement with **Figure 5.11**, the misfit dislocations here do not lie at the same height as the QDs. We can also see that the threading dislocations (black arrows) give rise to the misfit dislocations. The apparent difference in height between the parallel misfit dislocations indicates that they are at different depths from the foil surface. Reprinted from J. Selvidge et al., “Defect filtering for thermal expansion induced dislocations in III–V lasers on silicon,” *Appl. Phys. Lett.*, vol. 117, no. 12, p. 122101, Sep. 2020, doi: 10.1063/5.0023378, with the permission of AIP Publishing.

It is worth noting that QDs adjacent to the threading dislocation appear slightly different from the others both in density and in appearance. As these differences in QD morphology could only arise during growth, we can say with confidence that the threading dislocations have not moved from their growth positions with the QD layers themselves. The consistency between these images and **Figure 5.12a** and **Figure 5.12b** provides strong

evidence for the success of not only the lower trapping layer, but of the importance of the unusual upper trapping layer. I additionally note that, qualitatively based on the images presented in **Figure 5.11** and **Figure 5.12**, that the upper trapping layer appears to be either more important or more effective in the filtering of misfit dislocation length from the active region than the bottom trapping layer.

Due to the previously described difficulties associated with XSTEM imaging of dislocations in QD materials (see **Chapter 2**), to confirm the height of the misfit dislocations in the baseline we prepared a PV-STEM foil cut out slightly off-normal from the film surface. The sample was prepared milling inwards from the lower n-cladding towards the p-cladding. As such, on right side of the image presented in **Figure 5.13**, all layers are intact and imaged through. Moving to the leftward, QD layers are successively removed starting with the bottom layer until, on the left side, all QD layers are removed and only the upper p-cladding is being imaged. The five wavy contrast bands (orange arrows) correspond to the locations where the foil cuts through each QD layer. Horizontal misfit dislocations (white arrows) are cut off at the same place the as lowermost QD layer, indicating these dislocations lie at the first QD layer. On the other hand, vertical misfit dislocations (black arrows) are not cut off until the uppermost QD layer is removed, indicating they lie at the uppermost QD layer. The difference in the number and direction of misfit dislocations at the lowermost and uppermost QDs suggest that the relaxation processes occur independently in the n and p cladding. In agreement with **Figure 5.11** and **Figure 5.12**, the density of the misfit dislocation network adjacent to the p-cladding appears to be higher.

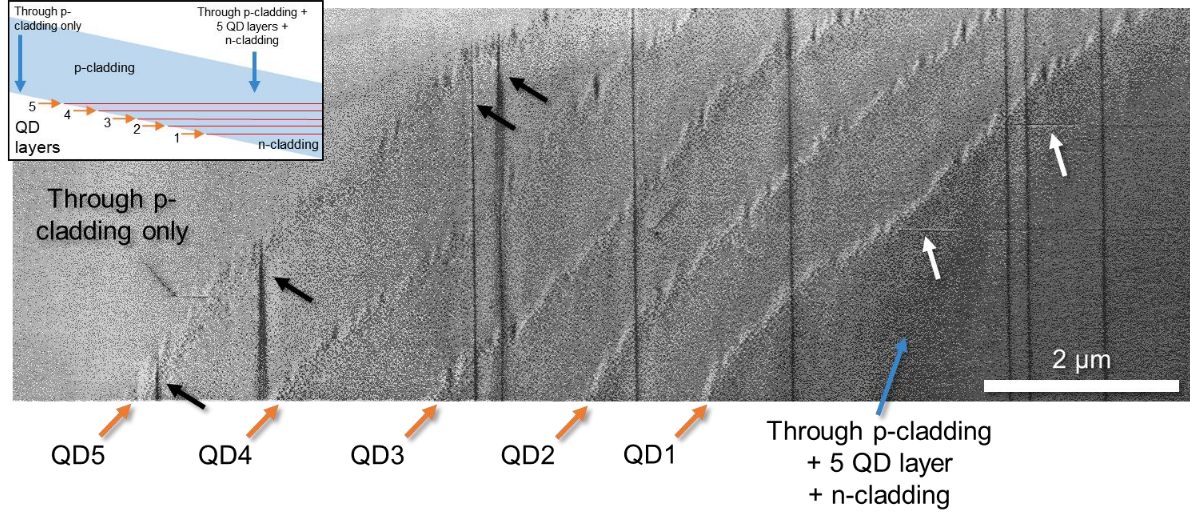

Figure 5.13 Bright-field plan-view STEM image of a baseline laser (**g**=$2\bar{2}0$). The inset depicts a cross-sectional view to assist the reader in understanding how the QD layers were successively removed along the length of the foil due to the offcut orientation. Orange arrows mark the intersections of the QD layers and the foil surface. The black arrows indicate misfit dislocations that lie just above the top QD layer (and are thus visible while only the 5th QD layer remains); while the white arrows indicate misfit dislocations that lie just below the bottom QD layer and thus disappear upon its removal.

Misfit Dislocation Network Asymmetries

As noted previously, **Figures 5.11-5.13** all appear to have a higher density of misfit dislocations on the p-side of the junction. We expect that this is a real effect. In contrast to the case of a simple GaAs-on-Si layer discussed in **Chapter 3** (see **Figure 3.11** for definition of terms and additional details), in the p-doped cladding (depicted in the upper schematic in **Figure 5.14**), the excess stress on the TD is *reduced* by the line tension component, τ_{l-p_clad}, where:

$$\tau_{l-p_clad} = -\frac{\mu b \cos\alpha \, (1 - \nu \cos^2 \beta)}{4\pi h(1-\nu)} \log\left(\frac{4h}{b}\right).$$

This is because, unlike in **Figure 3.11**, there is not a pre-existing compressive-strain-relieving misfit dislocation network at the p-doped cladding/active region interface to shrink. Thus, threading dislocation glide above the active region adjacent pinning points generates new tensile-strain-relieving misfit dislocation segments. Nevertheless, threading dislocation glide in the laser p-cladding and in a simple GaAs-on-Si structure are fundamentally similar as both have a free top surface.

In contrast, the n-doped cladding (lower schematic in **Figure 5.14**) has thick semiconductor layers both above and below, making the situation more complex. Unlike in the p-cladding, the n-cladding has a pre-existing, underlying misfit dislocation network. However, due to the InGaAs layer in the buffer structure (**Figure 5.5b**), that misfit dislocation network, lying at the interface of the buffer and n-doped laser cladding, relieves tensile strain. Therefore, when threading dislocation segments glide in the n-cladding they extend the pre-existing misfit dislocations. And, as the TD segment is pinned in the active region, a wide dipole structure necessarily forms across the n- doped cladding. In this scenario, threading dislocation experiences a line tensional shear given by:

$$\tau_{l-n_clad} = -\frac{\mu b \cos\alpha\,(1-\nu\cos^2\beta)}{4\pi h(1-\nu)}\left[\log\left(\frac{4(h+t)}{b}\right)+\log\left(\frac{4t}{b}\right)+2\log\left(\frac{h}{h+t}\right)\right],$$

where t is the thickness of the active layer and p-cladding. The first two terms represent the line tensions from each of the individual misfit dislocation segments and the third term accounts for the very weak interaction between the two misfit dislocations across the dipole.

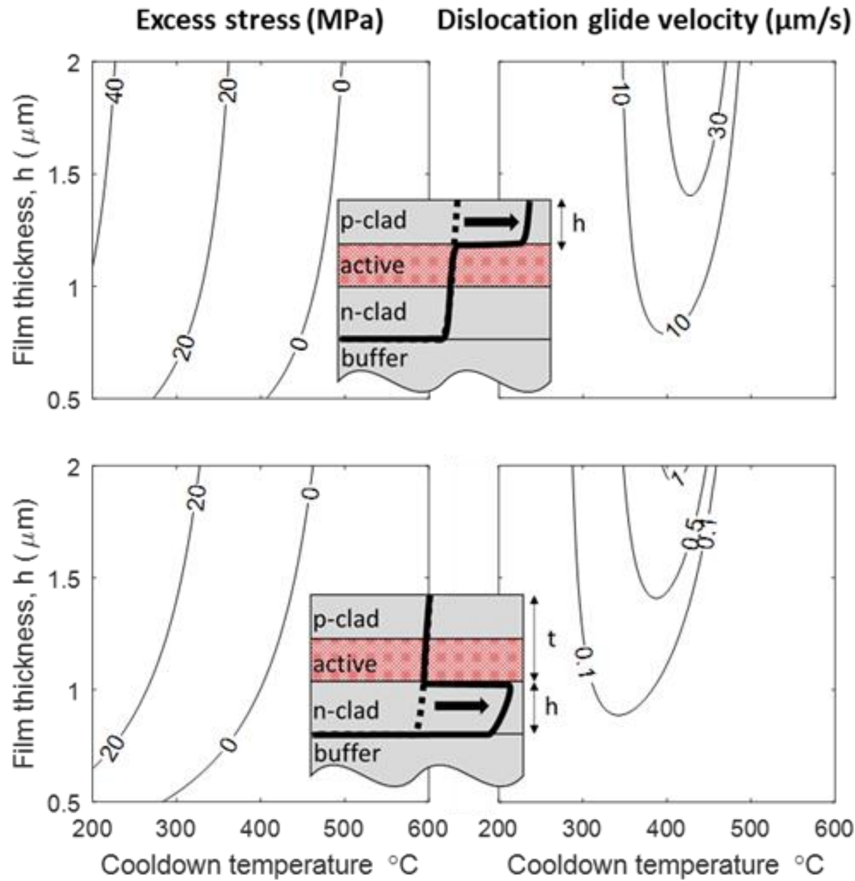

Figure 5.14 Excess stress and instantaneous dislocation glide velocity during cooldown in the p- and n-cladding and their distinct dislocation geometries. Film thickness, h, refers to the region where the threading dislocation segment glides in each case. Glide parameters for undoped GaAs α dislocations are used for light p-type doped cladding while those for n-doped GaAs α are used for n-cladding. t=2 μm for the n-doped cladding case and $\varepsilon_{res} = -0.02\%$ is assumed for both. After ref.[62]

The left column in **Figure 5.14** shows the excess stress on a threading dislocation segment in the p-cladding (top) and n-cladding (bottom) as a function of the cool down temperature and cladding thickness, assuming $\varepsilon_{res} = -0.02\%$. The calculation for the n-cladding also assumes $t = 2$ μm. In both cases, we see a relatively weak dependance on

cladding thickness, with threading dislocations experiencing a slightly increased τ_{ex} in thicker films.

As the differences in excess stress between the n-type and p-type cladding are also relatively small, we expect that the anisotropy in the densities of the two misfit dislocation networks arises primarily from the differences in threading dislocation glide kinetics due to doping and dislocation character. The parameters for dislocation glide velocities are experimentally determined and have not been measured for $Al_xGa_{1-x}As$, so we assume that they are equivalent to those measured for n-doped and undoped GaAs (substituting the latter for moderate p-doping) by Sumino and Yonenaga.[82] Using these assumptions, the righthand column in **Figure 5.14** shows the TD glide velocities corresponding to τ_{ex} for α-TDs in the n-type and p-type cladding. The orders of magnitude reduction in the calculated glide velocities between threading dislocations in the n-cladding as compared to the p-cladding support both the hypotheses that there is a real anisotropy in the densities and that it is primarily a kinetic effect.

PV-STEM Investigation of Trapping Layer Lasers

We additionally illustrate the differences between the TL80 and baseline structures at the single-dislocation level using cross-sectional strain-contrast electron tomography generated from multiple BF plan-view (PV)-STEM images taken across a range of tilt angles. We performed tomographic reconstructions of PV-STEM foils containing the laser active regions using a series of systematic row diffraction-contrast images obtained by tilting along the (220) Kikuchi band (**Figure 5.15a-f**). The detector served as a virtual aperture. Baseline samples were tilted (α) from -35° to 35° while TL80 was tilted from -28° to 28° (the increased foil

thickness of TL80 made ±35° tilt impractical). Remaining on Bragg condition necessitated small changes (approximately 4°) in the azimuth angle (β). We used Tomviz (https://tomviz.org) to obtain the cross-sectional reconstructions, manually aligning and optimizing the tilt axis for the sets of 9–11 images and using the 'Simple back projection' algorithm. **Figure 5.15a** and **Figure 5.15b** present a sample PV-STEM image for the baseline laser, showing a misfit dislocation amid a field of QDs, and the corresponding tomographic reconstruction, respectively. The reconstruction resolves the five QD layers and shows that this misfit dislocation lies at the uppermost QD layer.

Likewise, **Figure 5.15c** and **Figure 5.15d** show a PV-STEM image and the corresponding tomographic reconstruction, respectively, of a dislocation with a misfit segment and a terminating threading segment in a TL80 laser. Although strain-contrast tomography cannot resolve the trapping layer itself, the misfit segment clearly lies above the QD layers at the trapping layer's height. The threading segment travels downward through the five QD layers without forming additional misfit segments.

Figure 5.15e also shows a PV-STEM image of a dislocation in a TL80 laser, but here, there is a short down-sloping section along the misfit segment, which indicates a change in height. The tomographic reconstruction (**Figure 5.15f**) shows that these two segments lie at the trapping layer and uppermost QD layer. This configuration most likely forms because threading segments, normally pinned by the trapping layer, can become unpinned during cooldown and glide briefly before becoming pinned again. Since dislocation glide cannot occur within QD layers, a misfit segment forms at the outermost QD layer. This bears some resemblance to the incomplete misfit reduction observed by CL and ECCI, but this segment

of untrapped misfit is far shorter, suggesting its formation mechanism may be unique from the ones observed via SEM.

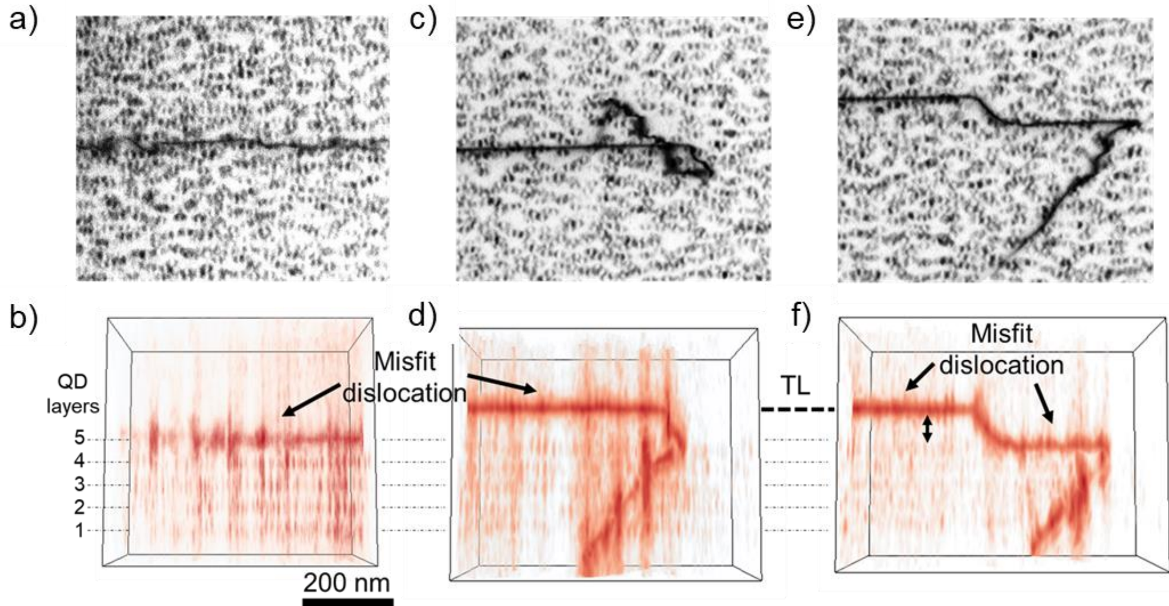

Figure 5.15 (a-b) Baseline **(a)** BF plan-view (PV)-STEM image (**g = 220**, convergence angle = 10.5 mrad) showing a misfit dislocation among a field of QDs. **(b)** Cross-sectional tomographic strain-contrast reconstruction showing that the misfit dislocation lies at the fifth QD layer. **(c-f)** TL80 **(c)** BF PV-STEM image showing a misfit dislocation terminating in a threading dislocation and **(d)** corresponding tomogram showing that the misfit segment lies at the trapping layer height. Note that due to insufficient strain contrast, the trapping layer itself is not resolved by the reconstruction. **(e)** BF-PVSTEM image showing misfit segments at two heights with a threading dislocation end and **(f)** corresponding tomographic reconstruction. The tomogram reveals a trapped misfit segment and an additional short misfit segment at the QD layer. Reprinted from J. Selvidge et al., "Defect filtering for thermal expansion induced dislocations in III–V lasers on silicon," *Appl. Phys. Lett.*, vol. 117, no. 12, p. 122101, Sep. 2020, doi: 10.1063/5.0023378, with the permission of AIP Publishing.

Nevertheless, just as in the model structures, the trapping layers are very successful here: most misfit dislocation length lies at the trapping layer, which we confirm with additional PV-STEM. **Figure 5.16** presents an aerial view of the trapping layer PV-STEM foil used to create tomographic reconstructions in **Figure 5.15d** and **Figure 5.15f**. Two perpendicular misfit

arrays lie at the trapping layers. Instances of incomplete pinning that form misfit dislocations at the QD layer occur infrequently (white arrows) and the length of misfit dislocation lying near the QD layer tends to be short. We identify these instances from the short threading segments indicating the height change. The inset shows the location of the dislocation examined in **Figures 5.15e-f**. Even so, incomplete trapping is surely detrimental. It therefore emphasizes the importance of trapping layer optimization.

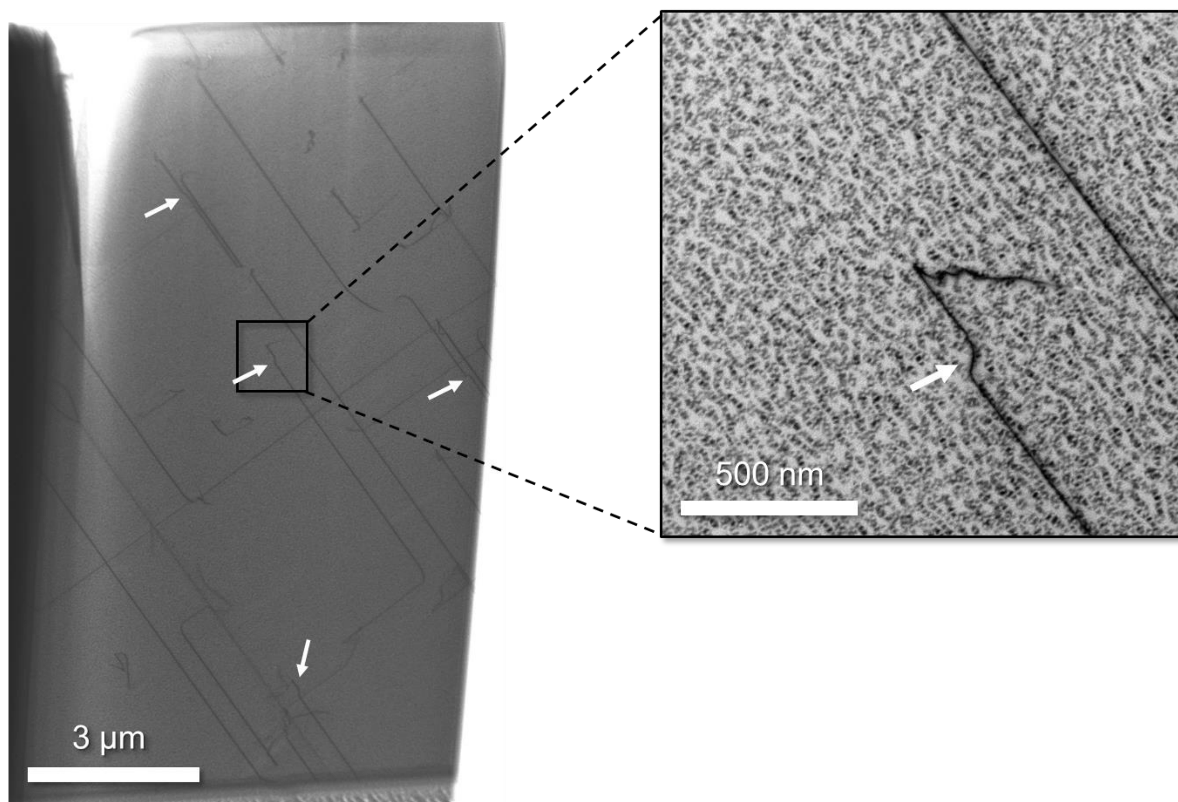

Figure 5.16 Large-area plan-view scanning transmission electron micrograph of the trapping layer foil. White arrows indicate instances of incomplete misfit dislocation trapping, identified by apparent height changes. Inset shows a magnified view of the dislocation displayed in **Figure 5.14e**.

Laser Performance Measurements

We began to explore the design space by investigating the effect of a single parameter—trapping layer height. Placing trapping layers farther from the QD layers likely reduces non-radiative recombination losses from trapping-layer misfit dislocations, but also may exacerbate incomplete pinning and return some misfit segments to the QD layers. To better understand the optimum spacing, we characterized the electro-optic properties of all three laser types (no-TL, TL80, and TL180). All three sample types were fabricated together and grown on pieces of the same buffer with a dislocation density of 3×10^7 cm^{-2}. The 3 μm wide, deeply etched ridge lasers were fabricated and cleaved to a length of 1500 μm. They have two topside contacts.

Photoluminescence spectroscopy and light output-current-voltage (LIV) curves of a representative high performing device from each design are shown in **Figure 5.17a** and **Figure 5.17b**, respectively. Photoluminescence measurements were carried out at room temperature using a non-resonant 780-nm pump laser with normal incidence pumping and detection; LIV measurements were conducted at 20 °C. Introducing trapping layers increases photoluminescence intensity by approximately 2× in TL80 and 1.5× in TL180 compared to baseline (**Figure 5.17a**). These results agree qualitatively with the marked improvements in single-facet output power (**Figure 5.17b**) in fully fabricated TL80 and TL180 lasers over baseline.

Histograms comparing the structures further support these performance improvements showing lower currents to begin lasing (threshold current: **Figure 5.17c**), more rapidly increasing output powers with input current (slope efficiency: **Figure 5.17d**), and higher peak

single-facet output powers (**Figure 5.17e**). Both trapping layer designs show a 2× reduction in median threshold current below baseline. The lowest threshold current, 15 mA on a TL180 laser, represents a 40% decrease from baseline minimum. This is also 25% lower than state-of-the-art lasers on Si, with identical device design but 4× lower threading dislocation density.[48] We additionally observe an impressive 60% (40%) increase in median slope efficiency and a 3.4× (2.6×) increase in median peak single-facet output powers for TL80 (TL180) lasers. As I will discuss in **Chapter 6** and alluded to in **Chapter 1**, these performance improvements correspond to order of magnitude lifetime improvements.

As SRH losses must be saturated for a lasing to begin, the link between effective misfit dislocation trapping and reductions in threshold current is intuitive. However, to understand the marked improvements in slope efficiency and peak output power, it is worth briefly considering how trapping layers may mitigate optical losses associated with dislocations. Although carrier loss at dislocations is necessarily saturated at the threshold current, the energy released in SRH recombination processes can lead to localized heating effects.[152]–[155] Under such circumstances, material in the vicinity of a dislocation could begin to act as a local absorber due to a slight reduction in its bandgap. Such a scenario agrees with the findings of Hakki and Paoli, who, in refs. [156], [157], identified 'local absorber defects' associated with asymmetric, single-facet spectral shifts and reductions in output power in degraded Ga/AlGaAs stripe lasers. Although the optical losses associated with these defects were more important under lasing conditions, they were also associated with small non-radiative excess currents consistent with SRH.[157] Given the marked reduction in threshold

and thus SRH at dislocations, it stands to reason that the trapping layers should also substantially reduce their associated optical absorption.

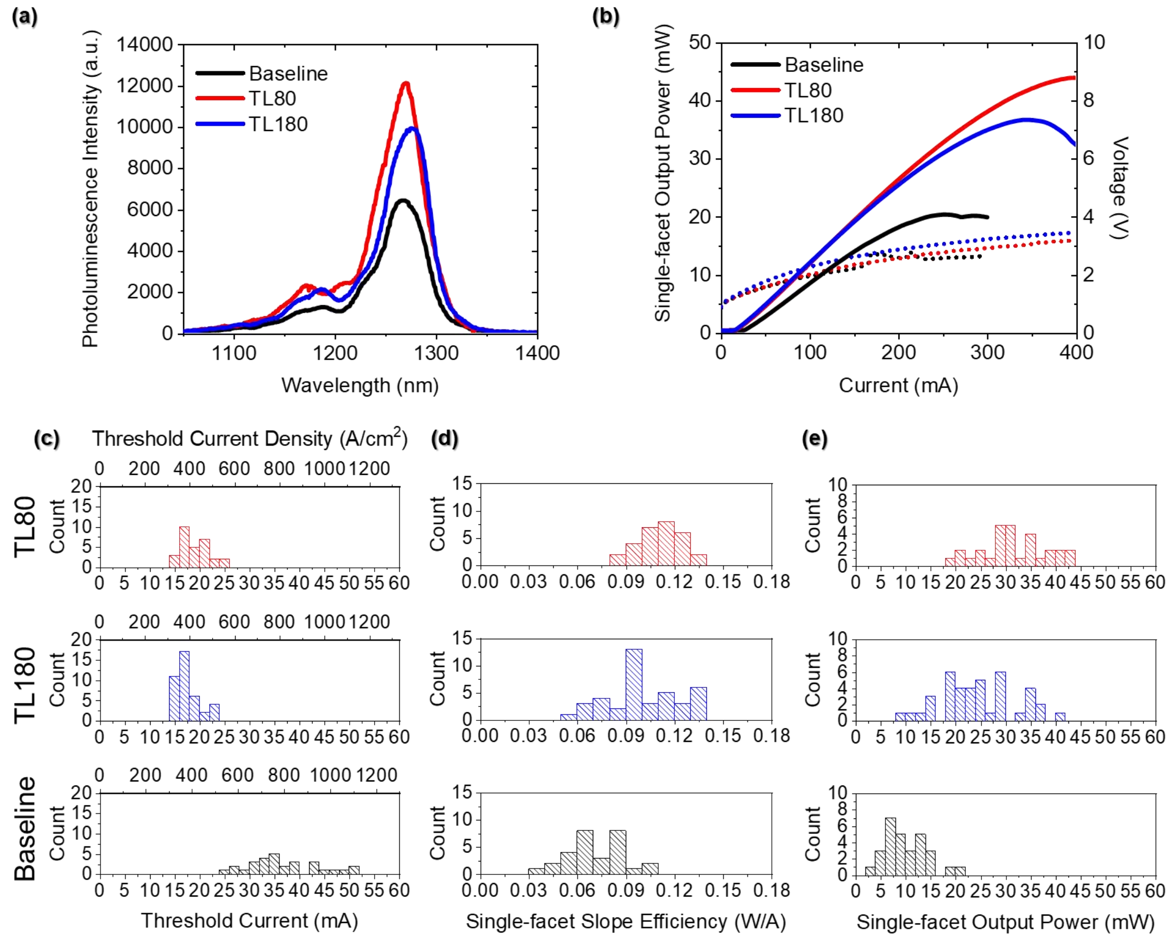

Figure 5.17 (a-e) Comparison of TL80 (red), TL180 (blue), and baseline (black) lasers. **(a)** Photoluminescence comparison of the three laser designs. **(b)** Single-facet output power (mW) (solid line) and voltage (V) (dashed lines) as a function of current (mA) (LI and IV curves, respectively). Including trapping layers improves LI behavior by reducing threshold currents, increasing slope efficiencies and, increasing peak output powers as compared to baseline. In contrast, the IV curves relatively similar across the three device designs. **(c-e)** Histograms comparing TL80, TL180, and baseline laser performance across **(c)** threshold current (mA) and threshold current density (A/cm^2), **(d)** single-facet slope efficiency (W/A), and **(e)** single-facet output power (mW). Both trapping layer designs show significant improvements over baseline. Adapted from ref.[51]

We also compared the electrically dissipated power at 'laser rollover' and present these histograms in **Figure 5.18**. Note that laser rollover is the current at which lasing output begins to decrease with current due to the onset of excited state lasing. We find that the median electrically dissipated power, in W, at rollover of TL80 (0.85) and TL180 (0.76) is nearly twice that of the baseline (0.46). Assuming comparable thermal impedances, the inclusion of trapping layers appears to have increased another critical parameter in these lasers: optical amplification (gain). However, it is also possible that, through the reduction of SRH recombination in the active region, we have effectively lowered the junction temperature, a possibility alluded to in the previous paragraph and explored further in **Chapter 6**. It is difficult to deconvolve these effects: gain decreases with increasing temperature so a reduction in junction temperature necessarily increases the gain by a corresponding amount.

Based on the data presented here, the TL80 laser design appears to slightly outperform the TL180 across all initial performance metrics aside from minimum and median threshold current. However, we cannot yet conclusively determine which design is superior. There was significant processing variability, across all the device designs, making it difficult to be conclusive. We anticipated that differences might emerge during long-term reliability studies due to the competition between improved trapping and increased distance from the active region, but, as discussed in **Chapter 6**, to date, this too has been somewhat inconclusive. Additionally, we cannot yet ascertain whether trapping layers adversely impact electrical transport in these lasers due to large variability in the series resistances across all three devices designs. As the higher-than-usual specific contact resistances across all devices (p: 2.3×10^{-5}

$\Omega \cdot cm^2$, n: 5.5×10^{-5} $\Omega \cdot cm^2$) represent a limiting factor on output power, processing modifications will likely improve device performance even further.

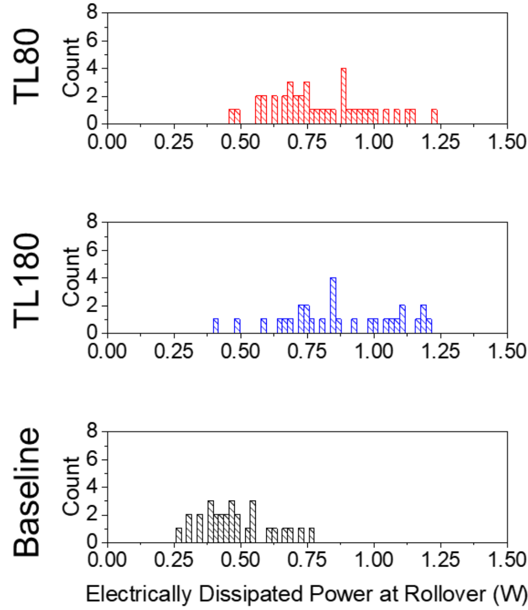

Figure 5.18 Histograms comparing the electrically dissipated power at rollover for TL80 (red), TL180 (blue) and baseline (black). Although there is some variability in the data, including trapping layers appears to increase the gain.

5.4 Summary

Researchers in the decades-long study of III-V on silicon integration have duly focused on reducing the density of threading dislocations. Our research demonstrates these threading dislocations additionally give rise to highly damaging but independently addressable misfit dislocations. We resolve this by introducing misfit-dislocation trapping layers both *above and below* the lasing active region. This represents a major departure from traditional defect

filtering and device design while remaining synergistic with ongoing efforts in threading-dislocation reduction. Recognizing that these misfit dislocations form not due to QD and QW layers exceeding critical thickness, as previously thought, but rather due to an unusual mix of thermal and lattice hardening effects occurring during sample cooldown, we provide clear pathways for continued laser performance improvements. Unfortunately, due to difficulties arising from the COVID-19 pandemic, to date we have not been able to perform optimization on any additional parameters. However, this provides plenty of opportunities for continuing research, the subject of **Chapter 7**. Luckily, we were able to assess the orders of magnitude reliability improvement available simply using these structures, which is the subject of **Chapter 6**.

Chapter 6:

Laser Reliability

6.1 Introduction

Like all complex engineering systems, lasers have a finite lifetime. However, the lifetimes of individual devices are highly variable. It is therefore useful to think about the device failure rate as being modeled by a bathtub curve, an example of which is shown in **Figure 6.1**.[158] In the early stages of operation, the failure rate will be relatively high; devices that fail during this period are referred to as infant failures. Infant failures arise due to pre-existing defects within the device such as large growth defects or errors in processing. Device screening procedures, such as burn-in procedures in which the devices are intentionally operated under high stress conditions (i.e., high currents and temperatures), are used to remove as many infant failure prone devices as possible prior to prolonged operation. This process intentionally induces failure in these devices and as such the failure rate during this period is relatively high. As time passes, more and more devices prone to infant failure will have already failed causing the overall failure rate at these later times to reduce. After this initial period and for much of the remainder of the device lifetime, the failure rate will be relatively low and flat. This corresponds to random device failures which we would expect to occur at a constant rate throughout the device lifetime. Near the end of the device lifetime, the failure rate begins to

dramatically increase because of wear-out failures, which is to say those failures attributed to gradual degradation of the material itself because of operation.

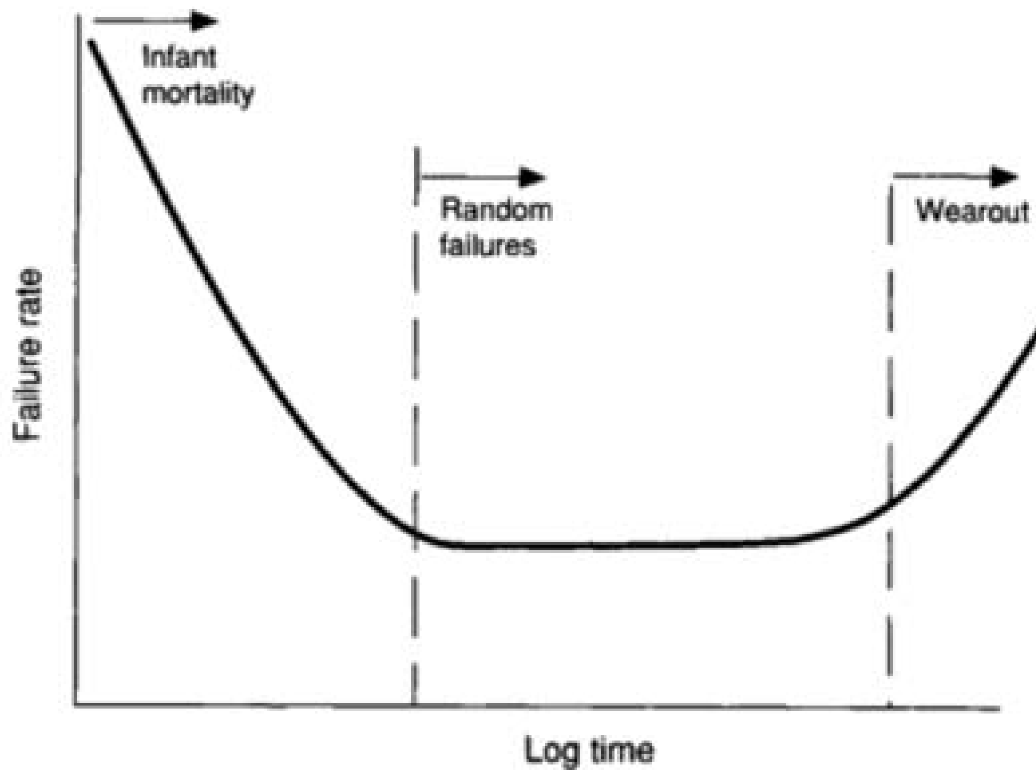

Figure 6.1 Device failure rate as a function of time. Initially, the failure rate is relatively large due to defective devices in the population. This drops rapidly and the failure rate becomes relatively low and stable, corresponding to random failure. Near the end of the devices' expected lifetime the failure rate begins to rise again due to wear out. Reprinted from *Engineering Materials Science*, M. Ohring, "15 - FAILURE AND RELIABILITY OF ELECTRONIC MATERIALS AND DEVICES,", 747-788, Copyright (1995), with permission from Elsevier.

6.2 Traditional Laser Failure Modes

In lasers specifically, we often define failure based on the timescale of the degradation process. There are three major classes—sudden (referred to as 'catastrophic'), rapid, and gradual—and different physical processes dominate each.

6.2.1 Catastrophic Failure

In Fabry Perot structures, catastrophic failure often occurs due to facet damage, specifically localized melting.[159]–[162] The process occurs when:

1) large amounts of non-radiative recombination occur at a cleaved facet or pre-existing defect due to high operating current causing an increase in the local temperature and corresponding reduction in the bandgap and,
2) large amounts of optical absorption occur due to the locally decreased bandgap, further increasing the local temperature to the melting point.

Crystalline defects, especially dislocations, form ahead of the molten front. **Figure 6.2** shows a TEM image of a $In_xGa_{1-x}As/GaAs$ strained QW laser diode that failed due to catastrophic optical damage.[163] As of this writing, we have not identified any facet specific failure modes in the lasers treated in the subsequent discussion, however, as we move towards higher output powers associated with the trapping layer designs and operate at increasing temperatures, these may become a concern.

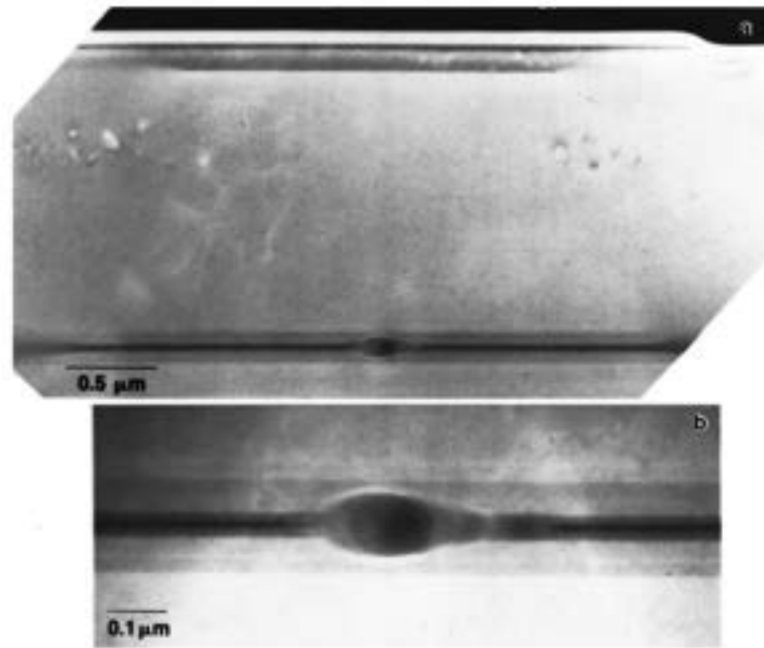

Figure 6.2 Dark-field cross-sectional TEM micrographs (**g** = **200**) showing **(a)** a melted and resolidified area caused by catastrophic optical damaged, and **(b)** a higher magnification image of the completely intermixed well/barrier/separate-confinement-heterostructure (SCH) region. Reprinted from S. N. G. Chu, N. Chand, W. B. Joyce, P. Parayanthal, and D. P. Wilt, “Generic degradation mechanism for 980 nm InxGa1−xAs/GaAs strained quantum-well lasers,” *Appl. Phys. Lett.*, vol. 78, no. 21, pp. 3166–3168, May 2001, doi: 10.1063/1.1371967, with the permission of AIP Publishing.

6.2.2 Rapid Failure

Historically, in widely used quantum well (QW) based lasers, rapid failure has occurred though recombination enhanced dislocation growth processes such as recombination enhanced dislocation climb (REDC)[21], [58], [59] and recombination enhanced dislocation glide (REDG)[135], [164]. To address this problem, decades of work went into improving the crystalline quality of III-V substrates which is to say reducing their dislocation density by orders of magnitude. However, as detailed in the previous Chapters, such strategies will not

work for GaAs on Si. Thus, failure in QW-based GaAs on Si structures occurs in a matter of minutes to hundreds of hours.[26], [27], [29], [33], [34] For a full discussion of these processes, see **Chapter 4**.

6.2.3 Gradual Failure

As a result of efforts to improve native substrate quality, dislocation mediated failure mechanisms were effectively eliminated in those devices and gradual point defect mediated failure mechanisms became the most common wear-out failure modes. These vary by materials system. In GaAs-based systems the most important gradual degradation mechanisms is the gradual increase in the density of deep-level defects.[165], [166] These have been shown to eventually precipitate out as nano-scale dislocation loops. **Figure 6.3** presents an overview of this degradation mechanism. **Figures 6.3a-b** showing BF-TEM images from the active region of undegraded (**Fig. 6.3a**) and degraded (**Fig. 6.3b**) AlGaAs LEDs. The degraded device was operated at 556A/cm^2 for 7100 h. The junction temperature was 169 °C. The appearance of the nano-scale dislocation loops correlates with the observed increase in deep-level defects (**Fig. 6.3c**). Likewise, the precipitation of point defect aggregates (nano-scale dislocation loops etc.) also constitutes a key failure mode in InGaAsP/InP-based devices.[167], [168] Interdiffusion of Au atoms into the active region have also been shown to lead to failure in InGaAsP/InP devices.[169]

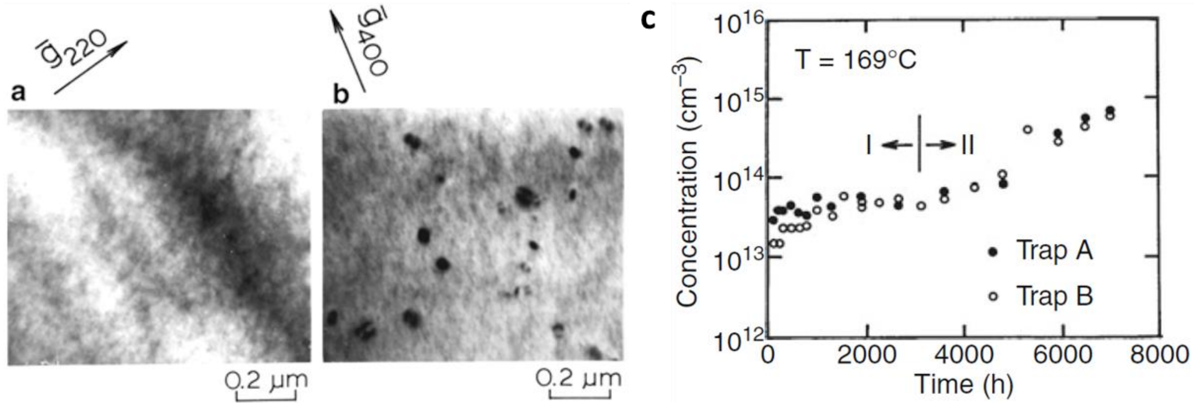

Figure 6.3 (a-b) Bright-field TEM images of the active regions of AlGaAs DH LEDs **(a)** before operation and **(b)** after operation for 7,100 hours (current density=556 A/cm^2, junction temperature=169°C). **(c)** Concentration of deep-level defects in AlGaAs DH LEDs as a function of the operating time. After ref.[165] © 1983 IEEE.

6.2.4 Accelerating Factors

Degradation rates, for non-instantaneous failure modes, are highly sensitive to internal and external device operating conditions. The change in the mean-time-to-failure (MTTF) is frequently modeled using the following relationship:

$$MTTF = AJ^{-n}\exp\left(\frac{E_a}{kT}\right)$$

where A is a constant, J is the current density, n is the current acceleration factor, E_a is the thermal acceleration activation energy, and kT is the thermal energy of the system.

Using data from Jung et al. data, reported in ref.[40], Norman et al. report $E_a = 0.9$eV and $n \cong 3.5$. This corresponds to, approximately, a three order of magnitude reduction in laser lifetime between 35 °C and 60 °C, as the current required for $2I_{th}$operation also has an

exponential dependence on temperature ($I_{th} \propto \exp\left(\frac{T}{T_0}\right)$, with $T_0 = 30$ K for these specific devices). Thus, low operating currents and temperature tolerant device designs are critical. Likewise, heat extraction from devices is a key concern, but, in this, GaAs-based devices on silicon have an advantage over their native substrate counterparts due to silicon's higher thermal conductivity.

While temperature and operating current are the most critical considerations in designing for reliability, they are certainly not the only ones. Internal stress, for example, has been shown to accelerate device failure in AlGaAs based laser designs.[166], [170] Likewise, external environmental factors, such as radiation, can both activate new failure pathways and accelerate existing ones.[171] GS vs. FES lasing is another critical consideration for QD laser reliability, as the latter has shown to significantly accelerated degradation.[172]

6.3 Failure Modes in Lasers with Misfit Trapping Layers

I performed comprehensive electron microscopy analyses on the ridge laser structures described in **Figure 5.9** after aging at 60 °C. This allowed my colleagues and I to link degradation in device performance to structural changes in the dislocations. The relatively high TDD templates (2–4×10^7 cm^{-2}) facilitate an investigation into the significant impact of MDs over TDs. We found that misfit dislocation facilitated degradation was far more detrimental than threading dislocation facilitated degradation and reducing it improves device reliability by several orders of magnitude. We additionally sought to characterize the interplay

between competing factors that differentiate our TL80 and TL180 structures: trapping layer efficiency and misfit dislocation distance from the active region.

6.3.1 Lifetime Testing Conditions

Prior to aging, we coated the laser bars with quarter-wave thickness SiO_2 and Ta_2O_5 layers for 60% (1 pair) and 99% (8 pairs) reflectivity on front and back facets, respectively. This reduces threshold current and should help protect the facets from degradation, allowing us to investigate the degradation due to the pre-existing misfit dislocations. After the bars were then singulated, soldered onto AlN carriers, and wirebonded, we loaded them into a Newport ILX Lightwave LRS-9434 laser diode reliability test system. In the first study, we aged three No-TL, five TL180, six TL80 ridge lasers (3 μm × 1500 μm) under automatic current control (ACC) at 60 °C. This small sample size arose because we excluded any devices with a threshold current density above 500 A cm^{-2} or a maximum output power below 10 mW at 20 °C after facet coating, as we expected this metrics suggested errors in processing and/or mounting. We operated the devices continuously for up to 3000 hours at approximately twice their initial 60 °C threshold current—70 mA for the No-TL devices and 37 mA for the TL devices. Light output-current (LI) and voltage-current (VI) measurements were collected automatically at 35 °C and 60 °C every 50 hours. Note that Mr. Eamonn T. Hughes performed the lifetime testing; he remains a student in the Bowers and Mukherjee groups at UCSB.

6.3.2 Device Reliability Characterization

Figures 6.4a-6.4c present the LI and IV measurements over time for a high performing device from each group. The No-TL laser clearly degrades significantly more than either TL laser,

despite similar turn-on voltages and series resistance. The decreases in rollover current over time and the gradual degradation of the IV curves could suggest increasing junction temperature due to increased non-radiative recombination. These effects appear to be less pronounced in TL80. **Figures 6.4d-6.4g** summarize various degradation metrics (change in threshold current, peak power, current required for 10 mW of output power, and current at rollover, respectively) extracted from the LI curves. The No-TL device's output power falls below 10 mW after only 600 hours. After 3000 hours, its threshold current increases by 55% and its peak output power drops 48%. In contrast, both TL devices undergo less than 9% increases in the threshold current and current required for 10 mW of output power. This TL80 device appears to perform the best: its peak power drop is only 11%, compared to TL180's 20% drop.

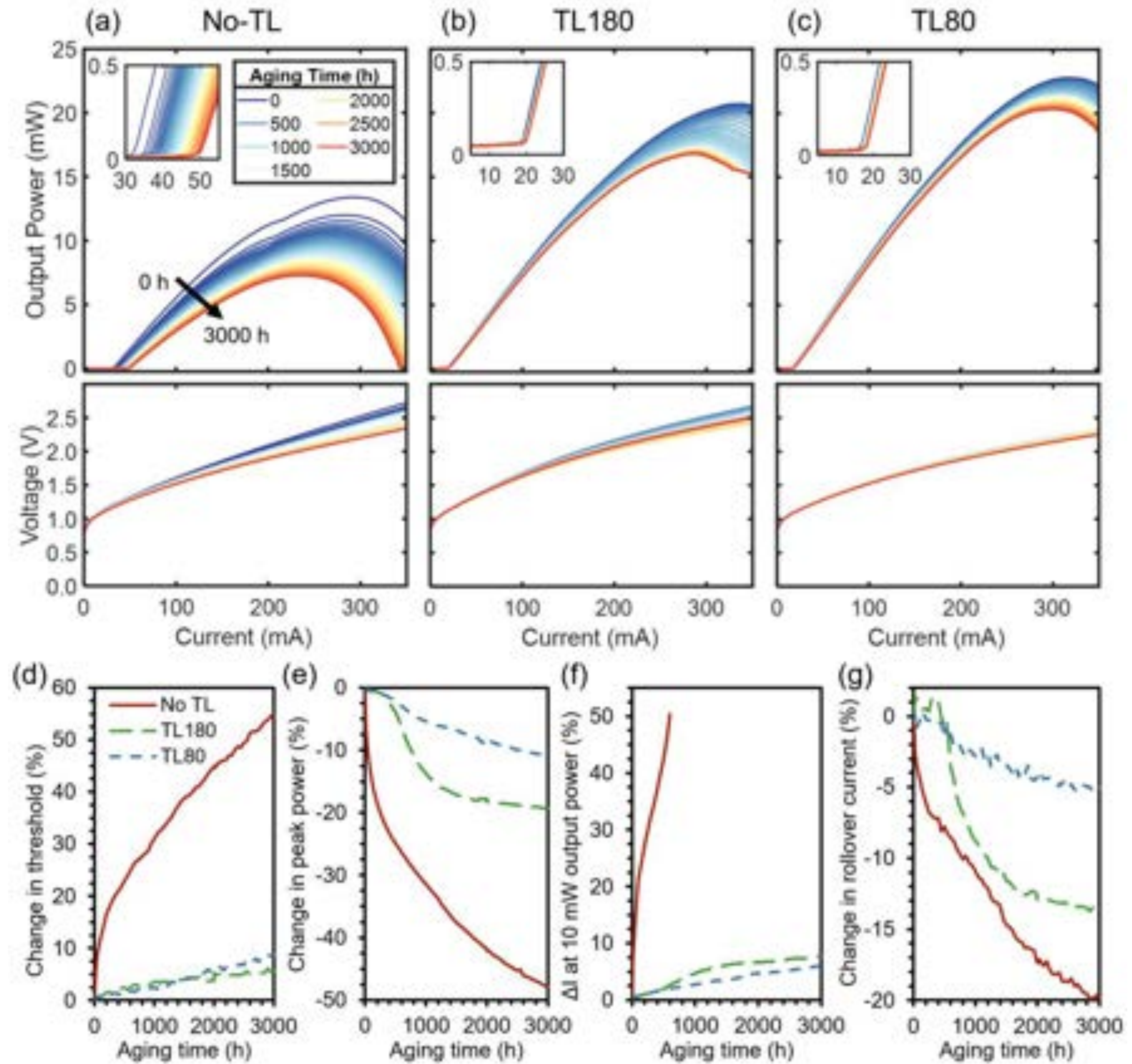

Figure 6.4 60 °C reliability data for a high performing device from each design. **(a-c)** Light-output vs. current and voltage vs. current measurements taken at 50 h intervals over the course of aging for **(a)** No-TL, **(b)** TL180, and **(c)** TL80. **(d-g)** Degradation behavior for the same three lasers measured by **(d)** change in threshold current, **(e)** change in peak output power, **(f)** change in the current required for 10 mW of output power, and **(g)** change in current at rollover. Reprinted from J. Selvidge et al., "Reduced dislocation growth leads to long lifetime InAs quantum dot lasers on silicon at high temperatures," *Appl. Phys. Lett.*, vol. 118, no. 19, p. 192101, May 2021, doi: 10.1063/5.0052316, with the permission of AIP Publishing.

To assess whether the differences in the rollover behavior between TL180 and TL80 devices are real, we performed a Mann-Whitney U statistical test on the change in peak power at rollover for all TL lasers from each group. For these group sizes $U \leq 3$ corresponds to a statistically significant difference to α = 0.05. As shown in **Figure 6.5**, we observe a statistically significant differed in peak power drop within the first 15 hours of operation. As devices were removed for PV-STEM after 1200 hours, the analysis was not conducted beyond that point.

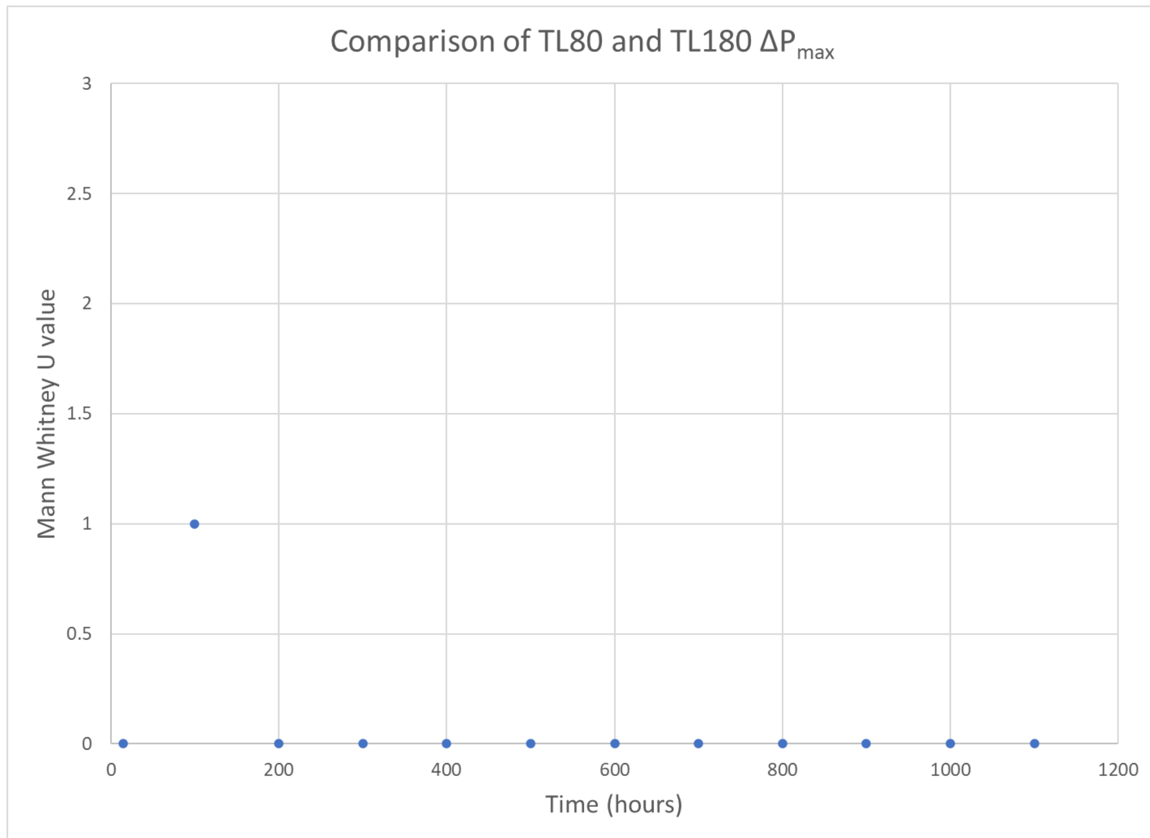

Figure 6.5 Mann-Whitney U statistical comparison between the change in peak power for TL80 and TL180 devices as a function of time. For these group sizes, (i.e., $N_{TL80} = 6$ and $N_{TL180} = 5$) $U \leq 3$ is statistically significant to significance level of α=0.05.

Comparing the performance of TL lasers to recently reported QD lasers grown on GaAs aged under similar conditions[173] we find very similar rates of 35 °C threshold current increase over 3000 h, as shown in **Figure 6.6a**. Change in output power at 2500 A/cm^2 (**Fig. 6.6b**) shows slightly slower degradation rates for native-substrate lasers. Note that differences in device dimensions and facet coatings make exact comparison between these devices difficult. Nevertheless, their behaviors are strikingly similar. This suggests that substantially reducing the misfit dislocation density leads to degradation mechanisms far more like native substrates than might be expected. Indeed, despite a TDD of 2–4×10^7 cm^{-2}, devices with trapping layers yield reliability results comparable to those obtained in threading-dislocation-free lasers; most degradation in the No-TL lasers results from MDs in the active region.

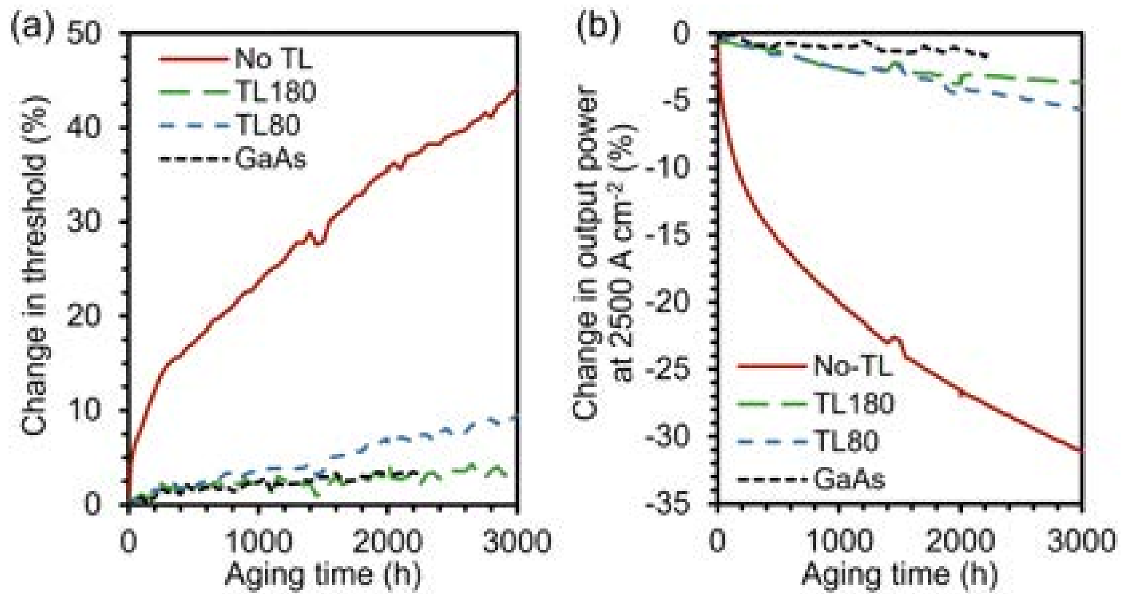

Figure 6.6 60 °C lifetime testing with performance measurements acquired at 35 °C for the three high performing devices presented in **Figure 6.4** and similar device structures on GaAs substrates from ref.[173]. Comparing (**a**) change in threshold current and (**b**) change in output power at 2500 A cm^{-2} injection we find that the TL lasers' degradation behavior appears far more like the native substrate device's behavior than the No-TL's behavior. Although all the devices presented were aged at 60 °C, LI data was only collected at 35 °C for the devices on GaAs, thus, unlike in **Figure 6.4**, the summarized TL and No-TL data presented here were measured at 35 °C. Reprinted from J. Selvidge et al., "Reduced dislocation growth leads to long lifetime InAs quantum dot lasers on silicon at high temperatures," *Appl. Phys. Lett.*, vol. 118, no. 19, p. 192101, May 2021, doi: 10.1063/5.0052316, with the permission of AIP Publishing.

To provide additional evidence for the substantially reduced role threading dislocations play in facilitating failure compared to misfit dislocations, in a separate study, we compared the relative reliability improvements available by adding trapping layers and adding a newly designed asymmetrical graded (ASG) threading dislocation buffer structure.[60] For additional details on the ASG buffer, refer to ref.[41]. **Figures 6.7a-c** present the extrapolated lifetime at 80°C based on the median change in current required for 10 mW of output power, median increase in threshold current, and the median reduction in max power. As noted,

Sample A presents our previous record-breaking device structures, while Sample B and Sample C include trapping layers and trapping layers as well as the ASG buffer, respectively. Including trapping layers increases the extrapolated lifetime by between 50-100 fold after the first 1200 hours of aging. In contrast, a Mann-Whitney *U* statistical comparison between the samples in groups B and C does not yield a statistically significant difference between the groups at t=1200 hours, suggesting that the small differences that appear in the extrapolations are within the error. This is an especially interesting result, given the long-standing emphasis on threading dislocation density reduction within the field. Note that Mr. Chen Shang performed the growth of the samples presented in **Figure 6.7**; he remains a student in the Bowers group.

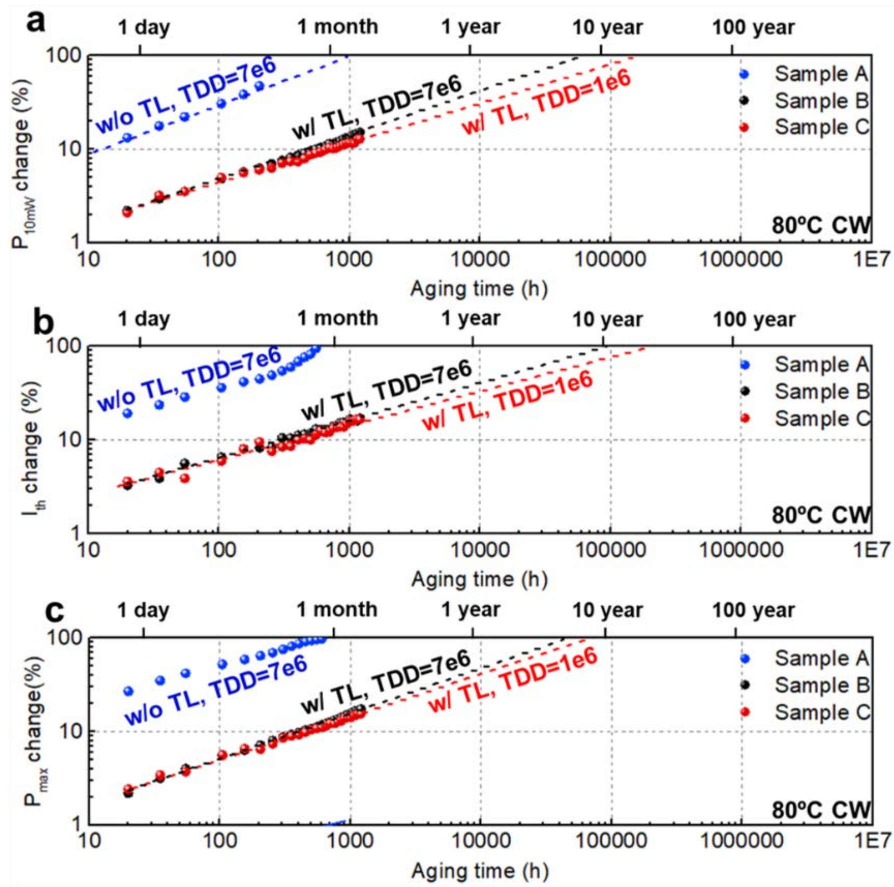

Figure 6.7 Median percent change of **(a)** current required for 10 mW output power, **(b)** threshold current, and **(c)** peak output power after 1200 hours of 80°C operation at twice the devices' initial threshold current. After ref.[60]

6.3.3 Evaluating Different Trapping Layer Spacings via STEM

To remind the reader of the various factors at play in trapping layer height optimization, **Figure 6.8** presents a composite cross-sectional scanning transmission electron microscopy (STEM) image from a typical TL180 laser. I imaged the left portion along the [110] zone axis of the sample and the right portion by tilting the sample along **g**=**002**. The tilted sample is presented schematically in the inset to assist with image interpretation. The yellow arrows in

the magnified outset denote misfit dislocations that lie flat along the projected thickness of the upper trapping layer. The orange and red arrows mark a dislocation running perpendicular to imaging direction. Most of the misfit dislocation length lies at the trapping layer (orange arrow), however, a short segment lies at the uppermost QD layer (red arrow). This is consistent with the previous observations of partial trapping layer failure discussed in **Chapter 5**.

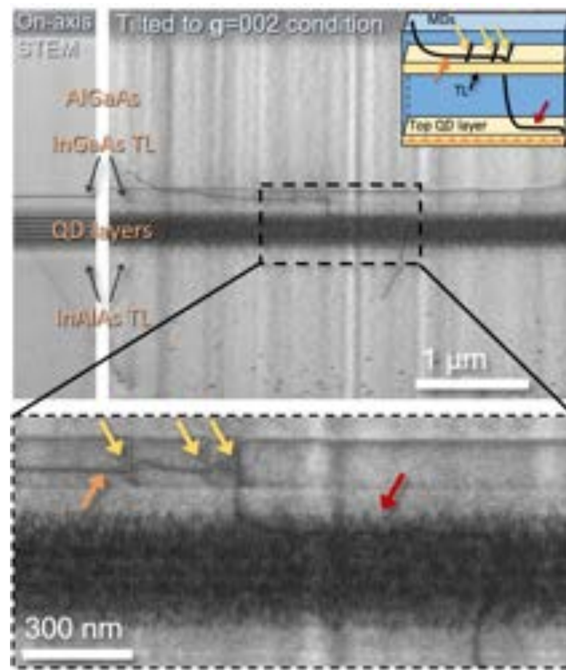

Figure 6.8 Cross-sectional scanning transmission electron micrograph of a TL180 laser structure along the [110] zone axis (left) and tilted to a **g**=002 diffraction condition (right). The outset presents a high magnification image of the dashed region. At higher magnification we can see that a threading dislocation rises through the QD layers, forms a short misfit dislocation (MD) segment (red arrow) at the fifth QD layer, and forms a trapped MD (orange arrow) segment at the upper TL. Yellow arrows denote perpendicular MDs at the upper trapping layer which appear as short vertical segments in projection, (shown schematically in the inset). Reprinted from J. Selvidge et al., “Reduced dislocation growth leads to long lifetime InAs quantum dot lasers on silicon at high temperatures,” *Appl. Phys. Lett.*, vol. 118, no. 19, p. 192101, May 2021, doi: 10.1063/5.0052316, with the permission of AIP Publishing.

PV-STEM Analyses of Degraded Trapping Layer Lasers

We selected the most heavily degraded device (evaluated by reduction in peak power) from each group for STEM analysis. I then prepared a foil containing the active region (and trapping layers) using standard focused ion beam lift-out processes. Examining the MD networks in the three aged lasers using PV-STEM helps to explain the differences in the measured reliability data between the three designs. Note that although the No-TL and TL180 devices were removed from the aging rack after 1200 hours of operation, we aged the TL80 device for an additional 600 hours to achieve a drop in peak power greater than 15%.

Figures 6.9a-c show large section from the plan-view foils generated for the No-TL, TL180, and TL80, respectively. The MD densities are similar: 4.8 μm^{-1} in the No-TL foil and 4.4 μm^{-1} in each TL foil. This agrees with our expectation that the misfit dislocation formation mechanism is the same in each case and that the TDD of the templates are approximately equal. In the No-TL, the MDs, which were straight prior to aging,[46] underwent REDC and now appear wavy. And, while there is clear variation in the extent of REDC across different misfit dislocations and along the length of individual ones, all the MDs show some small, jagged features along their length. All the MDs in this sample lie along the uppermost or lowermost QD layer (shown schematically in **Figure 6.9a** inset). This positions them directly in the active region where they can facilitate significant amounts of SRH recombination. However, the variation in the extent of climb, demonstrated clearly in **Figure 6.9d**, deserves some explanation. My colleagues and I believe that the extent of climb may be partially dependent on whether a given MD lies at the first quantum dot layer or at the fifth the active region. The active region is modulation p-doped, so MDs near the n-cladding likely see larger

minority carrier densities. As SRH rates depend linearly on the number of available carriers, the n-side misfit dislocations likely undergo more REDC than those on the p-side. However, we also expect significantly reduced misfit dislocation densities on the n-side,[80], [174], [62] explaining why only a few MDs show such large amounts of climb.

In marked contrast, most dislocations in the aged TL180 and TL80 lasers, show no clear evidence of REDC. A close inspection of **Figure 6.9e** and **Figure 6.9f** reveals a few instances of climbed MDs, marked by orange arrows. We found that only 9% and 1% of the total MD length in the TL180 and TL80 foils, respectively, have clear evidence of REDC. Thus, both TL designs displace misfit dislocation formation sufficiently far into the doped regions to prevent evidence of REDC after 1200 and 1800 hours of aging for TL180 and TL80, respectively.

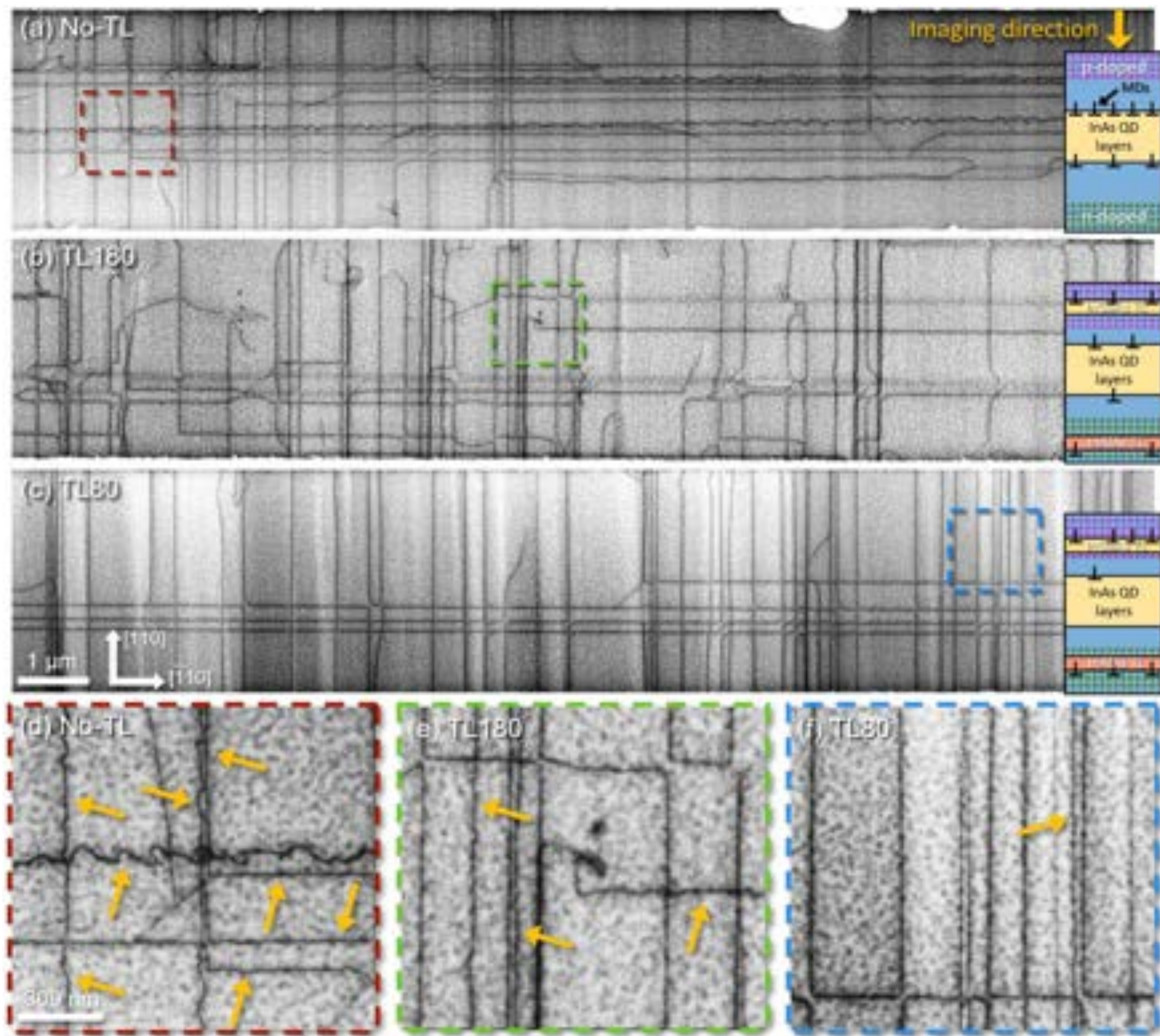

Figure 6.9 (a-c) Plan-view scanning transmission electron micrographs (acquired slightly off the [001]-zone axis to improve dislocation contrast) from lifetime tested **(a)** no-TL (1200 h), **(b)** TL180 (1200 h), and **(c)** TL80 (1800 h) lasers. The measured misfit dislocation density in each of the three foils was between 4-5 μm^{-1}. The schematic insets provide the reader with the misfit dislocations expected locations in each structure. In (a) the no-TL laser, as the misfit dislocations lie at the uppermost and lowermost QD layers, they show moderate to extensive waviness—evidence of recombination-enhanced dislocation climb (REDC). This is more obvious in **(d)** which presents a high magnification image of the boxed region in (a). In the TL lasers, we expect most misfit dislocations are trapped, and, indeed, the vast majority show no clear evidence of REDC. However, in these structures a few misfit dislocations still show evidence of REDC examples of which (marked with orange arrows) are presented in analogous high magnification images for **(e)** TL180 and **(f)** TL80. The total climbed MD length is approximately 9x larger in TL180 than TL80. Each foil is ~600-950 nm thick with ~70 μm^2 of total imageable area. Reprinted from J. Selvidge et al., "Reduced dislocation growth leads to long lifetime InAs quantum dot lasers on silicon at high temperatures," *Appl. Phys. Lett.*, vol. 118, no. 19, p. 192101, May 2021, doi: 10.1063/5.0052316, with the permission of AIP Publishing.

Tomographic Evaluations of Degraded Trapping Layer Lasers

To confirm that the climbed misfit dislocations in the TL samples lie at the QD layers, we generate a tomographic reconstruction of a section of the TL80 foil (**Figure 6.10**) and of a section of the TL180 foil (**Figure 6.11**). These tomograms are generated from 11 images taken in 5° increments along (220)-type Kikuchi lines. While insufficient strain contrast means the trapping layers themselves are not visible, most of the MDs lie at their expected height in **Figure 6.10** (~80 nm) either above the active region in the p-doped cladding (section A) or below in the n-doped cladding (section C). The only misfit dislocation with unambiguous evidence of REDC lies at the QD layers (section B). The analogous reconstruction of TL180, presents a single trapped MD and a single MD at the QDs. The MD at the QD layer (section B) shows evidence of REDC while the MD at the upper TL in the p-cladding (section A) remains straight. Note that the increased foil thickness required to capture the TL180 active region reduces image sharpness.

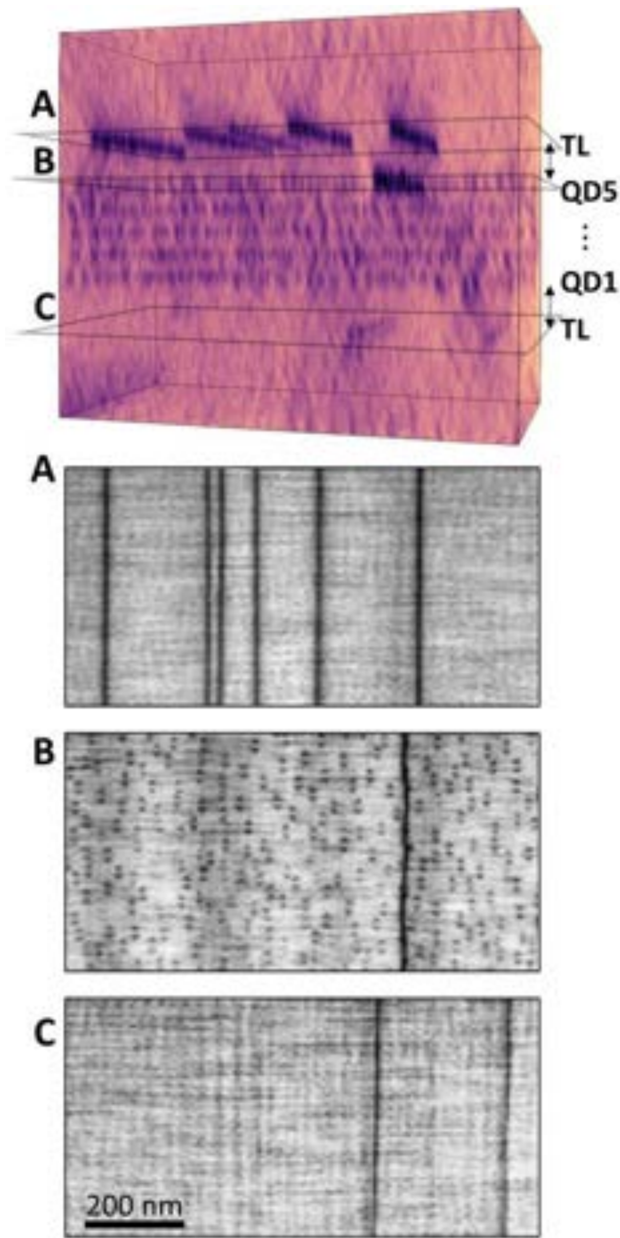

Figure 6.10 Strain-contrast tomographic reconstruction of a small portion of the TL80 laser foil in **Figure 6.9c**. The 3D reconstruction and the thin, reconstructed plan view 'image' slices shows a single misfit dislocation lying near the fifth QD layer (section B). All the other misfit segments lie either at the upper trapping layer (section A) or at the lower trapping layer (section C). Note that the trapping layers themselves are not visible in the reconstruction. Reprinted from J. Selvidge et al., "Reduced dislocation growth leads to long lifetime InAs quantum dot lasers on silicon at high temperatures," *Appl. Phys. Lett.*, vol. 118, no. 19, p. 192101, May 2021, doi: 10.1063/5.0052316, with the permission of AIP Publishing.

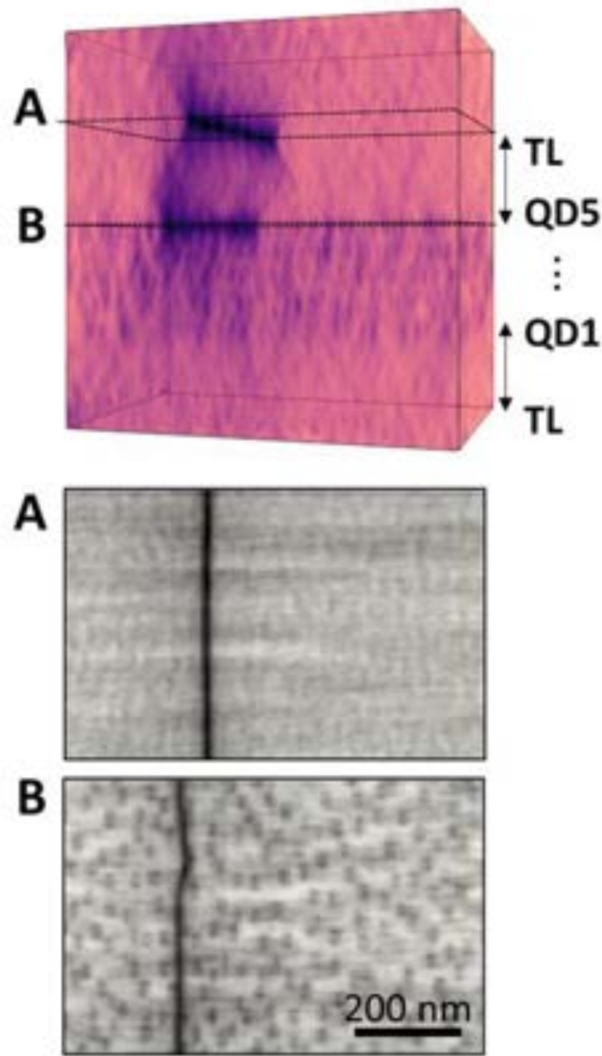

Figure 6.11 Tomographic reconstruction a small portion of the TL180 laser foil presented in **Figure 6.9b**. The thin, reconstructed plan view 'image' slices from heights A and B each show a misfit dislocation (MD). The misfit segment at the trapping layer (section A) appears straight, while the misfit segment near the QD layers shows evidence of recombination enhanced dislocation climb (section B). Note that the increased foil thickness leads to a reduction in image sharpness. Reprinted from J. Selvidge et al., "Reduced dislocation growth leads to long lifetime InAs quantum dot lasers on silicon at high temperatures," *Appl. Phys. Lett.*, vol. 118, no. 19, p. 192101, May 2021, doi: 10.1063/5.0052316, with the permission of AIP Publishing.

My colleagues and I have not yet identified the exact mechanism that results in some MDs forming at the QD layers in TL structures, but our microstructure analysis suggests that the spacing between the QDs and trapping layers plays an important role in the process. Although we offer some hypotheses in ref.[62], we have not yet been able to conclusively confirm nor rule out any specific mechanisms, to date. Further, as the performance differences appear rapidly during lifetime testing, we suspect the microstructural differences arise during cooldown, or possibly even during the thermal cycling that occurs during growth of the various layers. With a wider TL spacing the intermediary threading segment between the nearest QD layer and the TL experiences a larger driving force for glide and therefore forms a misfit dislocation segment at the QD layer. Trapping is more effective with smaller spacing but having misfit dislocations nearby will almost certainly increase SRH increasing minority carrier concentrations. A balance is required.

Unseen Degradation Mechanisms

In both TL structures the total change in misfit dislocation length seems incongruous with their performance degradation. We therefore also consider the generation of point defects by REDC; as we note in ref. [50], assuming a 5 µm point defect diffusion length, a uniform lateral 10 nm misfit dislocation excursion emits approximately 10^9 point defects (10^{18} cm^{-3}) in the active region, assuming the laser geometries reported on here (for comparison, we expect approximately 10^3 threading dislocations in the active region for TDD = $3\text{x}10^7$ cm^{-2}). These newly created point defects can then facilitate additional non-radiative recombination and degrade the performance further. Although the origin and nature of point defects participating in REDC needs further investigation, as previously mentioned, we expect that gallium

vacancies are generated through this process. Another important factor to consider is that non-radiative recombination dissipates heat and has been shown to locally increases the junction temperature. [152]–[155] This is turn may increase point defect diffusion locally and exacerbate REDC. These mutually- and self-reinforcing processes pose obvious problems, and indeed, thermal runaway at hotspots sometimes kills InAs QD lasers.[175] Furthermore, increased junction temperature can also lead to reductions in both gain[48], [176]–[178] and T_0[179] in QD lasers. Improvements in rollover and VI behavior, particularly for TL80, suggest that trapping layers substantially reduce junction heating.

6.4 Summary

While traditional dislocation filtering strategies have relied on the reduction of threading dislocation densities for reliability improvements, we demonstrate that inserting a single trapping layer on either side of the active region in doped regions of InAs QD lasers improves reliability by approximately two orders of magnitude, reaching industrially relevant metrics at both 60 and 80°C. My colleagues and I attribute these improvements to our observations that their inclusion prevents dislocation climb on about 91–99% of the observed MDs even after 1800 hours of aging. This in turn leads to substantially lowered point defect generation rates and reductions in device heating, both of which we expect result in the substantially improved performance we observe during prolonged operation at high temperatures. Within the trapping layer design space, due to the small sample sizes and large processing variation, my colleagues and I were unable to come to a conclusive answer on whether our TL180 or TL80 design was superior. **Chapter 7** proposes a more robust study, seeking to optimize this

and other trapping layer parameters to provide additional clarity. The improvement of native substrates led to the identification of slower gradual degradation modes those devices. Likewise, we may now begin to see point defect mediated degradation mechanisms and those effects arising purely from threading dislocations as QD laser performance on silicon rapidly approaches the performance of QD lasers on native substrates. It is time to look towards the advanced integration schemes proposed for photonic integrated circuits.

Chapter 7:

Conclusions and Future Directions

7.1 Introduction

The preceding Chapters represent a significant jump in our understanding of both the failure mechanisms in quantum dot lasers grown on silicon and effective mitigation strategies to address them. My results imply that carrier confinement in InAs QD materials plays at best a secondary role in improving the device performance on silicon, and that the dots own structural and mechanical properties are likely more important. However, those very same mechanical properties lead to highly damaging misfit dislocation that form during post-growth cooldown.

By applying principles from physical metallurgy, my colleagues and I effectively mitigated this. Inserting thin mechanically hardened misfit trapping layers to locally inhibit TD glide and displace MD formation away from the QDs, we obtain extrapolated device lifetimes greater than 100,000 hours at constant operating current ($2 \times I_{th}$) at 80°C. The previous best devices last for a mere 2000 hours. This orders-of-magnitude increase beyond traditional device structures arises because the trapping layer filters represent a significant departure from traditional defect filtering: they displace, rather than remove, misfit dislocations that form during cooldown, while traditional strategies seek to remove threading dislocations that form during growth. Thus, although the defect density in the full device

remains the same, we reduce number of misfit dislocations with visible evidence of recombination enhanced dislocation climb by between ten and one-hundred fold. The path forward is clear: we must begin to knowledge apply this in more advanced photonic integration schemes.

Nevertheless, fundamental materials work also remains to be done. My work demonstrates that we have a great deal still left to understand regarding the impacts of our devices' own mechanical properties on their performance and reliability. Effort to improve trapping layer design for use in InAs quantum dot lasers on Si are ongoing: their thickness, composition, placement, and number require independent optimization on the p- and n-sides of the junction. At the same time, it will also be important to revisit other industrially interesting cases, such as conventional quantum well lasers, where it has long been believed that dislocation based degradation mechanism would prevent reliable lasers. Assuming the quantum wells themselves act as threading dislocation pinning points (i.e., are themselves alloy hardened), from a mechanical perspective the trapping layers should be effective. Indeed, my colleague E. Hughes's most recent preliminary microscopy results seem to suggest they are. In any case, but especially for quantum well based designs, identifying directions to further reduce or eliminate the small fraction of un-trapped misfit dislocations is of interest as well. This is especially urgent because, to date, we do not fully understand their formation mechanism. As such, the remainder of this Chapter proposes a few possible experimental pathways to improve our understanding of the materials system.

7.2 Future Experimental Directions

7.2.1 Mechanical Properties Studies Using Model Structures

Chapters 4&5 highlight that fundamental materials studies on this system can still yield significant insight. However, the model structures my colleagues and I have used to date are, admittedly, far less complex than our full laser structures, making drawing conclusions regarding the exact mechanical behaviors in the full devices non-trivial. However, increasing the complexity of the model structures somewhat provides opportunities for improving our understanding, while still taking advantage of the relatively fast turnaround time and ability to use SEM based characterization techniques. One relatively easy possibility, for example, is to grow a few variants of the structure shown in **Figure 7.1**.

In our analysis to date, we have relied on the assumption that the mechanical properties of $Al_xGa_{1-x}As$ are functionally equivalent to those of GaAs. While this assumption is most likely correct to the first order, verifying it by growing three samples with x=0, 0.4, and 0.7 (our two current cladding compositions) and measuring the total misfit dislocation length we observe via ECCI or CL is simple to do. We could increase the experiment complexity slightly by measuring the residual strain in the three samples and growing a second set where we increase the thickness of the underlying GaAs (gray layer in Fig. 7.1) in the $Al_{0.4}Ga_{0.6}As$ and $Al_{0.7}Ga_{0.3}As$ samples. By carefully controlling the additional thickness, we can increase the tensile strain in the Al-alloyed films to the level we measure in the GaAs film, similar to the methodology employed by Hughes et al.[56] This strategy can help to differentiate whether any observed differences arise due to a difference in the glide velocities in the materials or

due to a change in the thermal driving force (from the slight difference in thermal expansion coefficient between $Al_xGa_{1-x}As$ and GaAs).

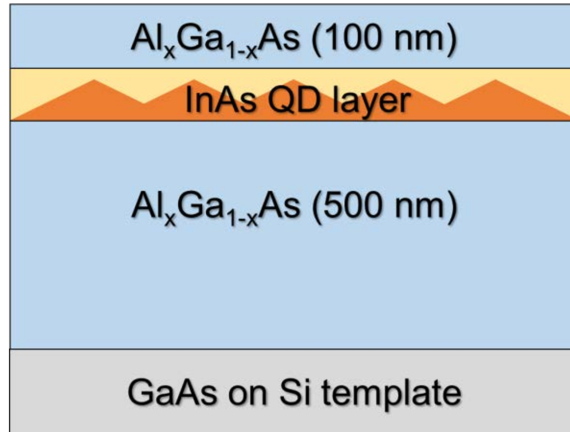

Figure 7.1 Model structure for mechanical properties inquiries. Adapted from ref.[51]

Another possibility using the basic structure presented in **Figure 7.1** would be to introduce various levels of doping to the 500 nm layer below the InAs QD layer, and above it, if desired. As mentioned previously, Yonenaga and Sumino demonstrated that doping GaAs can alter thermal dislocation glide velocities by orders of magnitude.[82] Growing otherwise equivalent undoped, n-doped, and p-doped model structures and measuring the misfit dislocation length at the QD layer, again using ECCI or CL, would provide an additional layer of complexity to our understanding of the mechanical behavior on either side of the junction during sample cooldown. As my colleagues and I suspect that both the relevant kinetics and the driving force for dislocation glide vary on either side of the junction,[62] this type of study can help us to deconvolve those effects with relatively simple analytical techniques. It is also worth noting that Yonenaga and Sumino measured a more significant glide velocity reduction

in Te-doped GaAs as compared to Si-doped GaAs. Thus, a similar experiment comparing the mechanical response to these two n-dopants specifically may be warranted.

Similarly, CL and ECCI based model structure experiments lend themselves well to improving our basic understanding of how various parameters impact trapping efficiency. **Figure 7.2** presents a simplified schematic which summarizes the parameter space for variants on the design of a structure with a single $In_xAl_{1-x}As$ trapping layer. Comparing the total quantum dot adjacent misfit dislocation length between samples varying the spacer height, marked as 'h,' the trapping layer thickness, marked as 't,' and the alloying fraction in the layer, marked 'x,' may also provide additional insight into the process by which a small fraction of misfit dislocations continues to form at the quantum dot layer. Additional strategies to remediate this are also treated in greater detail in the subsequent Section.

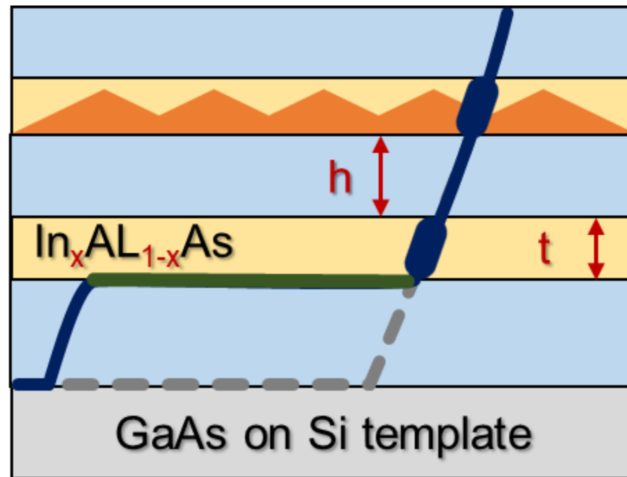

Figure 7.2 Trapping layer model structure schematic summarizing parameter space for a structure using a single $In_xAl_{1-x}As$ trapping layer. Adapted from ref.[51]

One final point of interest, from a mechanical properties perspective, is improving our understanding of the mechanism of dislocation climb in this system. While *in situ* experiments are always challenging, the GaAs/AlGaAs system (rather than InAs QDs) lends itself to a possible experimental design. For such an experiment I would suggest using growing a GaAs/AlGaAs laser on either a silicon substrate or on a scratched native substrate such that it has a large density of threading dislocations. As we do not expect that mechanical stress is required for climb as it is for glide, consistent with the growth of significant climb networks from a single threading dislocation on native substrates devices, it should then be possible to create a plan-view STEM sample with comparable geometry to the others in this work (i.e., with the substrate removed). From this point, irradiating the sample *in situ* STEM system for ten hours or so should, I would expect, allow the researcher to simultaneously observe the growth of a climb network. Ideally, this could be done using a STEM-CL system, such that the researcher could simultaneously observe the structural and optoelectronic evolution of the sample. The CL aspect could help to determine if clouds of point defects appeared to be moving towards the dislocation or away from it, which could offer some insight as to whether climb is mediated by the absorption or expulsion of point defects from the dislocation.

While ideally this section would include some calculation of the quasi-injection due to the incident electron beam, determining the fraction of 'injected' electrons and the fraction of electrons which simply pass through the sample with minimal interaction is somewhat non-trivial. An alternative option, although this too is non-trivial, could be to use a device geometry such that the contact could be wired to an external source and the device could be truly electrically injected. To do this would additionally require the use of a non-standard specimen

holder such as the Protochips Aduro 500 double-tilt MEMS-based heating and electrical biasing holder available through the Stanford Nano Shared Facilities. This design would require some sample preparation development as my current methodology for preparing plan-view samples with flat sidewalls relies heavily on the ability to view the sample on edge (as shown in **Figure 2.3**), something which would not be possible using this type of biasing holder.

7.2.2 Strategies for Reducing Un-trapped Misfit Dislocations

The results presented in **Chapter 6** suggest that the small fraction of un-trapped misfit dislocations play an important role in the degradation of laser performance over time, so strategies to further reduce them are of interest. Previous attempts to alloy harden the entire laser structure with a small fraction of indium resulted in the formation of a large number of misfit dislocations due to lattice mismatch between the laser and buffer layers.[62] As such, large scale compositional changes throughout the structure most likely would worsen lifetimes, rather than improving them. However, more targeted approaches could be successful and are worth considering; we expect that most of the remaining degradation can be attributed to the few remaining misfit dislocations at the active region. **Figure 7.3** shows one potential approach schematically. Here, the composition of interlayers between the outermost QD layer and the TL (denoted with a black box) have been slightly modified to include a very small fraction of indium. Although the spacing would need to be carefully designed such as to not exceed critical thickness, Fitzgerald's computations suggest that $In_{0.01}(Al_xGa_{1-x})_{0.99}As$ would have a critical thickness greater than 100 nm.[25] In this scenario,

we would not expect the stack to exceed critical thickness, but likely could substantially the glide on threading segments contained within the black boxed spacer layers.

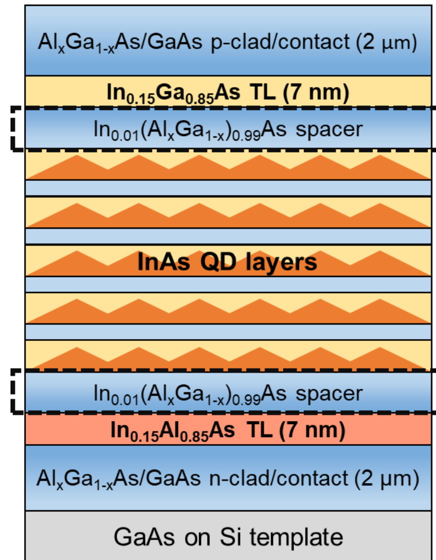

Figure 7.3 Schematic of trapping layer laser structure with alloy hardened spacer layers. Adapted from ref.[51]

Although we have not yet conclusively identified a formation mechanism for the so-called un-trapped misfit dislocation segments, the results reported in **Chapter 6** suggest that the spacing between the nearest QD layer the trapping layer plays an important role. However, it may not be desirable from a reliability perspective to induce the formation of misfit dislocation networks within a few tens of nanometers. Thus, **Figure 7.4** presents another possible approach (shown here in a model structure for simplicity): simply adding an additional trapping layer. As the majority of misfit dislocation formation appears to occur at the outer most pinning point, it may be possible to push this further away, while still trapping a very high fraction of misfit dislocations simply by adding an additional pinning point in the intermediary layers. Note also that the TL compositions in the schematic are intentionally

notated differently. As these layers serve different purposes (the outer to trap most of the misfit dislocations and the inner to hinder intermediary threading dislocation segment glide), while they can have equivalent compositions and thicknesses, this may not be necessary or even the most optimal choice from a device design perspective. Thus, going forward, efforts to independently optimize TL compositions, thicknesses, and spacings on either side of the junction will also be very important, as alluded to in the previous Section.

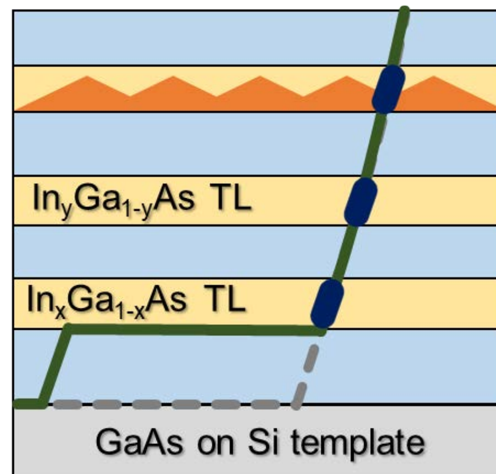

Figure 7.4 Schematic of model structure with an additional trapping layer, the composition and thickness and spacing of the two TLs should be independently optimized in this approach. Adapted from ref.[51]

7.2.3 Looking Beyond Misfit Dislocations to Improve Reliability

Given the significant strides my colleagues and I have made in mitigating misfit dislocation mediated failure, efforts to identify and address more gradual degradation mechanisms will likely become increasingly important. However, studying point defect based degradation mechanisms via electron microscopy poses some unique challenges: point defects are, for all

practical purposes, too small to be visible in an electron microscope. Nevertheless, studies like those performed by Kondo et al. which employ both electron-microscopy based techniques and other complementary measurements (e.g., deep level transient spectroscopy) can be a source of significant insight.[165] Likewise, approaches such as EBIC, CL, and EL will be useful in identifying areas where larger densities of dislocation loops may be present for site specific analytical studies. This is because, although individual point defects are rendered invisible in an electron microscope, point defect aggregates, whether in the form of precipitates or dislocation loops, are not. Simple observation of the size, density, and location of point defect aggregates can provide clues to the processes that occur during degradation. Mukherjee et al., for example, reasonably postulated that the appearance of dislocation loops near misfit dislocations and located in or immediately adjacent to highly compressively strained quantum dots during device operation (**Fig. 7.5**), suggested that the loops may themselves be tensile-strained.[50] As tensile strained dislocation loops are likely vacancy type, it thus follows that the nearby misfit dislocation underwent climb by expelling vacancies into the bulk.

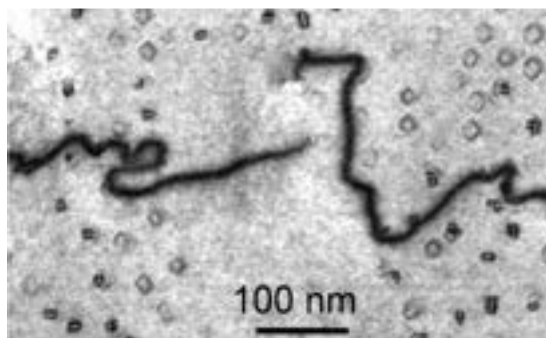

Figure 7.5 Plan-view STEM image showing dislocation loops that form climbed dislocations. Many of the dislocation loops appear to form right above the compressively strained quantum dots, suggesting they are tensile strained. Reprinted from K. Mukherjee et al., "Recombination-enhanced dislocation climb in InAs quantum dot lasers on silicon," J. Appl. Phys., vol. 128, no. 2, p. 025703, Jul. 2020, doi: 10.1063/1.5143606, with the permission of AIP Publishing.

However, while we had previously anticipated that the nearby misfit dislocation provided the point defect source for these loops, we identified similar features in subsequent electron microscopy analysis of degraded QD lasers grown on GaAs, as shown in **Figure 7.6**. TEM-based techniques such as "inside-outside" contrast analyses, although complex, may provide a more conclusive answer to the make-up of these loops (i.e., are they a compressively strained extra half plane of atoms or a tensile-strained missing one), but even once that is determined, understanding their source may remain an open question. Nevertheless, varying parameters such as laser geometry may be useful in understanding if factors such as sidewall recombination play an important role in dislocation loop formation in native substrates lasers. Further, as our results suggest that the degradation behaviors in lasers with misfit trapping layers are qualitatively like those on native substrates, efforts to better understand the degradation of QD lasers on GaAs are likely directly applicable to those grown on silicon substrates. The reader should also note that although I have treated the degradation behaviors

as essentially uniform processes in the preceding chapters, failure often occurs through highly localized mechanisms. Thus, experiments taking advantage of techniques such as EL that provide insight into site specific behaviors (e.g., failure at the facets or areas with high densities of dark spots) will likely be increasingly important soon.

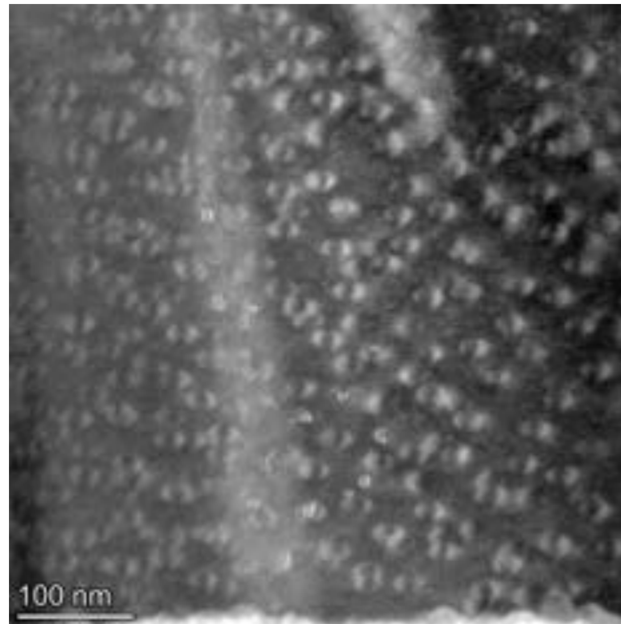

Figure 7.6 Annular dark field STEM image (acquired slightly off [001] zone axis to increase dislocation contrast) of a group of dislocation loops in a degraded InAs quantum dot laser grown on GaAs. The loops are identifiable here and in similar images by their increased contrast and decreased size.

7.3 Summary

Although we rarely consider mechanical properties of semiconductor optoelectronic systems and devices to the same extent as their optoelectronic properties, this work demonstrates that mechanical properties can have significant impacts on their performance and reliability. Likewise, by continuing to improve our understanding of them, significant improvements may

be available, not only in this system, but likely in others as well. To that end, I have proposed several rough experimental designs in the hopes of supporting future progress in this area. As I expect that improving our understanding of degradation mechanisms in InAs QD lasers on GaAs will become increasingly relevant, I have also highlighted a few potential experimental directions that should help to move us towards that goal. It is my hope that these types of experiments can continue to propel the field forward rapidly and that they continue to help us answer difficult unsolved questions and help to provide novel solutions.

References

[1] "Statistics," *ITU*. https://www.itu.int:443/en/ITU-D/Statistics/Pages/stat/default.aspx (accessed May 18, 2021).

[2] J. Hecht, "The bandwidth bottleneck that is throttling the Internet," *Nat. News*, vol. 536, no. 7615, p. 139, Aug. 2016, doi: 10.1038/536139a.

[3] C. A. Brackett, "Dense wavelength division multiplexing networks: principles and applications," *IEEE J. Sel. Areas Commun.*, vol. 8, no. 6, pp. 948–964, Aug. 1990, doi: 10.1109/49.57798.

[4] D. T. H. Tan, A. Grieco, and Y. Fainman, "Towards 100 channel dense wavelength division multiplexing with 100GHz spacing on silicon," *Opt. Express*, vol. 22, no. 9, pp. 10408–10415, May 2014, doi: 10.1364/OE.22.010408.

[5] T. A. Eriksson *et al.*, "Wavelength division multiplexing of continuous variable quantum key distribution and 18.3 Tbit/s data channels," *Commun. Phys.*, vol. 2, no. 1, Art. no. 1, Jan. 2019, doi: 10.1038/s42005-018-0105-5.

[6] R. Miglani, G. Singh, G. Singh, and D. P. Agrwal, "Gain optimization of 100 × 40 Gbps high capacity DWDM fiber optical link using hybrid amplification techniques," *J. Opt.*, vol. 49, no. 3, pp. 323–331, Sep. 2020, doi: 10.1007/s12596-020-00620-8.

[7] J. A. Farroni, A. Carter, and K. Tankala, "Optical fiber," US7116887B2, Oct. 03, 2006 Accessed: Apr. 01, 2021. [Online]. Available: https://patents.google.com/patent/US7116887B2/en

[8] I. Flammer, L.-A. de Montmorillon, and P. Matthijsse, "Optical fiber," US7555186B2, Jun. 30, 2009 Accessed: Apr. 01, 2021. [Online]. Available: https://patents.google.com/patent/US7555186B2/en

[9] Y. Nakajima, K. Mochizuki, H. Tanaka, and Y. Arashitani, "Optical fiber," US8571372B2, Oct. 29, 2013 Accessed: Apr. 01, 2021. [Online]. Available: https://patents.google.com/patent/US8571372B2/en

[10] "Prof. Douglas J. Paul :: University of Glasgow :: School of Engineering." http://userweb.eng.gla.ac.uk/douglas.paul/SiGe/lattice.html (accessed May 18, 2021).

[11] P. 30 J. 2019 | 15:30 GMT, "The Nanosheet Transistor Is the Next (and Maybe Last) Step in Moore's Law - IEEE Spectrum," *IEEE Spectrum: Technology, Engineering, and Science News*. http://spectrum.ieee.org/semiconductors/devices/the-nanosheet-transistor-is-the-next-and-maybe-last-step-in-moores-law (accessed Apr. 21, 2021).

[12] "The Macroeconomics of 450mm Wafers | SEMI." https://www.semi.org/en/macroeconomics-450mm-wafers (accessed Apr. 21, 2021).

[13] R. A. Soref, S. J. Emelett, and W. R. Buchwald, "Silicon waveguided components for the long-wave infrared region," *J. Opt. Pure Appl. Opt.*, vol. 8, no. 10, pp. 840–848, Aug. 2006, doi: 10.1088/1464-4258/8/10/004.

[14] J. F. Bauters *et al.*, "Planar waveguides with less than 0.1 dB/m propagation loss fabricated with wafer bonding," *Opt. Express*, vol. 19, no. 24, pp. 24090–24101, Nov. 2011, doi: 10.1364/OE.19.024090.

[15] G. Li *et al.*, "Ultralow-loss, high-density SOI optical waveguide routing for macrochip interconnects," *Opt. Express*, vol. 20, no. 11, p. 12035, May 2012, doi: 10.1364/OE.20.012035.

[16] E. J. Stanton, M. J. R. Heck, J. Bovington, A. Spott, and J. E. Bowers, “Multi-octave spectral beam combiner on ultra-broadband photonic integrated circuit platform,” *Opt. Express*, vol. 23, no. 9, pp. 11272–11283, May 2015, doi: 10.1364/OE.23.011272.

[17] N. Margalit, C. Xiang, S. M. Bowers, A. Bjorlin, R. Blum, and J. E. Bowers, “Perspective on the future of silicon photonics and electronics,” *Appl. Phys. Lett.*, vol. 118, no. 22, p. 220501, May 2021, doi: 10.1063/5.0050117.

[18] D. Liang and J. E. Bowers, “Recent progress in lasers on silicon,” *Nat. Photonics*, vol. 4, no. 8, Art. no. 8, Aug. 2010, doi: 10.1038/nphoton.2010.167.

[19] A. Y. Liu and J. Bowers, “Photonic Integration With Epitaxial III–V on Silicon,” *IEEE J. Sel. Top. Quantum Electron.*, vol. 24, no. 6, pp. 1–12, Nov. 2018, doi: 10.1109/JSTQE.2018.2854542.

[20] T. Egawa, Y. Hasegawa, T. Jimbo, and M. Umeno, “Degradation mechanism of AlGaAs/GaAs laser diodes grown on Si substrates,” *Appl. Phys. Lett.*, vol. 67, no. 20, pp. 2995–2997, Nov. 1995, doi: 10.1063/1.114930.

[21] O. Ueda, “On Degradation Studies of III–V Compound Semiconductor Optical Devices over Three Decades: Focusing on Gradual Degradation,” *Jpn. J. Appl. Phys.*, vol. 49, no. 9R, p. 090001, Sep. 2010, doi: 10.1143/JJAP.49.090001.

[22] B. Kunert, Y. Mols, M. Baryshniskova, N. Waldron, A. Schulze, and R. Langer, “How to control defect formation in monolithic III/V hetero-epitaxy on (100) Si? A critical review on current approaches,” *Semicond. Sci. Technol.*, vol. 33, no. 9, p. 093002, 2018, doi: 10.1088/1361-6641/aad655.

[23] J. W. Matthews, S. Mader, and T. B. Light, “Accommodation of Misfit Across the Interface Between Crystals of Semiconducting Elements or Compounds,” *J. Appl. Phys.*, vol. 41, no. 9, pp. 3800–3804, Aug. 1970, doi: 10.1063/1.1659510.

[24] J. Matthews, “Defects in epitaxial multilayers I. Misfit dislocations,” *J. Cryst. Growth*, vol. 27, pp. 118–125, Dec. 1974, doi: 10.1016/0022-0248(74)90424-2.

[25] D. J. DUNSTAN, “Strain and strain relaxation in semiconductors,” *J. Mater. Sci. Mater. Electron.*, vol. 8, no. 6, pp. 337–375, Dec. 1997, doi: 10.1023/A:1018547625106.

[26] J. P. van der Ziel, R. D. Dupuis, R. A. Logan, and C. J. Pinzone, “Degradation of GaAs lasers grown by metalorganic chemical vapor deposition on Si substrates,” *Appl. Phys. Lett.*, vol. 51, no. 2, pp. 89–91, Jul. 1987, doi: 10.1063/1.98997.

[27] D. G. Deppe *et al.*, “Room-temperature continuous operation of p-n AlxGa1−xAs-GaAs quantum well heterostructure lasers grown on Si,” *Appl. Phys. Lett.*, vol. 51, no. 9, pp. 637–639, Aug. 1987, doi: 10.1063/1.98371.

[28] D. C. Hall, D. G. Deppe, N. Holonyak, R. J. Matyi, H. Shichijo, and J. E. Epler, “Thermal behavior and stability of room-temperature continuous AlxGa1−xAs-GaAs quantum well heterostructure lasers grown on Si,” *J. Appl. Phys.*, vol. 64, no. 6, pp. 2854–2860, Sep. 1988, doi: 10.1063/1.341596.

[29] H. K. Choi, C. A. Wang, and N. H. Karam, “GaAs-based diode lasers on Si with increased lifetime obtained by using strained InGaAs active layer,” *Appl. Phys. Lett.*, vol. 59, no. 21, pp. 2634–2635, Nov. 1991, doi: 10.1063/1.105921.

[30] O. Ueda, “Materials-related reliability aspects of III–V optical devices,” *Mater. Sci. Eng. B*, vol. 20, no. 1, pp. 9–20, Jun. 1993, doi: 10.1016/0921-5107(93)90387-3.

[31] Y. Hasegawa, T. Egawa, T. Jimbo, and M. Umeno, “Suppression of <100> Dark-Line Defect Growth in AlGaAs/InGaAs Single Quantum Well Lasers Grown on Si Substrates,” *Jpn. J. Appl. Phys.*, vol. 35, no. 11R, p. 5637, Nov. 1996, doi: 10.1143/JJAP.35.5637.

[32] Z. I. Kazi, T. Egawa, T. Jimbo, and M. Umeno, “First Room-Temperature Continuous-Wave Operation of Self-Formed InGaAs Quantum Dot-Like Laser on Si substrate Grown by Metalorganic Chemical Vapor Deposition,” *Jpn. J. Appl. Phys.*, vol. 39, no. 7R, p. 3860, Jul. 2000, doi: 10.1143/JJAP.39.3860.
[33] Z. I. Kazi, P. Thilakan, T. Egawa, M. Umeno, and T. Jimbo, “Realization of GaAs/AlGaAs Lasers on Si Substrates Using Epitaxial Lateral Overgrowth by Metalorganic Chemical Vapor Deposition,” *Jpn. J. Appl. Phys.*, vol. 40, no. 8R, p. 4903, Aug. 2001, doi: 10.1143/JJAP.40.4903.
[34] M. E. Groenert *et al.*, “Monolithic integration of room-temperature cw GaAs/AlGaAs lasers on Si substrates via relaxed graded GeSi buffer layers,” *J. Appl. Phys.*, vol. 93, no. 1, pp. 362–367, Dec. 2002, doi: 10.1063/1.1525865.
[35] M. E. Groenert, A. J. Pitera, R. J. Ram, and E. A. Fitzgerald, “Improved room-temperature continuous wave GaAs/AlGaAs and InGaAs/GaAs/AlGaAs lasers fabricated on Si substrates via relaxed graded GexSi1−x buffer layers,” *J. Vac. Sci. Technol. B Microelectron. Nanometer Struct. Process. Meas. Phenom.*, vol. 21, no. 3, pp. 1064–1069, May 2003, doi: 10.1116/1.1576397.
[36] P. Petroff and R. L. Hartman, “Rapid degradation phenomenon in heterojunction GaAlAs–GaAs lasers,” *J. Appl. Phys.*, vol. 45, no. 9, pp. 3899–3903, Sep. 1974, doi: 10.1063/1.1663883.
[37] M. Yamaguchi, A. Yamamoto, M. Tachikawa, Y. Itoh, and M. Sugo, “Defect reduction effects in GaAs on Si substrates by thermal annealing,” *Appl. Phys. Lett.*, vol. 53, no. 23, pp. 2293–2295, Dec. 1988, doi: 10.1063/1.100257.
[38] I. George, F. Becagli, H. Y. Liu, J. Wu, M. Tang, and R. Beanland, “Dislocation filters in GaAs on Si,” *Semicond. Sci. Technol.*, vol. 30, p. 114004, Nov. 2015, doi: 10.1088/0268-1242/30/11/114004.
[39] D. Jung, P. G. Callahan, B. Shin, K. Mukherjee, A. C. Gossard, and J. E. Bowers, “Low threading dislocation density GaAs growth on on-axis GaP/Si (001),” *J. Appl. Phys.*, vol. 122, no. 22, p. 225703, Dec. 2017, doi: 10.1063/1.5001360.
[40] D. Jung *et al.*, “Impact of threading dislocation density on the lifetime of InAs quantum dot lasers on Si,” *Appl. Phys. Lett.*, vol. 112, no. 15, p. 153507, Apr. 2018, doi: 10.1063/1.5026147.
[41] C. Shang *et al.*, “A Pathway to Thin GaAs Virtual Substrate on On-Axis Si (001) with Ultralow Threading Dislocation Density,” *Phys. Status Solidi A*, vol. 218, no. 3, p. 2000402, 2021, doi: https://doi.org/10.1002/pssa.202000402.
[42] J.-M. Gerard and C. Weisbuch, “Semiconductor structure for optoelectronic components with inclusions,” US5075742A, Dec. 24, 1991 Accessed: May 07, 2020. [Online]. Available: https://patents.google.com/patent/US5075742A/en
[43] R. Beanland *et al.*, “Structural analysis of life tested 1.3 µm quantum dot lasers,” *J. Appl. Phys.*, vol. 103, no. 1, p. 014913, Jan. 2008, doi: 10.1063/1.2827451.
[44] T. Wang, H. Liu, A. Lee, F. Pozzi, and A. Seeds, “1.3-µm InAs/GaAs quantum-dot lasers monolithically grown on Si substrates,” *Opt. Express*, vol. 19, no. 12, pp. 11381–11386, Jun. 2011, doi: 10.1364/OE.19.011381.
[45] H. Liu *et al.*, “Long-wavelength InAs/GaAs quantum-dot laser diode monolithically grown on Ge substrate,” *Nat. Photonics*, vol. 5, no. 7, Art. no. 7, Jul. 2011, doi: 10.1038/nphoton.2011.120.

[46] A. Y. Liu, R. W. Herrick, O. Ueda, P. M. Petroff, A. C. Gossard, and J. E. Bowers, "Reliability of InAs/GaAs Quantum Dot Lasers Epitaxially Grown on Silicon," *IEEE J. Sel. Top. Quantum Electron.*, vol. 21, no. 6, pp. 690–697, Nov. 2015, doi: 10.1109/JSTQE.2015.2418226.

[47] S. Chen *et al.*, "Electrically pumped continuous-wave 13 µm InAs/GaAs quantum dot lasers monolithically grown on on-axis Si (001) substrates," *Opt. Express*, vol. 25, no. 5, p. 4632, Mar. 2017, doi: 10.1364/OE.25.004632.

[48] J. C. Norman *et al.*, "The Importance of p-Doping for Quantum Dot Laser on Silicon Performance," *IEEE J. Quantum Electron.*, vol. 55, no. 6, pp. 1–11, Dec. 2019, doi: 10.1109/JQE.2019.2941579.

[49] D. Jung *et al.*, "Recent Advances in InAs Quantum Dot Lasers Grown on On-Axis (001) Silicon by Molecular Beam Epitaxy," *Phys. Status Solidi A*, vol. 216, no. 1, p. 1800602, 2019, doi: 10.1002/pssa.201800602.

[50] K. Mukherjee *et al.*, "Recombination-enhanced dislocation climb in InAs quantum dot lasers on silicon," *J. Appl. Phys.*, vol. 128, no. 2, p. 025703, Jul. 2020, doi: 10.1063/1.5143606.

[51] J. Selvidge *et al.*, "Defect filtering for thermal expansion induced dislocations in III–V lasers on silicon," *Appl. Phys. Lett.*, vol. 117, no. 12, p. 122101, Sep. 2020, doi: 10.1063/5.0023378.

[52] J. Selvidge *et al.*, "Non-radiative recombination at dislocations in InAs quantum dots grown on silicon," *Appl. Phys. Lett.*, vol. 115, no. 13, p. 131102, Sep. 2019, doi: 10.1063/1.5113517.

[53] E. A. Fitzgerald, "Dislocations in strained-layer epitaxy : theory, experiment, and applications," *Mater. Sci. Rep.*, vol. 7, no. 3, pp. 87–142.

[54] R. Beanland, D. J. Dunstan, and P. J. Goodhew, "Plastic relaxation and relaxed buffer layers for semiconductor epitaxy," *Adv. Phys.*, vol. 45, no. 2, pp. 87–146, 1996, doi: 10.1080/00018739600101477.

[55] R. Beanland, J. P. R. David, and A. M. Sanchez, "Quantum dots in strained layers—preventing relaxation through the precipitate hardening effect," *J. Appl. Phys.*, vol. 104, no. 12, p. 123502, Dec. 2008, doi: 10.1063/1.3028270.

[56] E. T. Hughes, R. D. Shah, and K. Mukherjee, "Glide of threading dislocations in (In)AlGaAs on Si induced by carrier recombination: Characteristics, mitigation, and filtering," *J. Appl. Phys.*, vol. 125, no. 16, p. 165702, Apr. 2019, doi: 10.1063/1.5088844.

[57] J. Selvidge *et al.*, "Reduced dislocation growth leads to long lifetime InAs quantum dot lasers on silicon at high temperatures," *Appl. Phys. Lett.*, vol. 118, no. 19, p. 192101, May 2021, doi: 10.1063/5.0052316.

[58] P. Petroff and R. L. Hartman, "Defect structure introduced during operation of heterojunction GaAs lasers," *Appl. Phys. Lett.*, vol. 23, no. 8, pp. 469–471, Oct. 1973, doi: 10.1063/1.1654962.

[59] S. O'Hara, P. W. Hutchinson, and P. S. Dobson, "The origin of dislocation climb during laser operation," *Appl. Phys. Lett.*, vol. 30, no. 8, pp. 368–371, Apr. 1977, doi: 10.1063/1.89432.

[60] C. Shang *et al.*, "High-temperature reliable quantum-dot lasers on Si with misfit and threading dislocation filters," *Optica*, vol. 8, no. 5, pp. 749–754, May 2021, doi: 10.1364/OPTICA.423360.

[61] C. Shang *et al.*, "Advances in quantum dot lasers and integration with Si photonic integrated circuits," *Submitted*.

[62] K. Mukherjee *et al.*, "On the formation of misfit dislocations in InAs quantum dot lasers on silicon," *Prep.*.

[63] Z. Chen, Z. Chen, Y. Zhang, Y. Zhang, H. Zhao, and H. Zhao, “Quantitative defect analysis in MOCVD GaN-on-GaN using cathodoluminescence,” *Opt. Express*, vol. 28, no. 18, pp. 26651–26660, Aug. 2020, doi: 10.1364/OE.399986.

[64] P. Gentsch, H. Gilde, and L. Reimer, “Measurement of the top bottom effect in scanning transmission electron microscopy of thick amorphous specimens,” *J. Microsc.*, vol. 100, no. 1, pp. 81–92, 1974, doi: https://doi.org/10.1111/j.1365-2818.1974.tb03915.x.

[65] P. J. Phillips, M. J. Mills, and M. D. Graef, “Systematic row and zone axis STEM defect image simulations,” *Philos. Mag.*, Feb. 2011, Accessed: Apr. 15, 2021. [Online]. Available: http://www.tandfonline.com/doi/abs/10.1080/14786435.2010.547526

[66] P. J. Phillips, M. C. Brandes, M. J. Mills, and M. De Graef, “Diffraction contrast STEM of dislocations: Imaging and simulations,” *Ultramicroscopy*, vol. 111, no. 9, pp. 1483–1487, Aug. 2011, doi: 10.1016/j.ultramic.2011.07.001.

[67] M. Tanaka, K. Higashida, K. Kaneko, S. Hata, and M. Mitsuhara, “Crack tip dislocations revealed by electron tomography in silicon single crystal,” *Scr. Mater.*, vol. 59, no. 8, pp. 901–904, Oct. 2008, doi: 10.1016/j.scriptamat.2008.06.042.

[68] Y. Miyajima, M. Mitsuhara, S. Hata, H. Nakashima, and N. Tsuji, “Quantification of internal dislocation density using scanning transmission electron microscopy in ultrafine grained pure aluminium fabricated by severe plastic deformation,” *Mater. Sci. Eng. A*, vol. 528, no. 2, pp. 776–779, Dec. 2010, doi: 10.1016/j.msea.2010.09.058.

[69] R. Leary, P. A. Midgley, and J. M. Thomas, “Recent Advances in the Application of Electron Tomography to Materials Chemistry,” *Acc. Chem. Res.*, vol. 45, no. 10, pp. 1782–1791, Oct. 2012, doi: 10.1021/ar3001102.

[70] M. Tanaka, G. S. Liu, T. Kishida, K. Higashida, and I. M. Robertson, “Transition from a punched-out dislocation to a slip dislocation revealed by electron tomography,” *J. Mater. Res.*, vol. 25, no. 12, pp. 2292–2296, Dec. 2010, doi: 10.1557/jmr.2010.0308.

[71] S. Hata *et al.*, “High-angle triple-axis specimen holder for three-dimensional diffraction contrast imaging in transmission electron microscopy,” *Ultramicroscopy*, vol. 111, no. 8, pp. 1168–1175, Jul. 2011, doi: 10.1016/j.ultramic.2011.03.021.

[72] M. Tanaka, S. Sadamatsu, G. S. Liu, H. Nakamura, K. Higashida, and I. M. Robertson, “Sequential multiplication of dislocation sources along a crack front revealed by high-voltage electron microscopy and tomography,” *J. Mater. Res.*, vol. 26, no. 4, pp. 508–513, Feb. 2011, doi: http://dx.doi.org.proxy.library.ucsb.edu:2048/10.1557/jmr.2010.99.

[73] G. S. Liu and I. M. Robertson, “Three-dimensional visualization of dislocation-precipitate interactions in a Al-4Mg-0.3Sc alloy using weak-beam dark-field electron tomography,” *J. Mater. Res.*, vol. 26, no. 4, pp. 514–522, Feb. 2011, doi: http://dx.doi.org.proxy.library.ucsb.edu:2048/10.1557/jmr.2010.83.

[74] A. Mussi, P. Cordier, S. Demouchy, and B. Hue, “Hardening mechanisms in olivine single crystal deformed at 1090 °C: an electron tomography study,” *Philos. Mag.*, vol. 97, no. 33, pp. 3172–3185, Nov. 2017, doi: 10.1080/14786435.2017.1367858.

[75] J. S. Barnard, A. S. Eggeman, J. Sharp, T. A. White, and P. A. Midgley, “Dislocation electron tomography and precession electron diffraction – minimising the effects of dynamical interactions in real and reciprocal space,” *Philos. Mag.*, vol. 90, no. 35–36, pp. 4711–4730, Dec. 2010, doi: 10.1080/14786430903581338.

[76] J. H. Sharp, J. S. Barnard, K. Kaneko, K. Higashida, and P. A. Midgley, “Dislocation tomography made easy: a reconstruction from ADF STEM images obtained using automated

image shift correction," *J. Phys. Conf. Ser.*, vol. 126, p. 012013, Aug. 2008, doi: 10.1088/1742-6596/126/1/012013.

[77] William D. Callister and David G. Rethwisch, *Materials Science and Engineering: An Introduction*, 8th ed. Danvers, MA: Wiley, 2010.

[78] K. Mukherjee, "Chapter 4 - Materials science of defects in GaAs-based semiconductor lasers," in *Reliability of Semiconductor Lasers and Optoelectronic Devices*, R. W. Herrick and O. Ueda, Eds. Woodhead Publishing, 2021, pp. 113–176. doi: 10.1016/B978-0-12-819254-2.00007-2.

[79] Y. Kamimura, K. Edagawa, and S. Takeuchi, "Experimental evaluation of the Peierls stresses in a variety of crystals and their relation to the crystal structure," *Acta Mater.*, vol. 61, no. 1, pp. 294–309, Jan. 2013, doi: 10.1016/j.actamat.2012.09.059.

[80] P. Borvin, J. Rabier, and H. Garem, "Plastic deformation of GaAs single crystals as a function of electronic doping I: Medium temperatures (150–650°C)," *Philos. Mag. A*, vol. 61, no. 4, pp. 619–645, Apr. 1990, doi: 10.1080/01418619008231939.

[81] H. Alexander and P. Haasen, "Dislocations and Plastic Flow in the Diamond Structure," in *Solid State Physics*, vol. 22, F. Seitz, D. Turnbull, and H. Ehrenreich, Eds. Academic Press, 1969, pp. 27–158. doi: 10.1016/S0081-1947(08)60031-4.

[82] I. Yonenaga and K. Sumino, "Impurity effects on the generation, velocity, and immobilization of dislocations in GaAs," *J. Appl. Phys.*, vol. 65, no. 1, pp. 85–92, Jan. 1989, doi: 10.1063/1.343380.

[83] H. Conrad, "Thermally activated deformation of metals," *JOM*, vol. 16, no. 7, pp. 582–588, Jul. 1964, doi: 10.1007/BF03378292.

[84] H. Conrad, "The athermal component of the flow stress in crystalline solids," *Mater. Sci. Eng.*, vol. 6, no. 4, pp. 265–273, Oct. 1970, doi: 10.1016/0025-5416(70)90054-6.

[85] R. Zeyfang, O. Buck, and A. Seeger, "Thermally Activated Plastic Deformation of High-Purity Copper Single Crystals," *Phys. Status Solidi B*, vol. 61, no. 2, pp. 551–561, 1974, doi: 10.1002/pssb.2220610220.

[86] H. W. Rosenberg and W. D. Nix, "Solid solution strengthening in Ti-Al alloys," *Metall. Trans.*, vol. 4, no. 5, pp. 1333–1338, May 1973, doi: 10.1007/BF02644529.

[87] K. Okazaki, "Solid-solution hardening and softening in binary iron alloys," *J. Mater. Sci.*, vol. 31, no. 4, pp. 1087–1099, Feb. 1996, doi: 10.1007/BF00352911.

[88] I. Yonenaga and K. Sumino, "Mechanical strength of GeSi alloy," *J. Appl. Phys.*, vol. 80, no. 6, pp. 3244–3247, Sep. 1996, doi: 10.1063/1.363266.

[89] I. Yonenaga, K. Sumino, G. Izawa, H. Watanabe, and J. Matsui, "Mechanical property and dislocation dynamics of GaAsP alloy semiconductor," *J. Mater. Res.*, vol. 4, no. 2, pp. 361–365, Apr. 1989, doi: 10.1557/JMR.1989.0361.

[90] J. C. Mikkelsen and J. B. Boyce, "Extended x-ray-absorption fine-structure study of Ga 1 − x In x As random solid solutions," *Phys. Rev. B*, vol. 28, no. 12, pp. 7130–7140, Dec. 1983, doi: 10.1103/PhysRevB.28.7130.

[91] A. Gangopadhyay, A. Maros, N. Faleev, R. R. King, and D. J. Smith, "Atomic Structure of Extended Defects in GaAs-based Heterostructures," *Microsc. Microanal.*, vol. 25, no. S2, pp. 2022–2023, Aug. 2019, doi: 10.1017/S1431927619010845.

[92] I. Yonenaga and K. Sumino, "Effects of In impurity on the dynamic behavior of dislocations in GaAs," *J. Appl. Phys.*, vol. 62, no. 4, pp. 1212–1219, Aug. 1987, doi: 10.1063/1.339672.

[93] D. J. Dunstan, S. Young, and R. H. Dixon, “Geometrical theory of critical thickness and relaxation in strained-layer growth,” *J. Appl. Phys.*, vol. 70, no. 6, pp. 3038–3045, Sep. 1991, doi: 10.1063/1.349335.
[94] T. G. Andersson, Z. G. Chen, V. D. Kulakovskii, A. Uddin, and J. T. Vallin, “Variation of the critical layer thickness with In content in strained InxGa1−xAs-GaAs quantum wells grown by molecular beam epitaxy,” *Appl. Phys. Lett.*, vol. 51, no. 10, pp. 752–754, Sep. 1987, doi: 10.1063/1.98856.
[95] E. P. O’Reilly and A. R. Adams, “Band-structure engineering in strained semiconductor lasers,” *IEEE J. Quantum Electron.*, vol. 30, no. 2, pp. 366–379, Feb. 1994, doi: 10.1109/3.283784.
[96] M. Sugo, N. Uchida, A. Yamamoto, T. Nishioka, and M. Yamaguchi, “Residual strains in heteroepitaxial III-V semiconductor films on Si(100) substrates,” *J. Appl. Phys.*, vol. 65, no. 2, pp. 591–595, Jan. 1989, doi: 10.1063/1.343113.
[97] P. G. Callahan, B. B. Haidet, D. Jung, G. G. E. Seward, and K. Mukherjee, “Direct observation of recombination-enhanced dislocation glide in heteroepitaxial GaAs on silicon,” *Phys. Rev. Mater.*, vol. 2, no. 8, p. 081601, Aug. 2018, doi: 10.1103/PhysRevMaterials.2.081601.
[98] B. W. Dodson and J. Y. Tsao, “Relaxation of strained-layer semiconductor structures via plastic flow,” *Appl. Phys. Lett.*, vol. 51, no. 17, pp. 1325–1327, Oct. 1987, doi: 10.1063/1.98667.
[99] W. D. Nix, D. B. Noble, and J. F. Turlo, “Mechanisms and Kinetics of Misfit Dislocation Formation in Heteroepitaxial Thin Films,” *MRS Online Proc. Libr. Arch.*, vol. 188, ed 1990, doi: 10.1557/PROC-188-315.
[100] D. C. Houghton, “Strain relaxation kinetics in Si1−xGex/Si heterostructures,” *J. Appl. Phys.*, vol. 70, no. 4, pp. 2136–2151, Aug. 1991, doi: 10.1063/1.349451.
[101] L. B. Freund and R. Hull, “On the Dodson–Tsao excess stress for glide of a threading dislocation in a strained epitaxial layer,” *J. Appl. Phys.*, vol. 71, no. 4, pp. 2054–2056, Feb. 1992, doi: 10.1063/1.351154.
[102] V. K. Yang, M. Groenert, C. W. Leitz, A. J. Pitera, M. T. Currie, and E. A. Fitzgerald, “Crack formation in GaAs heteroepitaxial films on Si and SiGe virtual substrates,” *J. Appl. Phys.*, vol. 93, no. 7, pp. 3859–3865, Mar. 2003, doi: 10.1063/1.1558963.
[103] V. Shchukin, N. N. Ledentsov, and D. Bimberg, *Epitaxy of Nanostructures*. Berlin Heidelberg: Springer-Verlag, 2004. doi: 10.1007/978-3-662-07066-6.
[104] “Stranski–Krastanov growth,” *Wikipedia*. Mar. 24, 2021. Accessed: May 18, 2021. [Online]. Available: https://en.wikipedia.org/w/index.php?title=Stranski%E2%80%93Krastanov_growth&oldid=1013903129
[105] L. H. Li, G. Patriarche, M. Rossetti, and A. Fiore, “Growth and characterization of InAs columnar quantum dots on GaAs substrate,” *J. Appl. Phys.*, vol. 102, no. 3, p. 033502, Aug. 2007, doi: 10.1063/1.2764212.
[106] S. Fathpour *et al.*, “The role of Auger recombination in the temperature-dependent output characteristics (T0=∞) of p-doped 1.3 µm quantum dot lasers,” *Appl. Phys. Lett.*, vol. 85, no. 22, pp. 5164–5166, Nov. 2004, doi: 10.1063/1.1829158.
[107] N. Pauc, M. R. Phillips, V. Aimez, and D. Drouin, “Carrier recombination near threading dislocations in GaN epilayers by low voltage cathodoluminescence,” *Appl. Phys. Lett.*, vol. 89, no. 16, p. 161905, Oct. 2006, doi: 10.1063/1.2357881.

[108] T. Sugahara *et al.*, “Direct Evidence that Dislocations are Non-Radiative Recombination Centers in GaN,” *Jpn. J. Appl. Phys.*, vol. 37, no. Part 2, No. 4A, pp. L398–L400, Apr. 1998, doi: 10.1143/JJAP.37.L398.

[109] S. J. Rosner, E. C. Carr, M. J. Ludowise, G. Girolami, and H. I. Erikson, “Correlation of cathodoluminescence inhomogeneity with microstructural defects in epitaxial GaN grown by metalorganic chemical-vapor deposition,” *Appl. Phys. Lett.*, vol. 70, no. 4, pp. 420–422, Jan. 1997, doi: 10.1063/1.118322.

[110] M. Ťapajna *et al.*, “Influence of threading dislocation density on early degradation in AlGaN/GaN high electron mobility transistors,” *Appl. Phys. Lett.*, vol. 99, no. 22, p. 223501, Nov. 2011, doi: 10.1063/1.3663573.

[111] X. A. Cao and S. D. Arthur, “High-power and reliable operation of vertical light-emitting diodes on bulk GaN,” *Appl. Phys. Lett.*, vol. 85, no. 18, pp. 3971–3973, Nov. 2004, doi: 10.1063/1.1810631.

[112] J. K. Kim, R. L. Naone, and L. A. Coldren, “Lateral carrier confinement in miniature lasers using quantum dots,” *IEEE J. Sel. Top. Quantum Electron.*, vol. 6, no. 3, pp. 504–510, May 2000, doi: 10.1109/2944.865105.

[113] S. Y. Hu *et al.*, “Lateral carrier diffusion and surface recombination in InGaAs/AlGaAs quantum-well ridge-waveguide lasers,” *J. Appl. Phys.*, vol. 76, no. 8, pp. 4479–4487, Oct. 1994, doi: 10.1063/1.357279.

[114] H. A. Zarem, P. C. Sercel, J. A. Lebens, L. E. Eng, A. Yariv, and K. J. Vahala, “Direct determination of the ambipolar diffusion length in GaAs/AlGaAs heterostructures by cathodoluminescence,” *Appl. Phys. Lett.*, vol. 55, no. 16, pp. 1647–1649, Oct. 1989, doi: 10.1063/1.102226.

[115] A. Fiore *et al.*, “Carrier diffusion in low-dimensional semiconductors: A comparison of quantum wells, disordered quantum wells, and quantum dots,” *Phys. Rev. B*, vol. 70, no. 20, p. 205311, Nov. 2004, doi: 10.1103/PhysRevB.70.205311.

[116] M. Grundmann and D. Bimberg, “Theory of random population for quantum dots,” *Phys. Rev. B*, vol. 55, no. 15, pp. 9740–9745, Apr. 1997, doi: 10.1103/PhysRevB.55.9740.

[117] M. Grundmann *et al.*, “Electronic structure and energy relaxation in strained InAs/GaAs quantum pyramids,” *Superlattices Microstruct.*, vol. 19, no. 2, pp. 81–95, Mar. 1996, doi: 10.1006/spmi.1996.0011.

[118] O. Stier, M. Grundmann, and D. Bimberg, “Electronic and optical properties of strained quantum dots modeled by 8-band k\ensuremath{\cdot}p theory,” *Phys. Rev. B*, vol. 59, no. 8, pp. 5688–5701, Feb. 1999, doi: 10.1103/PhysRevB.59.5688.

[119] M. Kolarczik, N. Owschimikow, B. Herzog, F. Buchholz, Y. I. Kaptan, and U. Woggon, “Exciton dynamics probe the energy structure of a quantum dot-in-a-well system: The role of Coulomb attraction and dimensionality,” *Phys. Rev. B*, vol. 91, no. 23, p. 235310, Jun. 2015, doi: 10.1103/PhysRevB.91.235310.

[120] Yu. I. Mazur *et al.*, “Excited state coherent resonant electronic tunneling in quantum well-quantum dot hybrid structures,” *Appl. Phys. Lett.*, vol. 98, no. 8, p. 083118, Feb. 2011, doi: 10.1063/1.3560063.

[121] E. B. Yakimov, “What is the real value of diffusion length in GaN?,” *J. Alloys Compd.*, vol. 627, pp. 344–351, Apr. 2015, doi: 10.1016/j.jallcom.2014.11.229.

[122] D. Naidu, P. M. Smowton, and H. D. Summers, “The measured dependence of the lateral ambipolar diffusion length on carrier injection-level in Stranski-Krastanov quantum dot devices,” *J. Appl. Phys.*, vol. 108, no. 4, p. 043108, Aug. 2010, doi: 10.1063/1.3471812.

[123] S. Sanguinetti, M. Henini, M. Grassi Alessi, M. Capizzi, P. Frigeri, and S. Franchi, “Carrier thermal escape and retrapping in self-assembled quantum dots,” *Phys. Rev. B*, vol. 60, no. 11, pp. 8276–8283, Sep. 1999, doi: 10.1103/PhysRevB.60.8276.

[124] I. O’Driscoll, P. Blood, and P. M. Smowton, “Random Population of Quantum Dots in InAs–GaAs Laser Structures,” *IEEE J. Quantum Electron.*, vol. 46, no. 4, pp. 525–532, Apr. 2010, doi: 10.1109/JQE.2009.2039198.

[125] M. Hutchings, I. O’Driscoll, P. M. Smowton, and P. Blood, “Fermi-dirac and random carrier distributions in quantum dot lasers,” *Appl. Phys. Lett.*, vol. 104, no. 3, p. 031103, Jan. 2014, doi: 10.1063/1.4862813.

[126] Z. Liu *et al.*, “Origin of defect tolerance in InAs/GaAs quantum dot lasers grown on silicon,” *J. Light. Technol.*, pp. 1–1, 2019, doi: 10.1109/JLT.2019.2925598.

[127] D. P. Popescu, P. G. Eliseev, A. Stintz, and K. J. Malloy, “Carrier migration in structures with InAs quantum dots,” *J. Appl. Phys.*, vol. 94, no. 4, pp. 2454–2458, Jul. 2003, doi: 10.1063/1.1594816.

[128] B. E. Mdivanyan and M. S. Shikhsaidov, “Photostimulated enhancement of dislocation glide in gallium arsenide crystals,” *Phys. Status Solidi A*, vol. 107, no. 1, pp. 131–140, 1988, doi: 10.1002/pssa.2211070112.

[129] E. Depraetère, D. Vignaud, J. L. Farvacque, B. Sieber, and A. Lefebvre, “The photoplastic effect in GaAs, a model for device degradation phenomena,” *Philos. Mag. A*, vol. 61, no. 6, pp. 893–907, Jun. 1990, doi: 10.1080/01418619008234949.

[130] K. Maeda and S. Takeuchi, “Enhanced Glide of Dislocations in GaAs Single Crystals by Electron Beam Irradiation,” *Jpn. J. Appl. Phys.*, vol. 20, no. 3, p. L165, Mar. 1981, doi: 10.1143/JJAP.20.L165.

[131] K. Maeda, M. Sato, A. Kubo, and S. Takeuchi, “Quantitative measurements of recombination enhanced dislocation glide in gallium arsenide,” *J. Appl. Phys.*, vol. 54, no. 1, pp. 161–168, Jan. 1983, doi: 10.1063/1.331725.

[132] I. Yonenaga, M. Werner, M. Bartsch, U. Messerschmidt, and E. R. Werner, “Recombination-Enhanced Dislocation Motion in SiGe and Ge,” *Phys. Status Solidi A*, vol. 171, no. 1, pp. 35–40, 1999, doi: 10.1002/(SICI)1521-396X(199901)171:1<35::AID-PSSA35>3.0.CO;2-A.

[133] M. Iwamoto and A. Kasami, “Observation of dark line defects in GaP green LED’s under an external uniaxial stress,” *Appl. Phys. Lett.*, vol. 28, no. 10, pp. 591–592, May 1976, doi: 10.1063/1.88575.

[134] T. Kamejima, K. Ishida, and J. Matsui, “Injection-Enhanced Dislocation Glide under Uniaxial Stress in GaAs–(GaAl)As Double Heterostructure Laser,” *Jpn. J. Appl. Phys.*, vol. 16, no. 2, p. 233, Feb. 1977, doi: 10.1143/JJAP.16.233.

[135] O. Ueda, S. Isozumi, S. Yamakoshi, and T. Kotani, “Defect structure of degraded Ga1−xAlxAs double-heterostructure light-emitting diodes,” *J. Appl. Phys.*, vol. 50, no. 2, pp. 765–772, Feb. 1979, doi: 10.1063/1.326042.

[136] H. Wang, A. A. Hopgood, and G. I. Ng, “Analysis of dark-line defect growth suppression in InxGa1−xAs/GaAs strained heterostructures,” *J. Appl. Phys.*, vol. 81, no. 7, pp. 3117–3123, Apr. 1997, doi: 10.1063/1.364353.

[137] R. G. Waters, D. P. Bour, S. L. Yellen, and N. F. Ruggieri, “Inhibited dark-line defect formation in strained InGaAs/AlGaAs quantum well lasers,” *IEEE Photonics Technol. Lett.*, vol. 2, no. 8, pp. 531–533, Aug. 1990, doi: 10.1109/68.58039.

[138] H. Saito and T. Kawakami, "The new origin of dark-line defects in planar-stripe DH lasers," *IEEE J. Quantum Electron.*, vol. 13, no. 8, pp. 564–567, Aug. 1977, doi: 10.1109/JQE.1977.1069399.

[139] P. W. Hutchinson and P. S. Dobson, "Defect structure of degraded GaAlAs-GaAs double heterojunction lasers," *Philos. Mag. J. Theor. Exp. Appl. Phys.*, vol. 32, no. 4, pp. 745–754, Oct. 1975, doi: 10.1080/14786437508221617.

[140] T. Y. Tan, H.-M. You, and U. M. Gösele, "Thermal equilibrium concentrations and effects of negatively charged Ga vacancies in n-type GaAs," *Appl. Phys. A*, vol. 56, no. 3, pp. 249–258, Mar. 1993, doi: 10.1007/BF00539483.

[141] P. M. Petroff and L. C. Kimerling, "Dislocation climb model in compound semiconductors with zinc blende structure," *Appl. Phys. Lett.*, vol. 29, no. 8, pp. 461–463, Oct. 1976, doi: 10.1063/1.89145.

[142] P. M. Petroff, "Chapter 6 Defects in III–V Compound Semiconductors," in *Semiconductors and Semimetals*, vol. 22, W. T. Tsang, Ed. Elsevier, 1985, pp. 379–403. doi: 10.1016/S0080-8784(08)62933-6.

[143] J. P. Hirth, J. Lothe, and T. Mura, "Theory of Dislocations (2nd ed.)," *J. Appl. Mech.*, vol. 50, no. 2, pp. 476–477, Jun. 1983, doi: 10.1115/1.3167075.

[144] J. S. Speck, M. A. Brewer, G. Beltz, A. E. Romanov, and W. Pompe, "Scaling laws for the reduction of threading dislocation densities in homogeneous buffer layers," *J. Appl. Phys.*, vol. 80, no. 7, pp. 3808–3816, Oct. 1996, doi: 10.1063/1.363334.

[145] T. Ward *et al.*, "Design rules for dislocation filters," *J. Appl. Phys.*, vol. 116, no. 6, p. 063508, Aug. 2014, doi: 10.1063/1.4892162.

[146] H.-C. Luan and L. C. Kimerling, "Cyclic thermal anneal for dislocation reduction," US6635110B1, Oct. 21, 2003 Accessed: Jul. 24, 2020. [Online]. Available: https://patents.google.com/patent/US6635110B1/en

[147] Y. Takano, M. Hisaka, N. Fujii, K. Suzuki, K. Kuwahara, and S. Fuke, "Reduction of threading dislocations by InGaAs interlayer in GaAs layers grown on Si substrates," *Appl. Phys. Lett.*, vol. 73, no. 20, pp. 2917–2919, Nov. 1998, doi: 10.1063/1.122629.

[148] Y. Takano, T. Kururi, K. Kuwahara, and S. Fuke, "Residual strain and threading dislocation density in InGaAs layers grown on Si substrates by metalorganic vapor-phase epitaxy," *Appl. Phys. Lett.*, vol. 78, no. 1, pp. 93–95, Dec. 2000, doi: 10.1063/1.1338502.

[149] H. Okamoto, Y. Watanabe, Y. Kadota, and Y. Ohmachi, "Dislocation Reduction in GaAs on Si by Thermal Cycles and InGaAs/GaAs Strained-Layer Superlattices," *Jpn. J. Appl. Phys.*, vol. 26, no. 12A, p. L1950, Dec. 1987, doi: 10.1143/JJAP.26.L1950.

[150] L. B. Freund, "The driving force for glide of a threading dislocation in a strained epitaxial layer on a substrate," *J. Mech. Phys. Solids*, vol. 38, no. 5, pp. 657–679, 1990, doi: 10.1016/0022-5096(90)90027-2.

[151] C. J. Humphreys, "The scattering of fast electrons by crystals," *Rep. Prog. Phys.*, vol. 42, no. 11, pp. 1825–1887, Nov. 1979, doi: 10.1088/0034-4885/42/11/002.

[152] T. Kobayashi, T. Kawakami, and Y. Furukawa, "Thermal Diagnosis of Dark lines in Degraded GaAs-AlGaAs Double-Heterostructure Lasers," *Jpn. J. Appl. Phys.*, vol. 14, no. 4, p. 508, Apr. 1975, doi: 10.1143/JJAP.14.508.

[153] T. Kobayashi and G. Iwane, "Three Dimensional Thermal Problems of Double-Heterostructure Semiconductor Lasers," *Jpn. J. Appl. Phys.*, vol. 16, no. 8, p. 1403, Aug. 1977, doi: 10.1143/JJAP.16.1403.

[154] M. Fukuda, K. Wakita, and G. Iwane, “Observation of Dark Defects Related to Degradation in InGaAsP/InP DH Lasers under Accelerated Operation,” *Jpn. J. Appl. Phys.*, vol. 20, no. 2, p. L87, Feb. 1981, doi: 10.1143/JJAP.20.L87.

[155] V. Hortelano, J. Anaya, J. Souto, J. Jiménez, J. Perinet, and F. Laruelle, “Defect signatures in degraded high power laser diodes,” *Microelectron. Reliab.*, vol. 53, no. 9, pp. 1501–1505, Sep. 2013, doi: 10.1016/j.microrel.2013.07.071.

[156] T. L. Paoli and B. W. Hakki, “cw degradation at 300°K of GaAs double-heterostructure junction lasers. I. Emission spectra,” *J. Appl. Phys.*, vol. 44, no. 9, pp. 4108–4112, Sep. 1973, doi: 10.1063/1.1662904.

[157] B. W. Hakki and T. L. Paoli, “cw degradation at 300°K of GaAs double-heterostructure junction lasers. II. Electronic gain,” *J. Appl. Phys.*, vol. 44, no. 9, pp. 4113–4119, Sep. 1973, doi: 10.1063/1.1662905.

[158] M. Ohring, “15 - FAILURE AND RELIABILITY OF ELECTRONIC MATERIALS AND DEVICES,” in *Engineering Materials Science*, M. Ohring, Ed. San Diego: Academic Press, 1995, pp. 747–788. doi: 10.1016/B978-012524995-9/50039-8.

[159] D. Cooper, C. Gooch, and R. Sherwell, “Internal self-damage of gallium arsenide lasers,” *IEEE J. Quantum Electron.*, vol. 2, no. 8, pp. 329–330, Aug. 1966, doi: 10.1109/JQE.1966.1074057.

[160] C. H. Henry, P. M. Petroff, R. A. Logan, and F. R. Merritt, “Catastrophic damage of AlxGa1−xAs double-heterostructure laser material,” *J. Appl. Phys.*, vol. 50, no. 5, pp. 3721–3732, May 1979, doi: 10.1063/1.326278.

[161] O. Ueda, H. Imai, T. Kotani, K. Wakita, and H. Saito, “TEM observation of catastrophically degraded Ga1−xAlxAs double-heterostructure lasers,” *J. Appl. Phys.*, vol. 50, no. 11, pp. 6643–6647, Nov. 1979, doi: 10.1063/1.325894.

[162] O. Ueda, K. Wakao, S. Komiya, A. Yamaguchi, S. Isozumi, and I. Umebu, “Catastrophic degradation of InGaAsP/InGaP double-heterostructure lasers grown on (001) GaAs substrates by liquid-phase epitaxy,” *J. Appl. Phys.*, vol. 58, no. 11, pp. 3996–4002, Dec. 1985, doi: 10.1063/1.335576.

[163] S. N. G. Chu, N. Chand, W. B. Joyce, P. Parayanthal, and D. P. Wilt, “Generic degradation mechanism for 980 nm InxGa1−xAs/GaAs strained quantum-well lasers,” *Appl. Phys. Lett.*, vol. 78, no. 21, pp. 3166–3168, May 2001, doi: 10.1063/1.1371967.

[164] O. Ueda, K. Wakao, A. Yamaguchi, S. Isozumi, and S. Komiya, “Defect structures in rapidly degraded InGaAsP/InGaP double-heterostructure lasers,” *J. Appl. Phys.*, vol. 57, no. 5, pp. 1523–1532, Mar. 1985, doi: 10.1063/1.334466.

[165] K. Kondo, O. Ueda, S. Isozumi, S. Yamakoshi, K. Akita, and T. Kotani, “Positive feedback model of defect formation in gradually degraded GaAlAs light emitting devices,” *IEEE Trans. Electron Devices*, vol. 30, no. 4, pp. 321–326, Apr. 1983, doi: 10.1109/T-ED.1983.21124.

[166] M. Ikeda, O. Ueda, S. Komiya, and I. Umebu, “Thermal strain-induced degradation mechanism in the visible AlGaAs/GaAs laser,” *J. Appl. Phys.*, vol. 58, no. 7, pp. 2448–2452, Oct. 1985, doi: 10.1063/1.335919.

[167] O. Ueda, S. Yamakoshi, S. Komiya, K. Akita, and T. Yamaoka, “Transmission electron microscope observation of dark-spot defects in InGaAsP/InP double-heterostructure light-emitting diodes aged at high temperature,” *Appl. Phys. Lett.*, vol. 36, no. 4, pp. 300–301, Feb. 1980, doi: 10.1063/1.91469.

[168] S. N. G. Chu *et al.*, “Defect mechanisms in degradation of 1.3-µm wavelength channeled-substrate buried heterostructure lasers,” *J. Appl. Phys.*, vol. 63, no. 3, pp. 611–623, Feb. 1988, doi: 10.1063/1.340100.

[169] A. K. Chin, C. L. Zipfel, S. Mahajan, F. Ermanis, and M. A. DiGiuseppe, “Cathodoluminescence evaluation of dark spot defects in InP/InGaAsP light-emitting diodes,” *Appl. Phys. Lett.*, vol. 41, no. 6, pp. 555–557, Sep. 1982, doi: 10.1063/1.93602.

[170] B. Wakefield, “Strain-enhanced luminescence degradation in GaAs/GaAlAs double-heterostructure lasers revealed by photoluminescence,” *J. Appl. Phys.*, vol. 50, no. 12, pp. 7914–7916, Dec. 1979, doi: 10.1063/1.325965.

[171] A. H. Johnston and T. F. Miyahira, “Radiation degradation mechanisms in laser diodes,” *IEEE Trans. Nucl. Sci.*, vol. 51, no. 6, pp. 3564–3571, Dec. 2004, doi: 10.1109/TNS.2004.839166.

[172] M. Buffolo *et al.*, “Physical Origin of the Optical Degradation of InAs Quantum Dot Lasers,” *IEEE J. Quantum Electron.*, vol. 55, no. 3, pp. 1–7, Jun. 2019, doi: 10.1109/JQE.2019.2909963.

[173] J. C. Norman *et al.*, “Chapter 6 - Reliability of lasers on silicon substrates for silicon photonics,” in *Reliability of Semiconductor Lasers and Optoelectronic Devices*, R. W. Herrick and O. Ueda, Eds. Woodhead Publishing, 2021, pp. 239–271. doi: 10.1016/B978-0-12-819254-2.00002-3.

[174] S. K. Choi, M. Mihara, and T. Ninomiya, “Dislocation Velocities in GaAs,” *Jpn. J. Appl. Phys.*, vol. 16, no. 5, p. 737, May 1977, doi: 10.1143/JJAP.16.737.

[175] C. K. Chia, M. Suryana, and M. Hopkinson, “Thermal runaway and optical efficiency in InAs/GaAs quantum dot lasers,” *Appl. Phys. Lett.*, vol. 95, no. 14, p. 141106, Oct. 2009, doi: 10.1063/1.3245305.

[176] Gyoungwon Park, O. B. Shchekin, and D. G. Deppe, “Temperature dependence of gain saturation in multilevel quantum dot lasers,” *IEEE J. Quantum Electron.*, vol. 36, no. 9, pp. 1065–1071, Sep. 2000, doi: 10.1109/3.863959.

[177] N. F. Massé, S. J. Sweeney, I. P. Marko, A. R. Adams, N. Hatori, and M. Sugawara, “Temperature dependence of the gain in p-doped and intrinsic 1.3μm InAs⁄GaAs quantum dot lasers,” *Appl. Phys. Lett.*, vol. 89, no. 19, p. 191118, Nov. 2006, doi: 10.1063/1.2387114.

[178] R. Wang, C. Z. Tong, S. F. Yoon, C. Y. Liu, H. X. Zhao, and Q. Cao, “Temperature Characteristics of Gain Profiles in 1.3-$ \mu\hboxm\ p$-Doped and Undoped InAs/GaAs Quantum-Dot Lasers,” *IEEE Electron Device Lett.*, vol. 30, no. 12, pp. 1311–1313, Dec. 2009, doi: 10.1109/LED.2009.2033718.

[179] L. V. Asryan and R. A. Suris, “Temperature dependence of the threshold current density of a quantum dot laser,” *IEEE J. Quantum Electron.*, vol. 34, no. 5, pp. 841–850, May 1998, doi: 10.1109/3.668772.